ASRL-TR-196-1

THE DESIGN, TESTING AND EVALUATION OF THE M.I.T. INDIVIDUAL-BLADE-CONTROL SYSTEM AS APPLIED TO GUST ALLEVIATION FOR HELICOPTERS

by

Robert Miller McKillip, Jr.

February 1980

Prepared under Research Grant No. NSG-2266 by

Aeroelastic and Structures Research Laboratory
Department of Aeronautics and Astronautics
Massachusetts Institute of Technology
Cambridge, Massachusetts 02139

for

AMES RESEARCH CENTER
NATIONAL AERONAUTICS AND SPACE ADMINISTRATION
MOFFETT FIELD, CALIFORNIA 94035

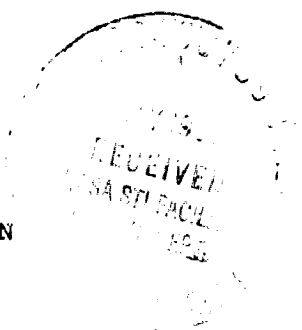

THE DESIGN, TESTING AND EVALUATION OF THE M.I.T. INDIVIDUAL-BLADE-CONTROL SYSTEM AS APPLIED TO GUST ALLEVIATION FOR HELICOPTERS

by

Robert Miller McKillip, Jr.

ABSTRACT

A new, advanced type of active control for helicopters as designed and tested on a four-foot diameter model rotor is described. A single blade was individually controlled in pitch in the rotating frame over a wide range of frequencies by electromechanical means. It is shown both analytically and experimentally that by utilizing a tip-mounted accelerometer as a sensor in the feedback path, significant reductions in blade flapping response to gust can be achieved at the gust excitation frequency as well as at super- and subharmonics of rotor speed.

Supervisor: Norman D. Ham
Professor of Aeronautics
and Astronautics

ACKNOWLEDGEMENTS

Few tasks of any reasonable size are seldom completed without outside assistance, and this research was certainly no exception. The author would like to thank Professor Norman Ham for his many hours of guidance given to the research, from the initial formulation of the IBC concept through to its validation in the wind tunnel. His timely observations and comments kept the author from exploring vast mazes of "blind alleys". Thanks are also due Mr. Paul Bauer for his great technical assistance on the project. Were it not for men like Paul, theoretical concepts and real-world hardware would have no correlation. The author would also like to thank Mr. Christopher Cholaj for donating his engineering expertise to the research, as well as Ms. Marilyn Bryant, for her typing of the manuscript.

CONTENTS

LIST OF ILLUSTRATIONS

SECTION 1

INTRODUCTION

As the helicopter's performance envelope is extended to cover a wider area of flight conditions, its control system must be capable of coping with the resulting increase in severity of the aerodynamic environment. Traditional swash plate rotor control, however, does not permit the freedom of motion required to counteract an external disturbance. With the introduction of Individual-Blade-Control, this restriction is eliminated and it then becomes possible to alleviate the adverse effects of atmospheric turbulence, retreating blade dynamic stall, blade vortex interaction and blade aerodynamic and/or mass mismatch. These benefits would be achieved by using appropriately weighted state variables in the feedback path to the pitch actuators for each blade. Thus, assuming sufficient reliability is possible to make the IBC concept a safety-of-flight item, it would then be possible to design a control configured helicopter.

The work descirbed herein is concerned only with the first phase of application of the IBC system, namely, suppression of blade flapping due to gust excitation. Two experiments were conducted, the first to verify the analytical model for flapping response to pitch input, and the second to demonstrate the effectiveness of the gust alleviation system design.

SECTION 2

MODEL DESIGN AND CONSTRUCTION

2.1 Design Philosophy

The design of the Individual-Blade-Control helicopter rotor model incorporated many parts and accessories already available at M.I.T. For simplicity and ease of modification it was decided initially to equip a single rotor blade with electromechanical pitch control, counterbalanced by two "dummy" blades of 5/8 inch steel drill rod and adjustable counterweights. Geometric restrictions were imposed upon the hardware, however, to make it possible to add two more identical but distinct pitch actuators without redesign. The complete system installed and ready for testing can be seen in Figure 1.

2.2 The Rotor Blade

The blade used in the test rotor was the same as that of Reference 1, having a NACA 0012 section with a 21.2-inch span and two-inch chord. It had an eight degree linearly decreasing twist from root to tip and was constructed of fiberglass with aluminum reinforcing. Mass and stiffness properties, as determined in Reference 2, can be seen in Figure 2. The blade was connected to the rotor hub by means of a ball-and-socket root fixture permitting flapping, lagging and feathering degrees of freedom about the same point. A complete set of rotor parameters can be found in Table 1, also taken from Reference 2.

2.3 The Control Mechanism

The individual-blade control assembly consisted of a shaft-mounted Servo motor that, through a series of linkage, acted as a position controller of the rotor blade pitch angle (Fig. 3). The motor/tachometer was mounted between two 1/4 inch thick discs of aluminum, which also held two counterweights, or "dummy motors", in order to offset the mass moment of inertia contribution of the active motor. These discs were fixed to the shaft by two aluminum blocks containing two setscrews and a keyway. Also, attached to the forward disc was an aluminum support for the transmission shaft of the control assembly.

This transmission shaft was mounted at a right angle to the motor shaft, and was given its rotation by a spiral bevel gear that was driven by a pinion on the motor shaft, with a 2:1 gear reduction ratio. This same shaft had attached to it a thin aluminum bar that had a threaded rod inserted through its other end, and parallel to the transmission shaft. Mounted on the threaded rod was yet another actuator link that consisted of two rod ends screwed together by a threaded metal coupling. The other end of the link was connected to a bolt that passes through the blades pitch axis (Fig. 4).

The rotor blade was rigidly attached to a steel fork assembly that, in turn, bolted to the inner race of a spherical bearing. The spherical bearing was then contained within a steel support block that was clamped fast to the main rotor hub, thus allowing fully articulated blade motion with concentric pitch, flap and lead-lag axes, offset from the hub by approximately two inches. The blade root fixture was instrumented with strain gages mounted on a .005 inch thick curved steel flexure that was free to turn about the lead-lag axis, but gave a torsional output corresponding to blade flapping, and a longitudinal bending output corresponding to blade ptich angle. This particular flexure geometry was chosen as a solution to the problem of uncoupling the three rigid degrees of freedom of the blade for purposes of measurement. A thickness of .005 inches was selected for the flexure in order to produce a significant signal for small blade deflections while at the same time providing a negligible restoring moment upon the blade flapping motion (Fig. 5).

SECTION 3

PITCH-SERVO ACTUATION SYSTEM DESIGN

3.1 Servo Feedback Strategy

Since the Servo motor fixed to the shaft was to function as a position control device, it was necessary to incorporate appropriately weighted feedback signals to the motor amplifier. These signals were the motor speed, taken from the tachometer, and the angular position, measured from the torsional strain gage mounted on the steel fixture attached to the blade. A block diagram of the control system can be seen in Figure 6. Both of these signals were used as feedback to acheive a faster system response for the same relative stability level.

3.2 Component Calibration and Frequency Response

In order to extract maximum performance from this configuration, an equivalent transfer function of the motor was required, and this was obtained by matching two different sets of frequency response data (corresponding to two different sets of gains) to a linear model of the Servo dynamics. Magnitude and phase versus frequency of excitation can be seen in Figures 7 and 8, corresponding to a position-only feedback, and also a position-plus-rate feedback configuration.

As can be seen in Figure 9, the motor exhibited the characteristics of a second-order system. At first this may appear to be an anomaly, but this behavior is typical of high quality Servo motors whose electrical time constants are of the same order of magnitude as their mechanical time constants. It should also be pointed out that, although the curve-fits of the motor transfer function data do not appear to be highly accurate, they are nevertheless a result of a compromise to match both sets of data equally well, since a linear model that closely approximated one of the test conditions would fail as a model of the other.

3.3 Root Locus Analysis

A revised block diagram of the Servo system, with the transfer functions of the components included in the blocks, can be seen in Figure 10. After

a bit of algebra, an overall transfer function of the Servo can be written as:

$$\frac{\theta_o(s)}{\theta_c(s)} = \frac{K}{s\left(\frac{s^2}{\omega_n^2} + \frac{2\rho}{\omega_n}s + 1\right) + K\left(K_{\dot\theta}s + K_\theta\right)}$$

The design criterion for the Servo system was for it to have as fast a response as possible, with a flat amplitude ratio up to the break point, and no more than a 30° phase lag throughout this region. The design tool that was used to select the appropriate gains for the best response was the root locus technique. A root locus plot of the general design problem can be seen in Figure 11.

A few observations can be made with regard to response characteristics upon close inspection of the locus of roots. Since the ratio of position feedback to rate feedback determines the location of the system's zero, and since with increased forward loop gain the pole at the origin will approach this zero from the right, it might be desirable to place the zero in a high-frequency range, far off to the left on the negative real axis. But since such a zero placement has a direct effect upon where the vertical asymptote for the complex pair lies, stability requirements impose restrictions upon how far this zero can be moved and how large the forward loop gain can be.

3.4 Gain Selection

Companion plots of predicted frequency response characteristics were made for these variations in gains, and final values of $\frac{k_\theta}{k_{\dot\theta}} = 140$ and $k = 1077.3$ were picked, with a break frequency of 11 Hz. A set of experimental data for this final configuration plotted along with the theoretical response can be seen in Figure 12. The system performance is more than adequate for the low-frequency gust alleviation portion of the program.

SECTION 4

WIND TUNNEL TESTING

4.1 The Test Facility

The Wright Brothers Wind Tunnel at M.I.T. was used for I.B.C. rotor frequency response testing. The test section is a 7' x 10' oval, and for rotor testing the turntable is equipped with two trunnions for horizontal mounting of the rotor shaft. This particular orientation was chosen to permit use of the existing gust generator (Ref. 5). For the first test described in this report, however, the gust generator was not installed.

Mounted outside of the test section was a hydraulic motor and slip ring assembly, providing shaft rotation and data transmission from the rotating frame to the analog computer in the fixed frame. Clamped to the far trunnion was another slip ring assembly that transmitted electrical current to the Servo motor and tachometer.

4.2 Model Installation and Instrumentation

Upon installation of the support trunnions, the rotor shaft was secured to the support bearings with the rotor plane in the center of the tunnel section. Since the control system was designed to be attached to the portion of the shaft lying in the downwash of the rotor thrust, there existed a sizable mass unbalance load upon the two trunnions, which became apparent during initial spin-ups of the shaft. This problem was overcome by attaching two steel angles to the trunnion farthest away from the control system hardware, thus increasing its stiffness and resonant frequency. Dynamic balancing was accomplished by contacting one of the 1/4-inch aluminum disks with the tip of a grease pencil and correcting for the indicated displacement.

Instrumentation used in the wind tunnel experiment consisted of: a difference amplifier, for the amplification of blade flapping and feathering strain gage signals; a portable analog computer and Servo amplifier, for processing the feedback loop signals and supplying the motor driving signal; a dual-beam storage oscilloscope, for monitoring the flap and pitch signals; a frequency counter, for monitoring the input pitch frequency; a function

generator, for supplying the pitch actuation signal; a spectrum analyzer, for on-line analysis of the blade flapping response; an X-Y plotter, for the production of a hard record of the analyzer output; another oscilloscope for quick visualization of the output of the spectrum analyzer; a difference amplifier for the amplification of the accelerometer signals; a hot wire probe and amplifier, for measurement of the gust amplitude; and finally, a PDP-11 computer, for analog-to-digital data acquisition and real time Fast Fourier Transform analysis. A schematic of the instrumentation layout is in Figure 13.

4.3 Testing Program

Since the frequency response characteristics of the servo met the design criteria for frequencies up to 70% of rotor rotational speed, it was decided that the data acquisition for the first test would be concentrated in this area. In the second test it was found that the break frequency for the servo was too close to rotational speed for an adequate gust alleviation design, and thus the rotor speed was halved for the feedback control test series.

Parameters varied in the first test included pitch excitation frequency, tunnel speed, collective pitch setting, and shaft angle with respect to the wind. A complete test matrix is included in Table 2, and all tests were conducted with a pitch excitation of plus and minus one degree, or, two degrees peak to peak.

In the second wind tunnel test, the parameters varied were gust excitation frequency, tunnel speed, and feedback gain (or, static sensitivity) value. This series is described in Table 3.

SECTION 5

THEORETICAL ANALYSIS

5.1 Equations of Motion

Given the articulated offset-hinged rotor blade shown in Figure 14, one can write the flapping equation of motion by summing moments about the offset hinge as:

$$\int_e^R \left[(r-e)^2\ddot{\beta} + r(r-e)\Omega^2\beta\right] dm = \int_e^R (r-e)\, dL \qquad (1)$$

where

$$dL = \tfrac{1}{2}\rho a c \left[\theta U_T^2 - U_p U_T\right] dr$$

$$U_T = \Omega r + \mu \Omega R \sin\psi$$

$$U_p = \lambda \Omega R + (r-e)\dot{\beta} + \mu \Omega R \beta \cos\psi$$

Factoring out $\Omega^2 R^4$ and defining $x \equiv \frac{r}{R}$, $\xi \equiv \frac{e}{R}$ gives

$$\int_e^R (r-e)\, dL = \left(\Omega^2 R^4\right) \tfrac{1}{2}\rho a c \int_\xi^1 (x-\xi)\left[\theta \frac{U_T^2}{R^2} - \frac{U_p U_T}{R^2}\right] dx$$

and after defining

$I_1 \equiv \int_e^R (r-e)^2 dm$, the blade flapping inertia

$\gamma \equiv \frac{\rho a c R^4}{I_1}$, the Lock number

substitution into Equation 1 yields, after some algebra:

$$\frac{\ddot{\beta}}{\Omega^2} + \left[A + H\mu\sin\psi\right]\frac{\dot{\beta}}{\Omega} + \left[1 + G + C\mu\cos\psi + \tfrac{1}{2}\mu^2 E \sin 2\psi\right]\beta$$
$$= \theta\left[B + \tfrac{1}{2}\mu^2 E + 2C\mu\sin\psi - \tfrac{1}{2}\mu^2 E\cos 2\psi\right]$$
$$- \left[C\lambda + E\lambda\mu\sin\psi\right] \qquad (2)$$

where

$$A = \frac{\gamma}{2}\left(\frac{1}{4} - \frac{2}{3}\xi + \frac{1}{2}\xi^2 - \frac{1}{12}\xi^4\right)$$

$$B = \frac{\gamma}{2}\left(\frac{1}{4} - \frac{1}{3}\xi + \frac{1}{12}\xi^4\right)$$

$$C = \frac{\gamma}{2}\left(\frac{1}{3} - \frac{1}{2}\xi + \frac{1}{6}\xi^3\right)$$

$$E = \frac{\gamma}{2}\left(\frac{1}{2} - \xi + \frac{1}{2}\xi^2\right)$$

$$G = \frac{1}{I_1}\int_e^R e(r-e)\,dm$$

$$H = \frac{\gamma}{2}\left(\frac{1}{3} - \xi + \xi^2 - \frac{1}{3}\xi^3\right)$$

$$I_1 = \int_e^R (r-e)^2\,dm$$

In addition to the pitch excitation terms on the right hand side of Equation 2, one must add the forcing terms due to the gust distribution across the rotor disk. Reference 1 shows these to be a series of Bessel functions, but they may be approximated by trigonometric functions as:

$$\frac{\gamma}{2}\int_\xi^1 x^2 \omega_G\,dx + \frac{\gamma}{2}\mu\sin(\Omega t)\int_\xi^1 x\,\omega_G\,dx$$

where

$x = r/R$

$\omega_G = \bar{\omega}_G \sin(\omega t - \phi_G)$

$\bar{\omega}_G$ = gust amplitude/rotor tip speed, ΩR

$$\phi_G = 2\pi\frac{R x \cos(\Omega t)}{\lambda_G} = \frac{1}{\mu}\left(\frac{\omega}{\Omega}\right) x \cos(\Omega t)$$

and substitution of this gives the following expression for the non-dimensional gust excitation:

$$\omega_G = \bar{\omega}_G\left[\sin\omega t\,\cos\phi_G - \cos\omega t\,\sin\phi_G\right]$$

Evaluation of the two integrals then yields the following terms:

$$= \overline{\omega_c} \sin \omega t \left\{ \frac{\gamma}{6}(1-\xi^3) - \frac{\gamma}{40}\frac{1}{\mu^2}\left(\frac{\omega}{\Omega}\right)^2(1-\xi^5) + \frac{\gamma}{896}\frac{1}{\mu^4}\left(\frac{\omega}{\Omega}\right)^4(1-\xi^7) \right\}$$

$$+ \overline{\omega_c} \cos(\Omega-\omega)t \left\{ \frac{\gamma}{8}\mu(1-\xi^3) - \frac{\gamma}{16}\frac{1}{\mu}\left(\frac{\omega}{\Omega}\right)(1-\xi^4) - \frac{3\gamma}{128}\frac{1}{\mu}\left(\frac{\omega}{\Omega}\right)^2(1-\xi^4) \right.$$

$$\left. + \frac{\gamma}{192}\frac{1}{\mu^3}\left(\frac{\omega}{\Omega}\right)^3(1-\xi^6) + \frac{\gamma}{3072}\frac{1}{\mu^3}\left(\frac{\omega}{\Omega}\right)^4(1-\xi^6) - \frac{\gamma}{6144}\frac{1}{\mu^5}\left(\frac{\omega}{\Omega}\right)^5(1-\xi^8) \right\}$$

$$+ \overline{\omega_c} \cos(\Omega+\omega)t \left\{ -\frac{\gamma}{8}\mu(1-\xi^2) - \frac{\gamma}{16}\frac{1}{\mu}\left(\frac{\omega}{\Omega}\right)(1-\xi^4) + \frac{3\gamma}{128}\frac{1}{\mu}\left(\frac{\omega}{\Omega}\right)^2(1-\xi^4) \right.$$

$$\left. + \frac{\gamma}{192}\frac{1}{\mu^3}\left(\frac{\omega}{\Omega}\right)^3(1-\xi^6) - \frac{\gamma}{3072}\frac{1}{\mu^3}\left(\frac{\omega}{\Omega}\right)^4(1-\xi^6) - \frac{\gamma}{6144}\frac{1}{\mu^5}\left(\frac{\omega}{\Omega}\right)^5(1-\xi^8) \right\}$$

$$+ \text{H.O.T.}$$

These would then be added onto the RHS of Equation 2 to describe the rigid flapping response to pitch and gust inputs. This expression contains periodic coefficients that can be eliminated using the harmonic balance technique as described below.

Since the I.B.C. rotor used a tip-mounted accelerometer as a feedback sensor, it is necessary to consider the effects of its placement upon the signal content of its output. Figure 15 shows the acceleration in the flatwise direction, a_F, to be:

$$a_F \doteq (R-e)\ddot{\beta} + R\Omega^2\beta + g\cos(\Omega t)\beta$$

and for any sinusoidal variation of flap angle,

$$\beta = A\sin\omega t \quad , \quad \ddot{\beta} = -\omega^2 A \sin\omega t$$

and hence,

$$a_F \doteq \left[R\Omega^2 - (R-e)\omega^2 + g\cos(\Omega t) \right] A \sin \omega t$$

Thus, this signal will be strongly frequency dependent, producing a value proportional to blade flapping position at low frequencies ($\omega << \Omega$) and one proportional to flapping accelerations at high frequencies ($\omega >> \Omega$), while having a negligible output at frequencies close to rotational frequency. Also, due to the high rotation speed of the rotor, the periodic portion of the accelerometer signal can be neglected.

5.2 Harmonic Balance

Standard harmonic balance solutions involve a simple substitution of assumed harmonic motion expressions, and then an equating of coefficients of like periodic functions. These assumed motions included a steady-state term plus harmonics at the gust excitation frequency (ω), rotor rotation frequency (Ω), and at the first subharmonic ($\Omega-\omega$) and superharmonic ($\Omega+\omega$) of the rotation frequency:

flapping motion:
$$\beta(t) = \beta_0 + \bar{\beta}_c \cos\omega t + \bar{\beta}_s \sin\omega t + \hat{\beta}_c \cos\Omega t + \hat{\beta}_s \sin\Omega t + \beta_c' \cos(\Omega-\omega)t + \beta_s' \sin(\Omega-\omega)t + \beta_c'' \cos(\Omega+\omega)t + \beta_s'' \sin(\Omega+\omega)t$$

pitching motion:
$$\theta(t) = \theta_0 + \bar{\theta}_c \cos\omega t + \bar{\theta}_s \sin\omega t + \hat{\theta}_c \cos\Omega t + \hat{\theta}_s \sin\Omega t + \theta_c' \cos(\Omega-\omega)t + \theta_s' \sin(\Omega-\omega)t + \theta_c'' \cos(\Omega+\omega)t + \theta_s'' \sin(\Omega+\omega)t$$

Substitution of these expressions into Equation 2 resulted in a matrix equation relating the nine blade flapping coefficients to the gust and pitch excitation terms. This matrix equation was then solved to extract the flapping coefficients as described in more detail in the appendix.

SECTION 6

DESIGN OF THE GUST ALLEVIATION SYSTEM

6.1 Desired Response Characteristics

In order to have some guidelines for approaching the problem of synthesis of a gust alleviation system design, an adequate definition of the requirements for the system response was necessary. Since primary helicopter control is achieved through orientation of the rotor thrust vector with respect to the fuselage, it is obvious that tighter control over orientation of the tip path plane (and hence the thrust vector) will improve the vehicle's handling qualities. In the rotating frame these pilot commands are either very low frequency (with respect to rotor rotation) such as thrust and maneuvering commands, or at rotor rotational speed, relating to static positioning of the tip path plane in space. Hence, any blade flapping due to an external disturbance, such as a low frequency gust, can be viewed as a perturbation which one wishes to attenuate as quickly as possible. A block diagram of the IBC system can be seen in Figure 16.

Since the work described here was performed upon a model rotor, the task of tracking a simulated pilot command was deemed secondary to merely reducing the effects of a gust disturbance upon the forward flight flapping response of the blade. The emphasis in the design process was directed at low frequency flap attenuation while producing no ill-effects upon the high-frequency flapping response, and striving for the simplest configuration possible.

6.2 Design Procedure

Design of the IBC rotor system was complicated by the presence of periodic terms in the blade's equation of motion, as can be seen in the previous section. These trigonometric terms, however, are first or second order in μ (advance ratio), and thus drop out in the case of hovering flight. Reference 6 suggests that because of this phenomenon, a constant coefficient expression for the blade flapping equation motion was possible over the range of low advance ratio. As a check to see if this approximation was valid for the model rotor used in the experiments, the method of

Reference 8 was applied to Equation 2, and the poles of the blade characteristic equation were found not to vary significantly for small μ.

With this result at hand, the decision was made to use classical control theory to design the gust alleviation system, with evaluation of the design to be made using the harmonic blance technique described in the appendix. Though this initial approach seemed adequate, closed-loop tests of an early feedback design were found to produce half-per-revolution oscillations in the flapping response at $\mu = 0.4$. Further investigation using Floquet theory showed that such a response could be predicted analytically, and henceforth all proposed IBC designs were checked for such phenomena using this method.

6.3 Design Synthesis

In order to understand the effects of each of the dynamic components present in the IBC system, it becomes necessary to consider each block of Figure 16 separately. If it were possible to sense blade flapping angle directly, and if we had an ideal pitch servo, the simplest IBC system would be a pure gain feedback or in effect, an electronic data-three hinge. The affect of such a design can be seen in the root-locus plot of Figure 17a and Bode plot of Figure 17b. As the gain is increased, the blade pole moves vertically away from the real axis, thus decreasing its damping. The Bode plot shows that as the gain is increased, the low frequency response is decreased at the expense of the flapping response of frequencies above rotor rotation. It should be emphasized again at this point that the behavior suggested by such classical control analysis assumes a single input, single output constant coefficient system, an assumption only valid at hovering flight. Hence, even though the frequency response indicated by the Bode plot of Figure 17b suggests that the superharmonic flapping response (arising due to forward flight) should be amplified, one cannot be certain of the actual response until the harmonic balance approach outlined in the appendix is applied to the feedback design. As Figure 17c indicates, there is amplification of the subharmonic response at low gust frequencies, a result that is perhaps counter-intuitive from the Bode amplitude plot of this simple system.

Although the IBC model rotor described here is instrumented (via a flexure and strain gauge mounted at the blade root fitting) to measure flap angle directly, it was felt that a more realistic means should be used to provide such a signal to the feedback path, one that could be realized on a full-scale machine. These considerations led to the choice of a tip mounted accelerometer as such a sensing element.

It was shown in the previous section that such an orientation contributes a complex conjugate pair of zeroes, located directly on the imaginary axis. Thus, as one increases the static sensitivity of this blade/accelerometer system, the blade pole moves directly over to this complex zero, reducing its damping while not significantly changing its natural frequency, as can be seen in Figure 18a. Figure 18b shows that because of the accelerometer's amplification of blade flapping accelerations at frequencies above rotor rotation, it appears possible (given an ideal servo) to attenuate high frequency flapping perturbations as well as low frequency disturbances. Figure 18c indicates that this system is indeed a good one, since it halves both the excitation and superharmonic responses, while leaving the subharmonic essentially unchanged. For the sake of comparison, the static sensitivity selected is the same as for the blade-only case of Figure 17 so that the effect of the added dynamics is illustrated only.

But these two design studies are unrealistic since they do not consider the effects of the pitch actuator dynamics. Like any physically realizable servo system, these dynamics are essentially low-pass, in that there is attenuation of high-frequency inputs. Thus, because this actuation system is located in the feedback path of Figure 16, high frequency flap peturbations will not be affected by the IBC system since the feedback path is essentially "broken" at the servo block. The challenge, then, is to configure the actuator to have a break frequency significantly larger than rotor rotational speed, and it is primarily for this reason that the second wind tunnel test was run half the speed of the first test.

Figures 19 through 21 consider the effect of varying the actuator's inner-loop gain upon the overall response of the IBC system. It can be

seen that as this inner loop gain is increased, the damping of the servo's complex conjugate poles decreases, and the flapping attenuation improves. This improvement is not significant for increases beyond those of Figure 20, as can be seen from comparisons of Figures 20c and 21c, and thus the system of Figure 20 was selected as the final gust alleviation system. A block diagram showing the frequency and damping of the elements of Figure 16 is given in Figure 22.

SECTION 7

EXPERIMENTAL RESULTS

7.1 Blade Response to Pitch

Figures 23a through 23c show the results of the first test plotted against theoretical response curves generated from substitution of the model rotor parameters into Equation 2. Though this first test included oscillations of blade pitch up to three times rotor rotational speed, these data are not shown here, as they are not of concern in the design of the gust alleviation system.

Looking first at the response curves for the hover condition (μ=0) in Figure 23a, it is readily apparent that although the actual magnitudes are anywhere from 50% to 75% less than predicted, the trends with increasing frequency are well matched. This reduction in response at excitation frequency can also be seen for the μ = 0.2 and μ = 0.4 cases, but the correlation improves as advance ratio increases.

Examination of the subharmonic and superharmonic response plots (Figures 23b and 23c) shows relatively good correlation between theory and experiment for the higher excitation frequencies. This fact seems to imply that the basic theory is correct, but it suggests that there are other factors present affecting the magnitude of the response at the excitation frequency.

A possible explanation of the discrepancies in Figure 23a would be inadequacies of the theoretical model. Reference 4 suggests a correction to the blade lift coefficient for a rotor in hovering flight due to the harmonic content of the rotor wake. This correction is independent of frequencies occurring at harmonics of the rotor rotation, but not for intermediate frequencies. Ignoring this last qualification, if one applies this correction to the test conditions considered, one obtains a flapping response quite similar to that observed in the test data.

The nonlinear fluctuation of the test results with change in collective setting might best be explained as follows: While data points for the settings of θ_o of 6.8 and 8.6 degrees match the trend of decreasing harmonic

wake effect with increasing inflow, the case of zero collective angle could very well represent a flight condition where the rotor blades pass through their own wake, and thus the rotor flow field becomes more complex than that described in Reference 4.

7.2 I.B.C. Gust Alleviation System Test

In the second wind tunnel test, in order to generate theoretical curves to plot alongside the flap response data, it was necessary to monitor the gust amplitude using a hotwire X-probe located directly above the rotor. A typical time history for the $\mu = 0.4$ case can be seen in Figure 24, and the spectral decomposition of this run is shown in Figures 25a and 25b. The information from the spectral analyses of the gust signal was thus used as input to the matrix relations given in the Appendix to produce the solid theoretical curves of Figures 26a through 26h. Several runs of the Fast Fourier Transform were performed over different segments of data for the open loop cases of the test, and the standard deviations for these data was used to construct the error bars about the data points.

Since the spectral analyses showed that the gust amplitude was not constant during a given run, a second set of theoretical curves are given in Figures 27a through 27h. These non-dimensionalize the flapping magnitude by the input gust amplitude, thus producing curves which more readily indicate any trends with gust frequency. The data for the various cases tested appears to match the theory reasonably well, and the correlation appears to improve with increasing advance ratio. Once again, the explanation for this trend may well be the reduction in any harmonic inflow effects due to an increase in total rotor inflow.

It should be noted here that Reference 1 seems to suggest that, in the expansion of the trigonometric approximation to the gust excitation terms, one may make the assumption $\cos \phi_G \simeq 1$ and $\sin \phi_G \simeq \phi_G$. Attempts to use this in the matrix relations described in the appendix produced theoretical flapping response curves that tended to grow with increasing excitation frequency. Upon power series expansion of $\sin \phi_G$ and $\cos \phi_G$, it was discovered that this initial approximation was rather inaccurate, due to the slow decay of higher order terms involving higher powers of nondimensional

frequency and reciptrocal advance ratio. Since the predicted response curves of Reference 1 do not show any notable increase with excitation frequency, it can only be assumed that the author did not use this rather crude approximation.

Figure 28 shows the effect of increasing open-loop static sensitivity (S_{OL}) upon the IBM gust alleviation system performance. It was originally thought that possible harmonic wake effects upon the model blade's flapping response to pitch input would dramatically lower the feedback gain so that the expected system performance would not be realized. Fortunately, this fear was unjustified, as can be seen in the Figure, where reductions at the excitation frequency are close to those predicted analytically. For moderate to low excitation frequencies, these can be rapidly calculated by considering the block diagram of Figure 22.

Since the forward path between the flapping due to disturbance and the flapping output of the IBC system is unity, any and all gain, or static sensitivity, must appear between the output and the summing junction. Then, we have the relation for closed-loop static sensitivity as:

$$S_{C.L.} = \frac{1}{1 + S_{O.L.}}$$

and hence for open-loop static sensitivity values of 0, 0.4, 0.8 and 1.2, we obtain closed-loop static sensitivity values of 1, 0.71, 0.56 and 0.45 respectively. This number subtracted from unity gives the fractional reduction in flapping response to be expected from the particular system.

As yet another means of comparison, Figure 29 shows the flapping response for the design point IBC gust alleviation system, with increased Lock number and 40% gust amplitude from that of Figure 20. The most interesting point to note is that for a full-scale rotor the increase in damping due to the increase in Lock number results in the flapping at excitation frequency being the predominant response. Also, with increased blade damping, it becomes possible to use larger feedback gain values for the same stability levels, and as a consequence the IBC system improves with increased scale effects.

SECTION 8

CONCLUSIONS

Comparison between theory and experiment indicates that the theory of this paper is satisfactory for the purposes of IBC gust alleviation system design.

The use of an accelerometer as blade motion sensor is shown not only to be feasible, but to have unique advantages in the IBC system.

The experimental results show that substantial alleviation of rotor blade response to gusts is possible.

Successful application of the IBC system to gust alleviation has motivated subsequent application of the system to blade vibration-alleviation investigations.

REFERENCES

1. Yasue, M., "Gust Response and Its Alleviation for a Hingeless Helicopter Rotor in Cruising Flight", MIT ASRL TR 189-1, September 1978.

2. Vehlow, C.A., "Experimental Investigation of Gust Response of Hingeless Helicopter Rotors", S.M. Thesis, Dept. of Aeronautics and Astronautics, Massachusetts Institute of Technology, May 1977.

3. Kretz, M., "Research in Multicyclic and Active Control of Rotary Wings", Vertica, 1, 2, 1976.

4. Miller, R.H., "Rotor Blade Harmonic Air Loading", I.A.S. Paper No. 62-82, January 1962.

5. Ham, N.D., Bauer, P.H. and Lawrence, T.H., "Wind Tunnel Generation of Sinusoidal Lateral and Longitudinal Gusts by Circulation Control of Twin Parallel Airfoils", NASA CR-137547, August 1974.

6. Biggers, J.C., "Some Approximations to the Flapping Stability of Helicopter Rotors", JAHS, 19, 4, October 1974.

7. Banerjee, D. et al., "Parameter Identification Applied to Analytic Hingeless Rotor Modelling", JAHS, 24, 1, January 1979.

8. Peters, D.A. and Hohenemser, K.H., "Application of Floquet Transition Matrix to Problems of Lifting Rotor Stability", JAHS, 16, April 1971.

TABLE 1

DESCRIPTION OF THE ROTOR BALDE USED IN THE WIND TUNNEL TEST

Number of blades	1
Radius, R	2.031 ft
Chord, c	2 in
Lock number, γ	3.01
Solidity, σ	0.0231
Collective pitch, θ_o	0, 6.8, 8.6 deg (first test)
	8 deg (second test)
Shaft tilt angle in cruising flight, α_s	10 deg forward
Lift-curve slope, a	5.73
Drag coefficient, C_{d_o}	0.012
Rotational speed, Ω	105 rad/sec (first test)
	53 rad/sec (second test
Built-in blade angle of twist, $\theta_{T\omega}$	8 deg (linear)
Elastic axis	33% chord
Aerodynamic center	25% chord
Hinge offset	2 in

TABLE 2

WIND TUNNEL TEST MATRIX

(FIRST TEST)

TUNNEL VELOCITY ADVANCE RATIO, μ	0 MPH 0.0	30 MPH 0.2	60 MPH 0.4
TEST CONDITION			
$\theta_{0.75} = 0°$ $\alpha_{SHAFT} = 0°$ RUN NOS.:	0,.5,1,2,5, 10,20,30,50 Hz PITCH INPUT 50-58	0,.5,1,2,5, 10,20,30,50 Hz PITCH INPUT 33-41	0,.5,1,2,5, 10,20,30,50 Hz PITCH INPUT 42-49
$\theta_{0.75} = 6.8°$ $\alpha_{SHAFT} = 10°$ RUN NOS.:	" 77-85	" 68-76	
$\theta_{0.75} = 8.6°$ $\alpha_{SHAFT} = 10°$ RUN NOS.:	" 59-67		

TABLE 3

IBC FEEDBACK TEST MATRIX

$\theta_{0.75} = 8°$, $\alpha_{SHAFT} = 10°$, all cases

TUNNEL VELOCITY ADVANCE RATIO, μ	15 MPH 0.2	30 MPH 0.4
FEEDBACK STATIC SENSITIVITY, S_{oL}	ω/Ω = .1, .2, .3, .4, .5	ω/Ω = .1, .2, .3, .4, .5
0.0		
0.4 (50% DESIGN VALUE)	"	"
0.8 (100% DESIGN VALUE)	"	"
1.2 (150% DESIGN VALUE)	"	"

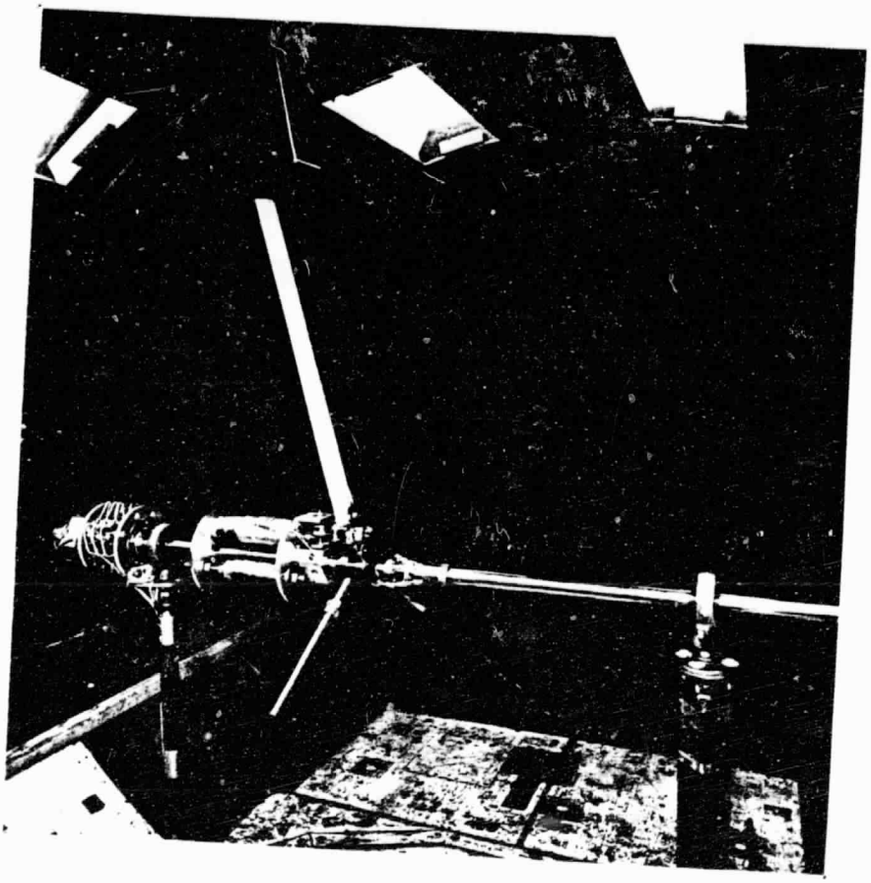

FIG. 1 INDIVIDUAL-BLADE-CONTROL MODEL ROTOR ASSEMBLY, UPSTREAM VIEW

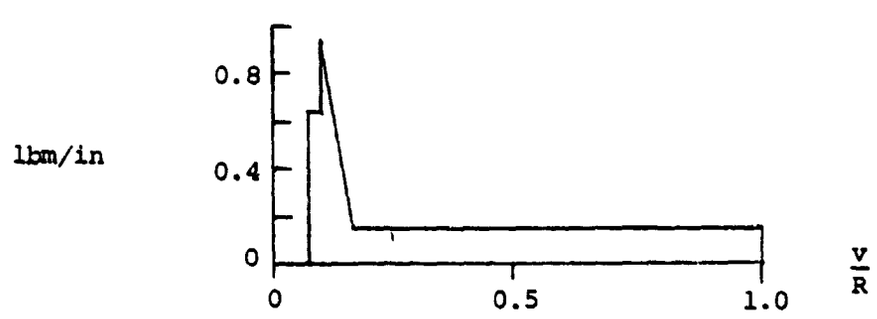

MASS DISTRIBUTION

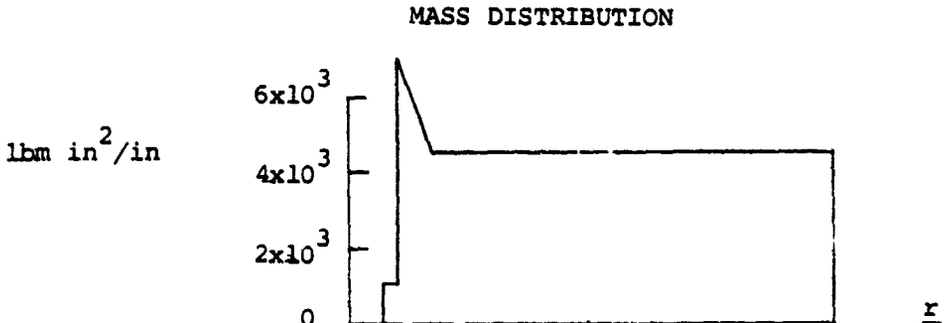

CROSS-SECTIONAL MOMENT OF INERTIA

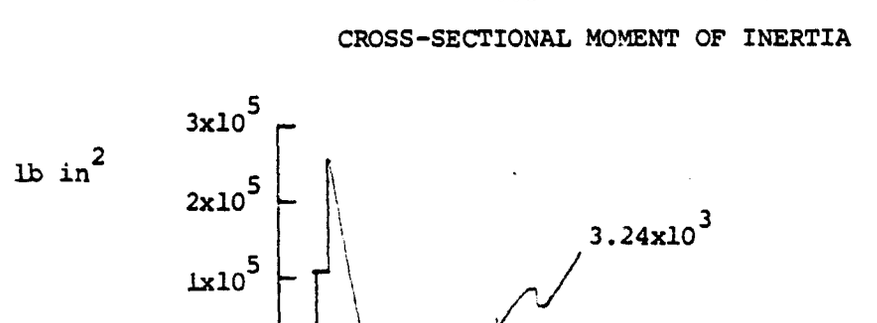

FLAPWISE STIFFNESS

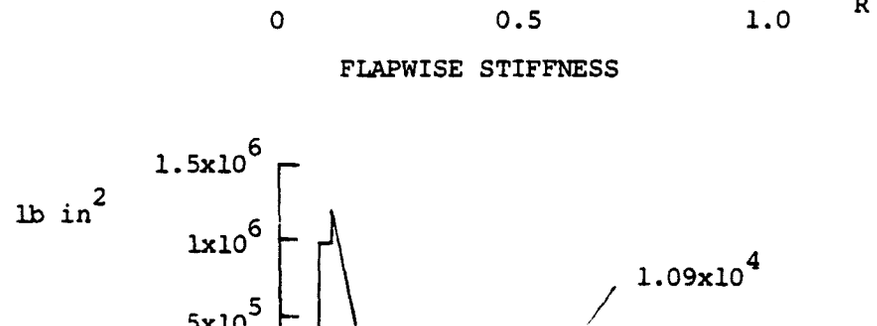

CHORDWISE STIFFNESS

FIG. 2 FORK ASSEMBLY AND BLADE PROPERTIES (HINGE POINT IS AT 0.082R)

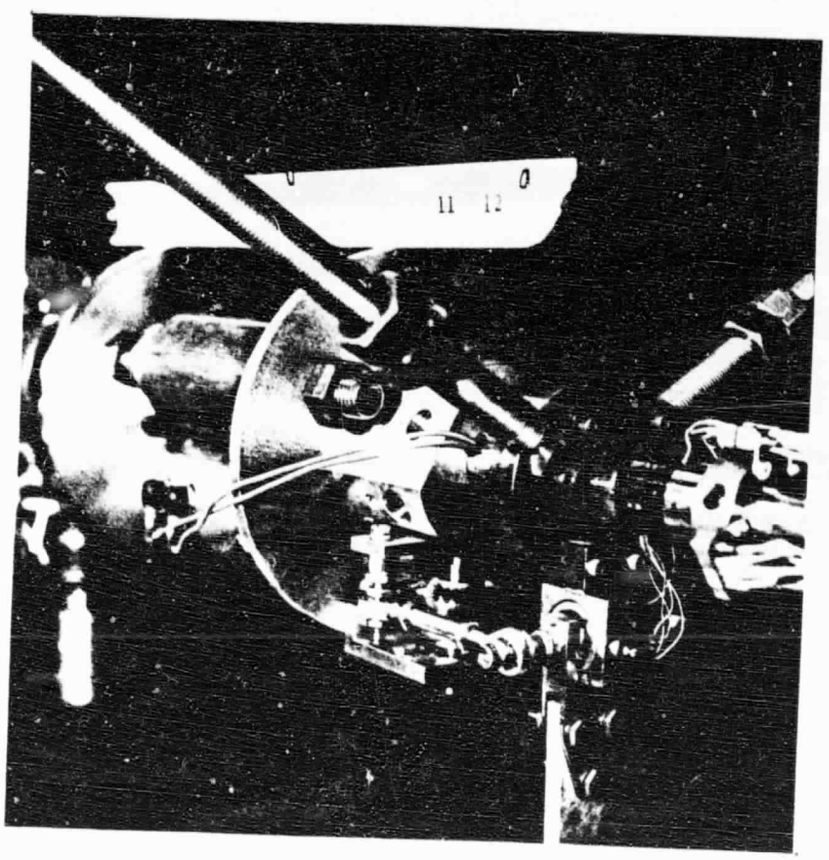

FIG. 3 PITCH ACTUATOR LINKAGE DETAIL, 3/4 VIEW

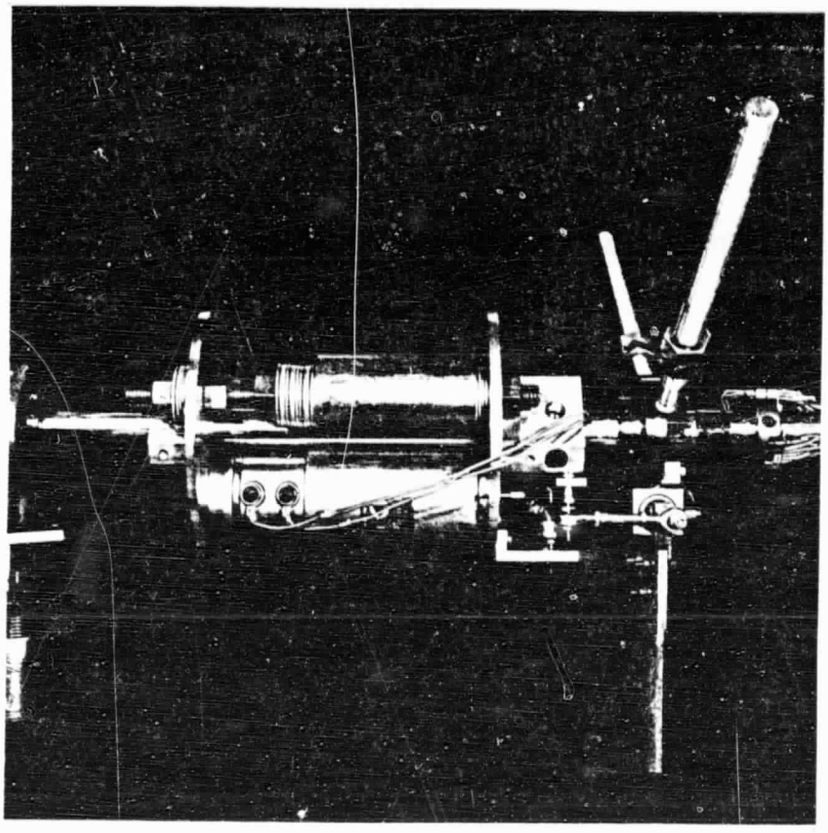

FIG. 4 SERVO MOTOR AND LINKAGE DETAIL, LEFT SIDE VIEW

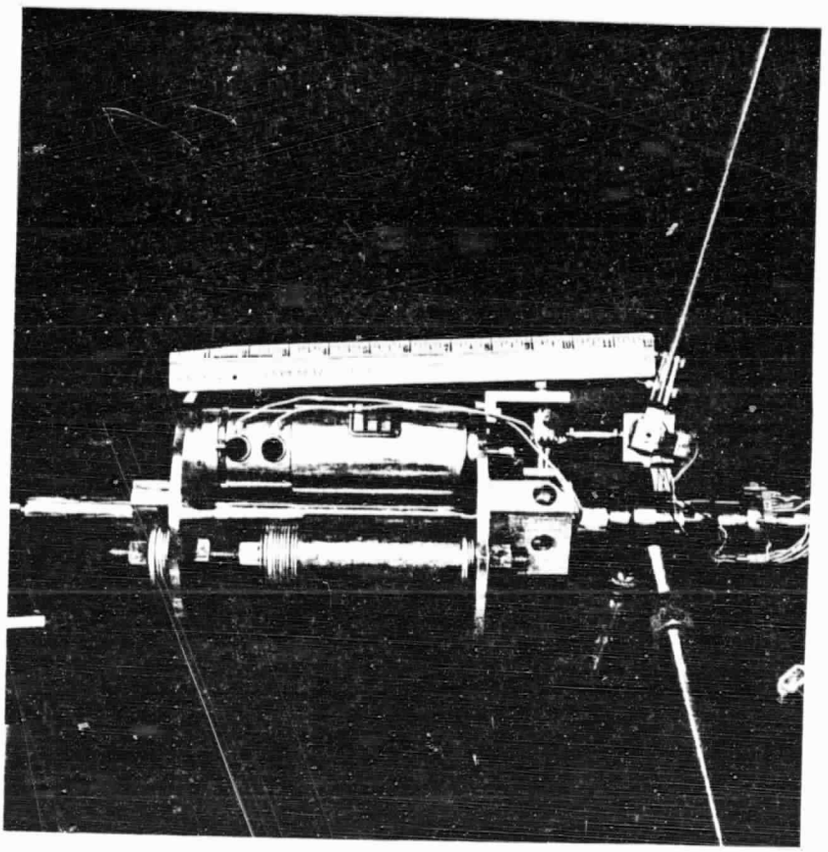

FIG. 5 SERVO MOTOR ASSEMBLY AND FLEXURE, RIGHT SIDE VIEW

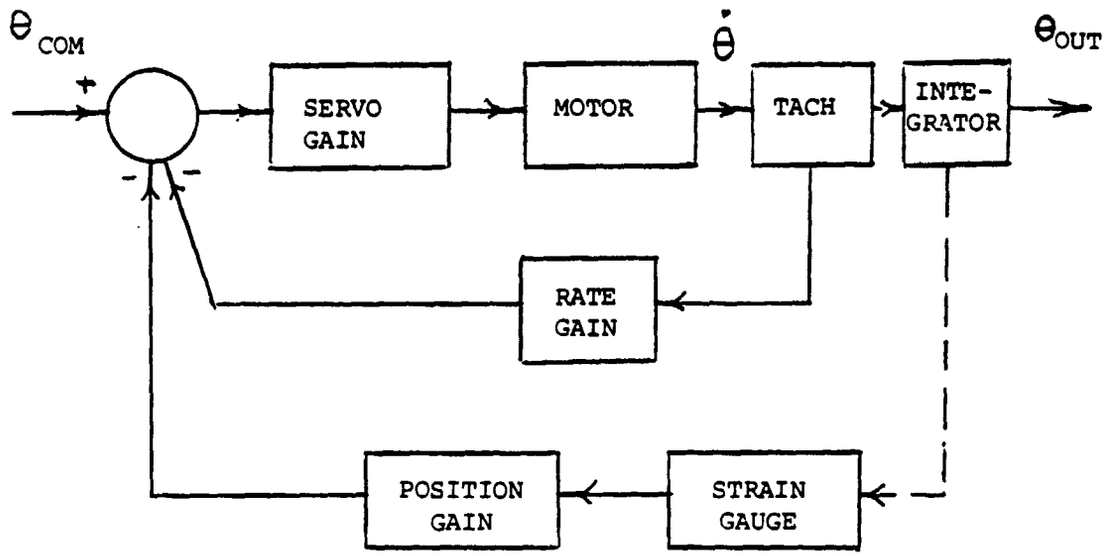

FIG. 6 SERVO SYSTEM BLOCK DIAGRAM

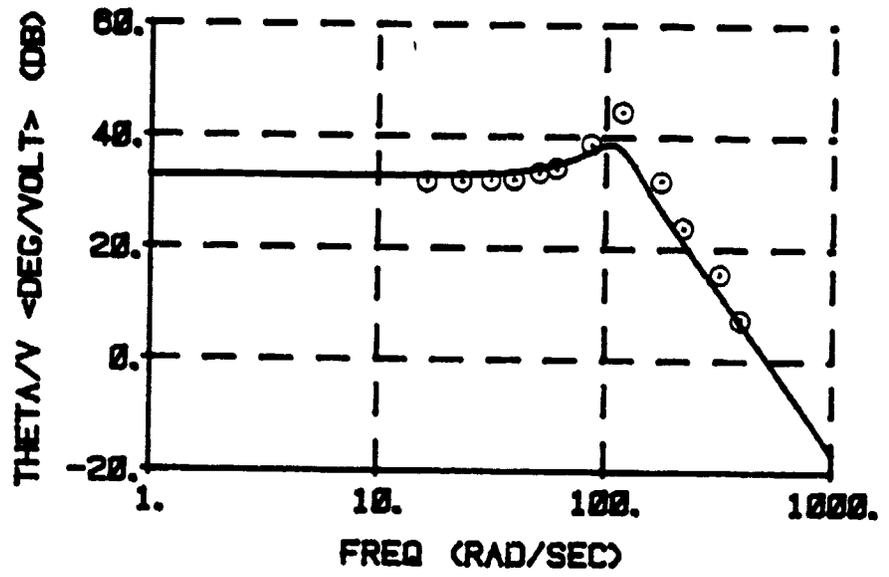

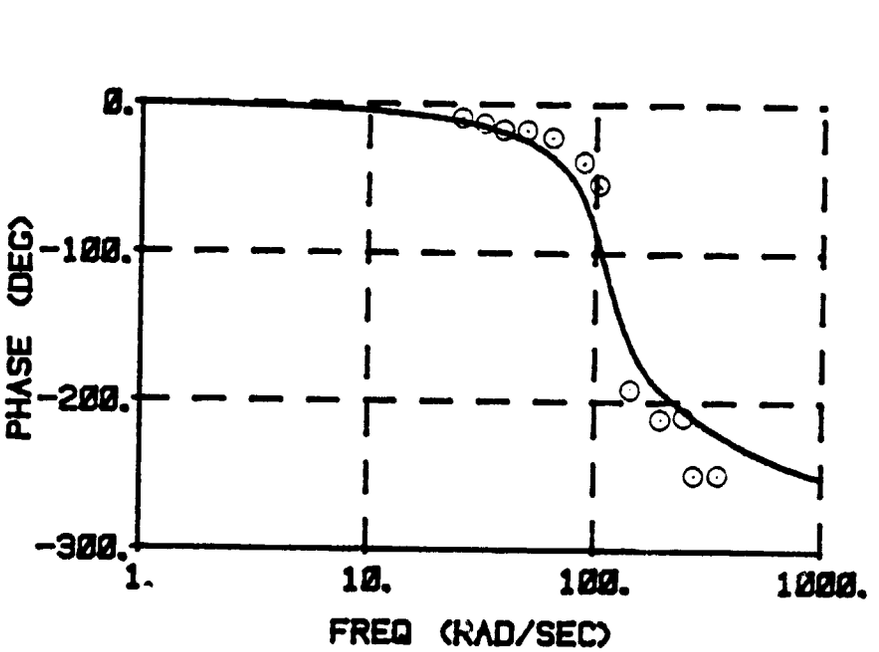

FIG. 7 FREQUENCY RESPONSE MATCHING, POSITION-ONLY FEEDBACK CONFIGURATION

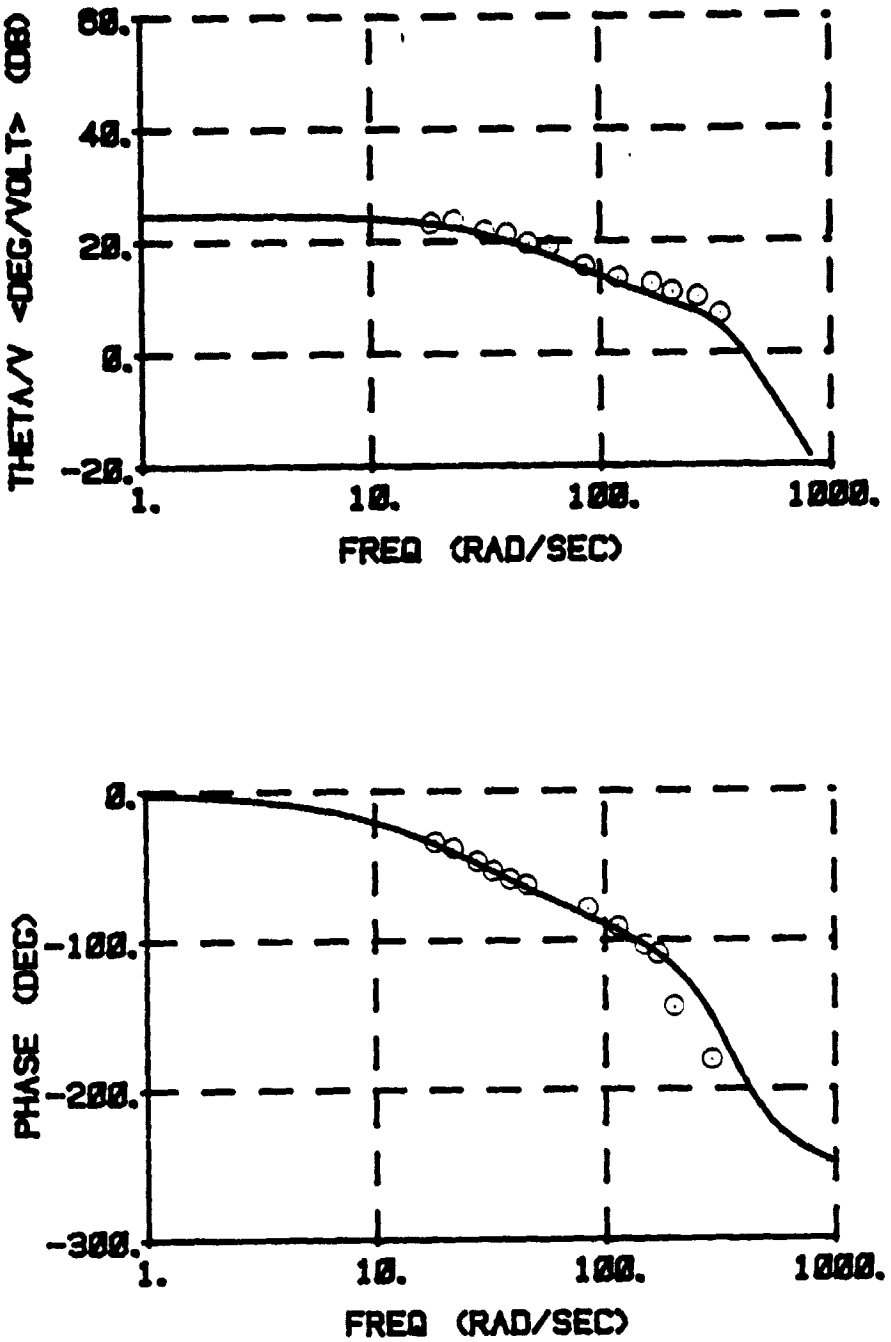

FIG. 8 FREQUENCY RESPONSE MATCHING, POSITION-PLUS-RATE FEEDBACK CONFIGURATION

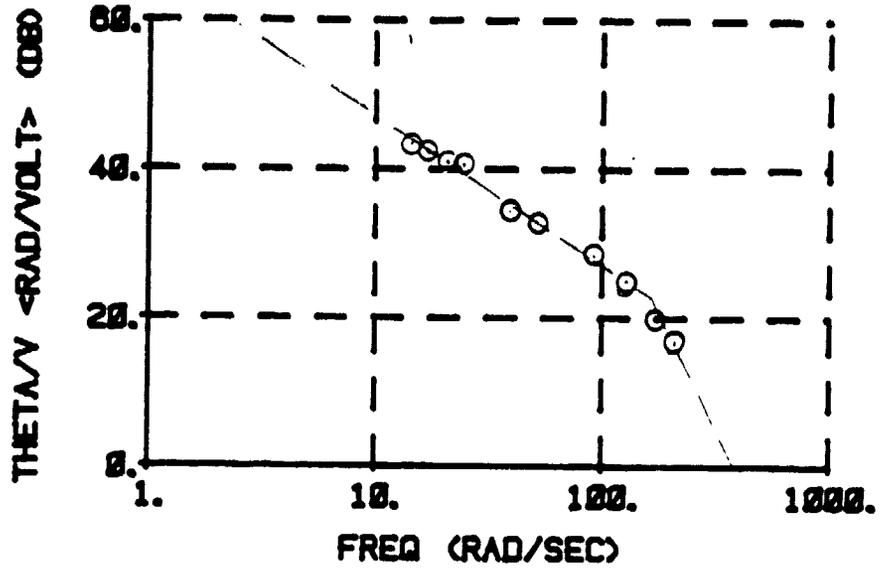

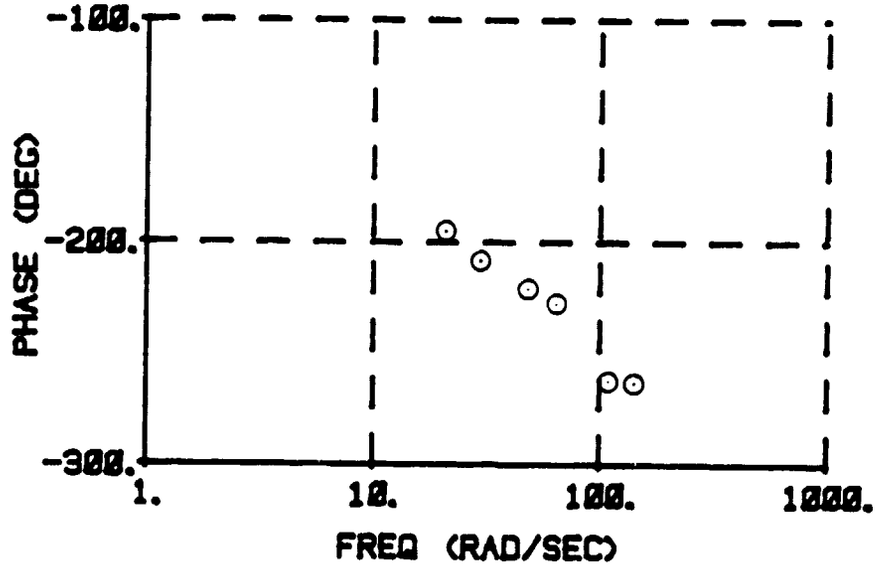

FIG. 9 OPEN LOOP SERVO MOTOR FREQUENCY RESPONSE

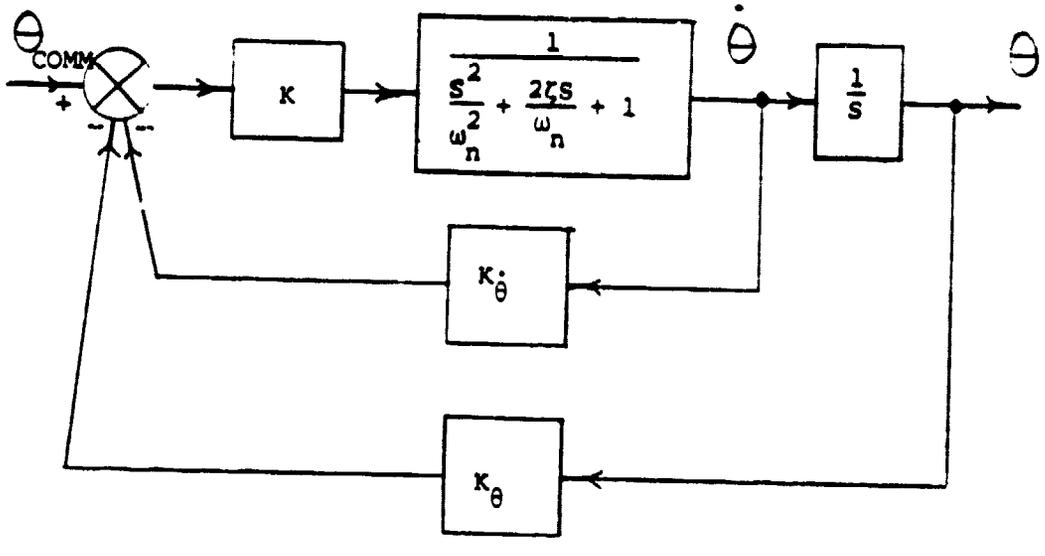

$\omega_n \doteq 166.5 \frac{RAD}{SEC}$ $\quad \zeta \doteq 1.0$

FIG. 10 SERVO ELEMENT TRANSFER FUNCTIONS

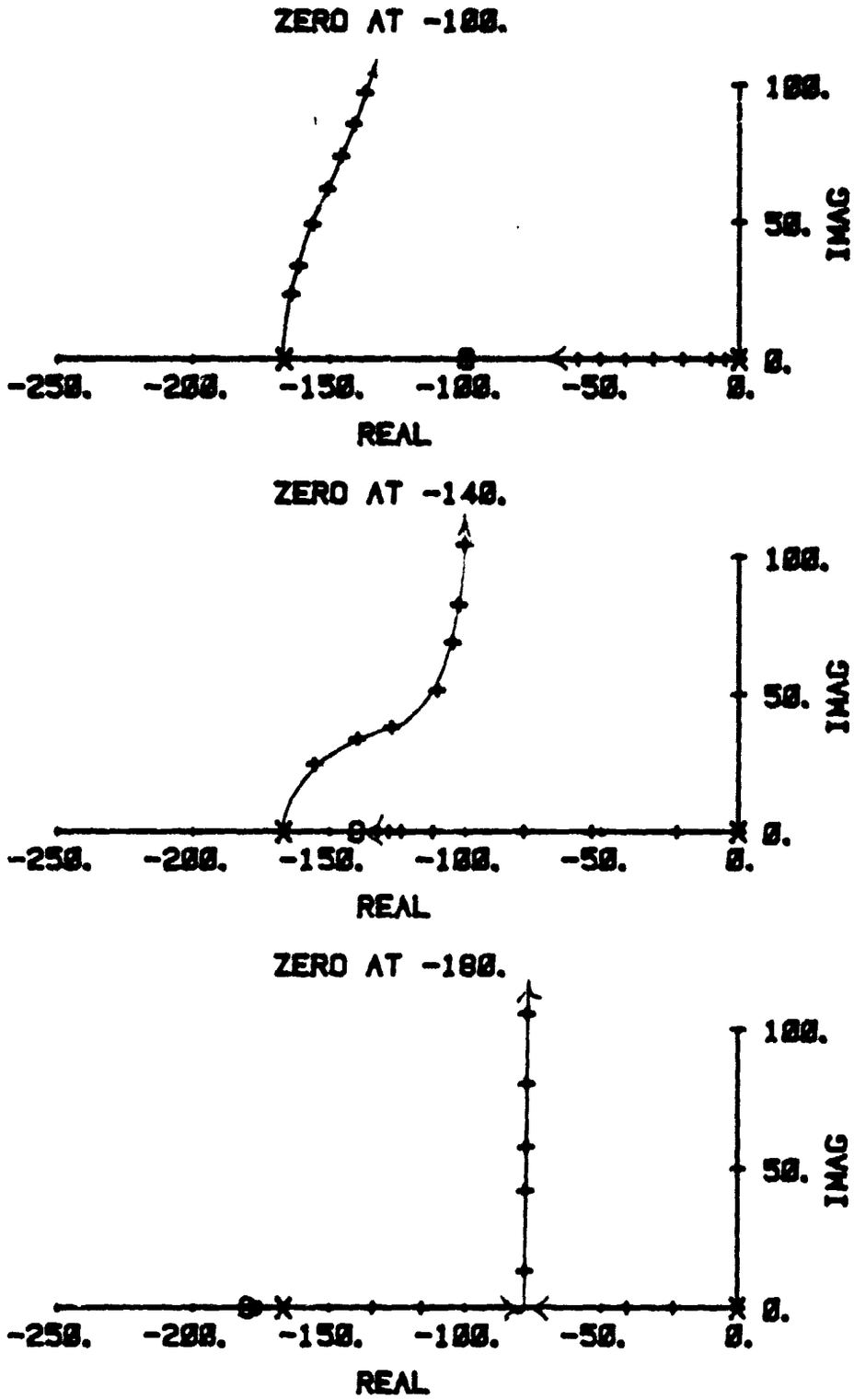

FIG. 11 ROOT LOCUS PLOT OF SERVO DESIGN PROBLEM

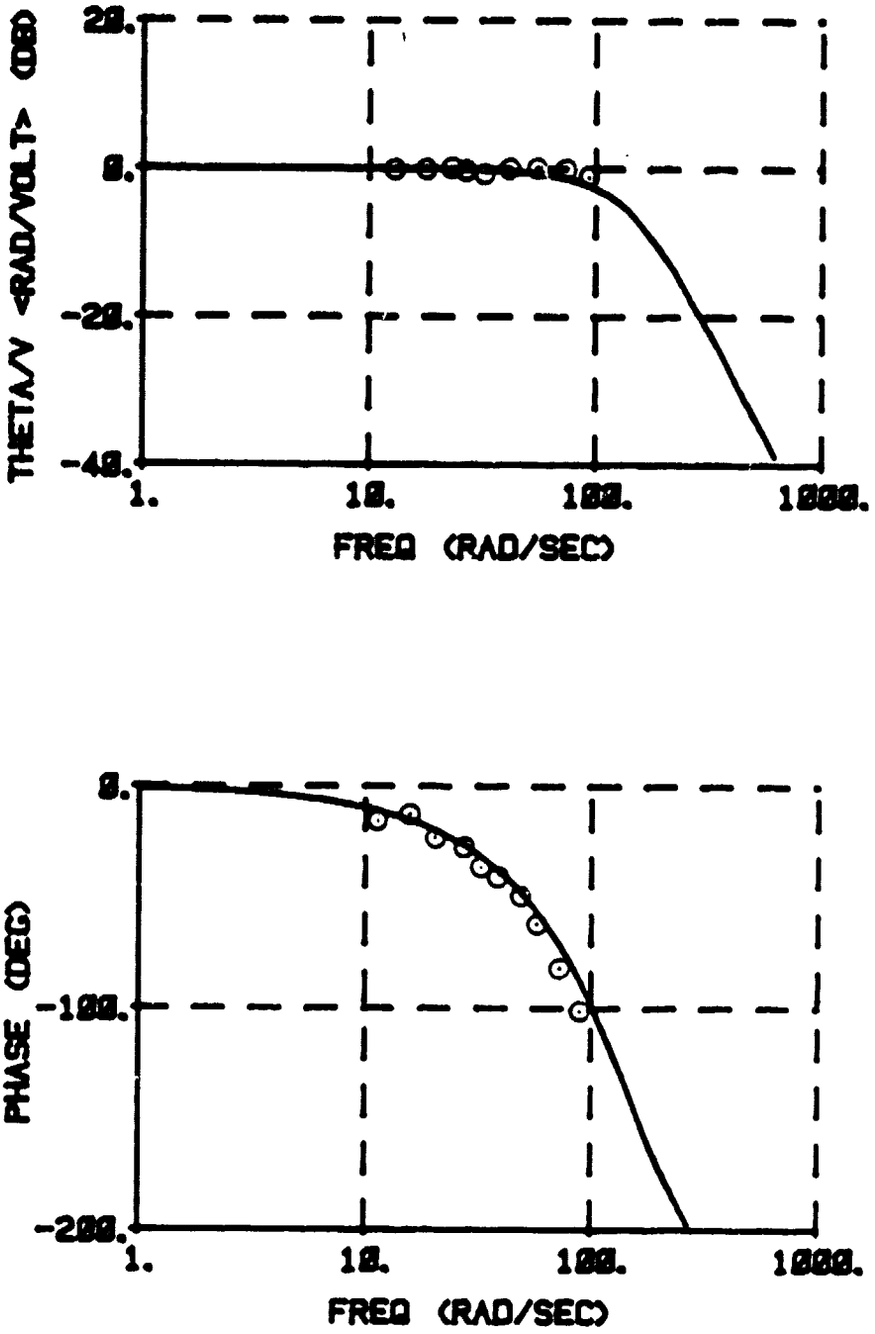

FIG. 12 SERVO FREQUENCY RESPONSE, FINAL CONFIGURATION

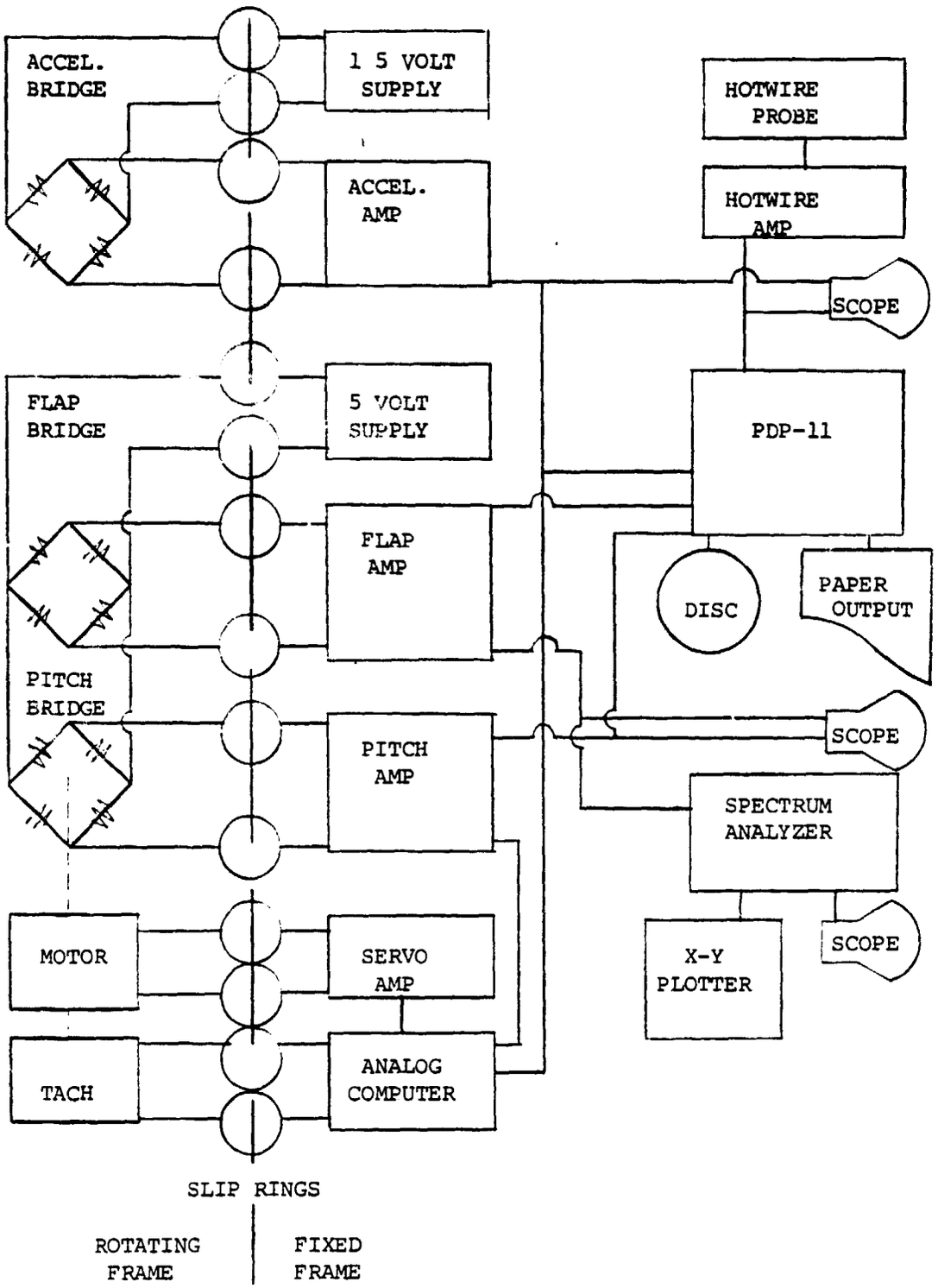

FIG. 13 INSTRUMENTATION FLOWCHART FOR WIND TUNNEL TESTS

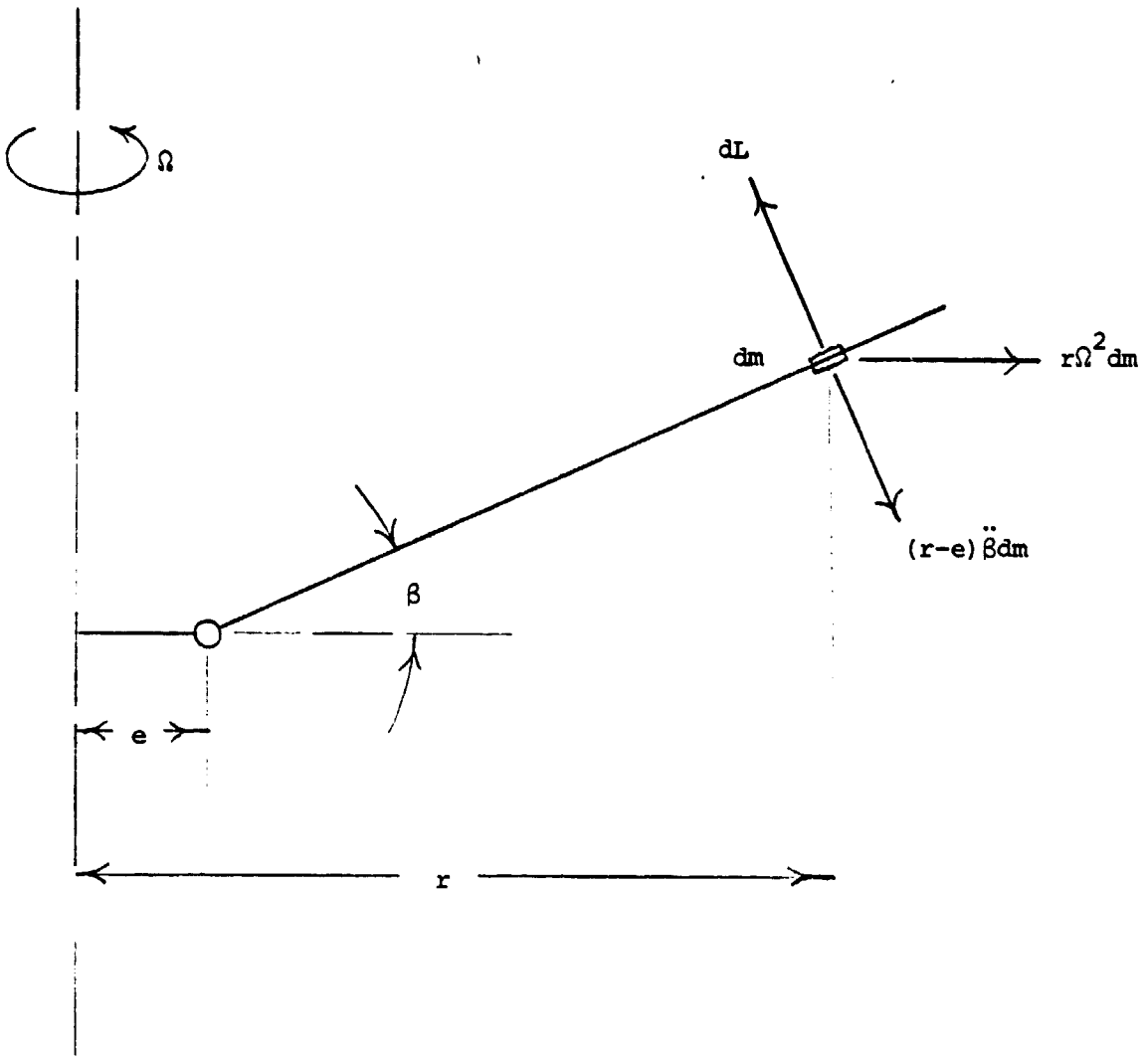

FIG. 14 BLADE ELEMENT FORCE SCHEMATIC

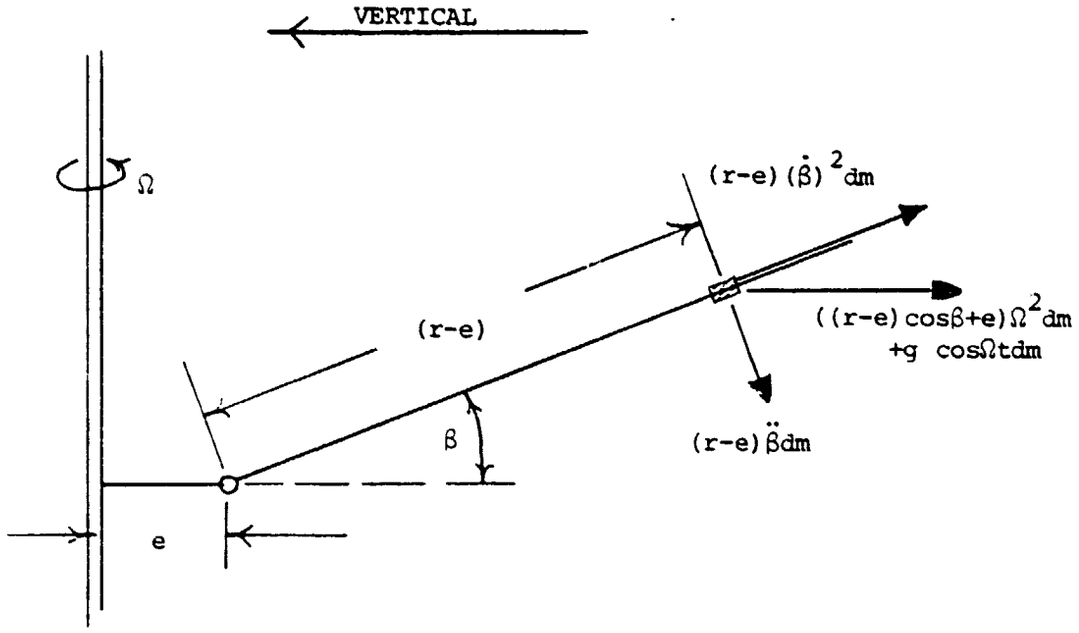

FIG. 15 MOTION FORCES ON BLADE ELEMENT

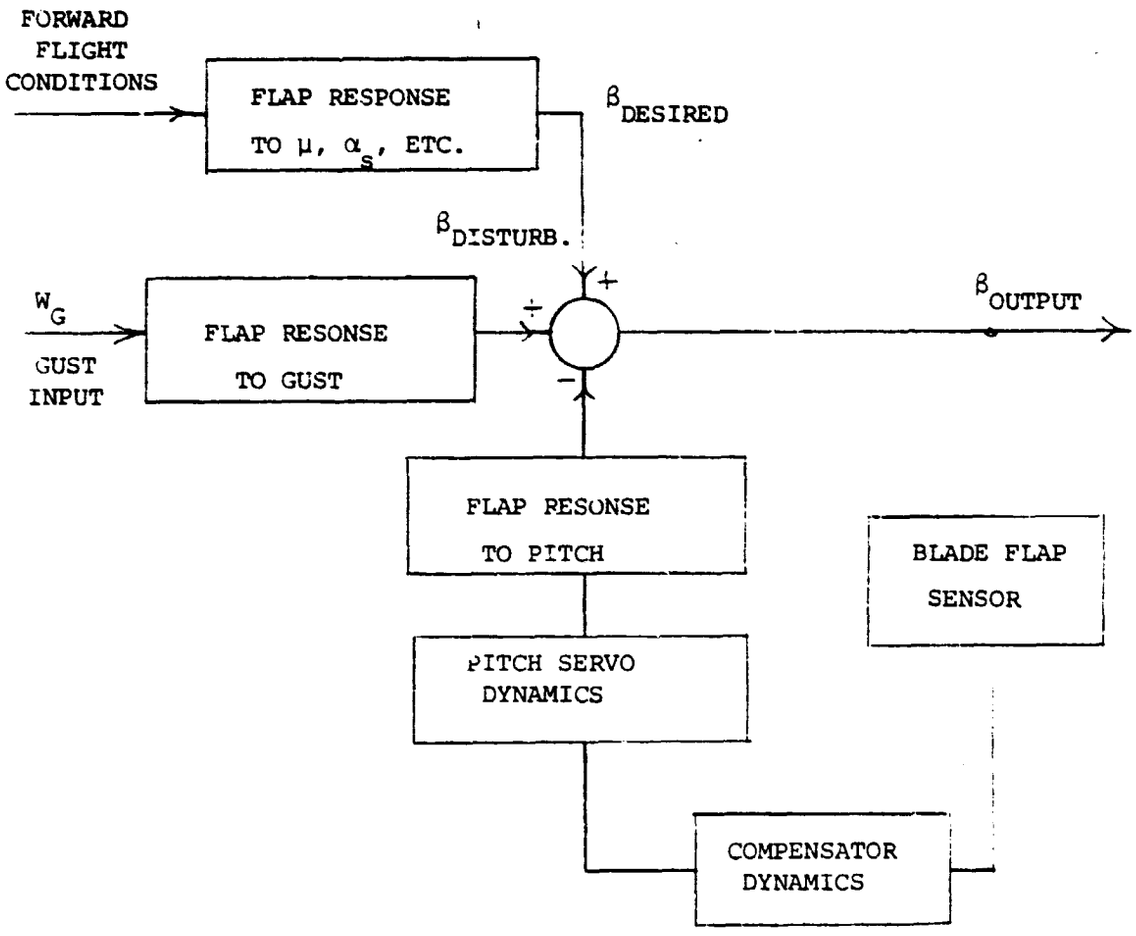

GOAL: $\beta_{OUTPUT} = \beta_{DESIRED}$

FIG. 16 I.B.C. SYSTEM BLOCK DIAGRAM

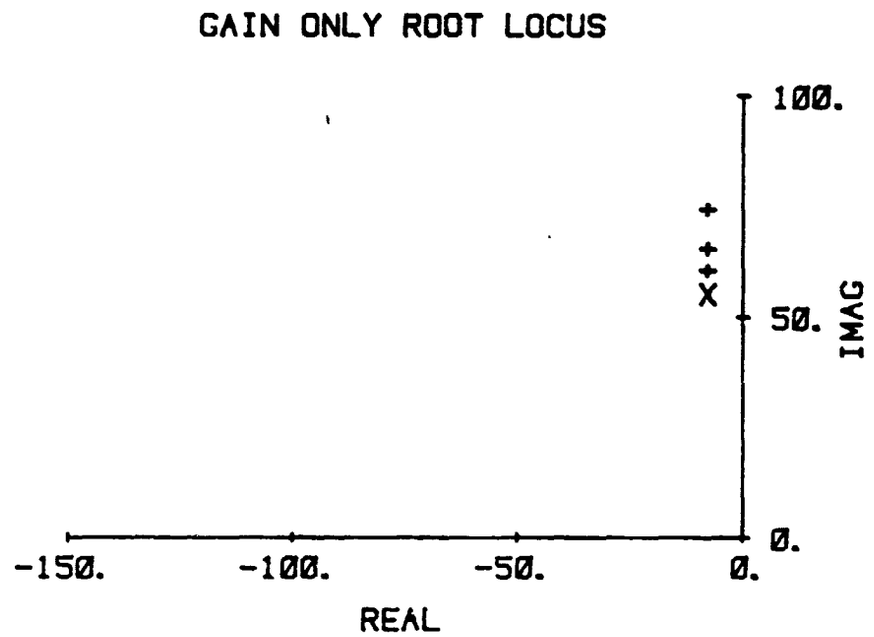

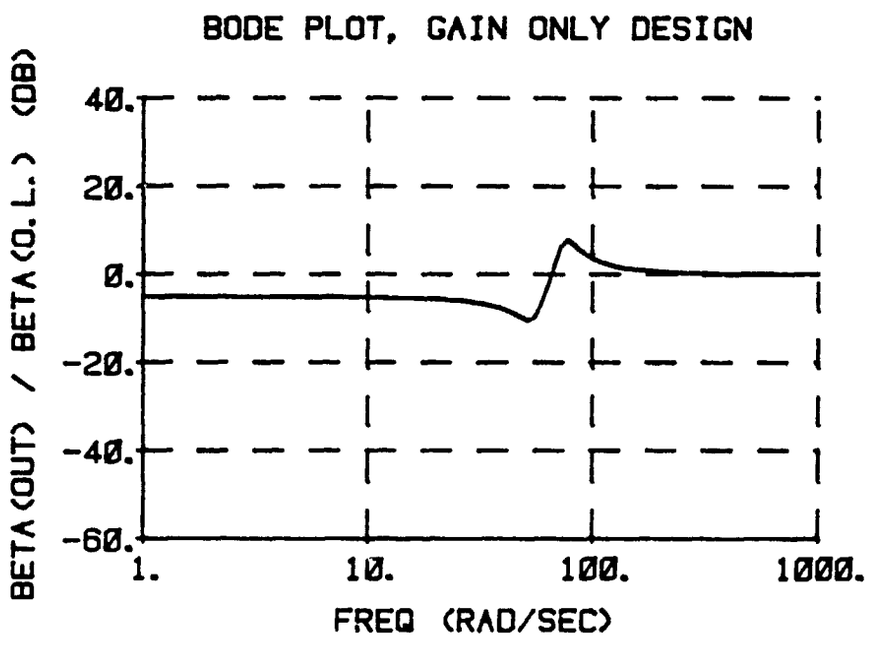

FIG. 17a, 17b I.B.C. GAIN ONLY FEEDBACK DESIGN

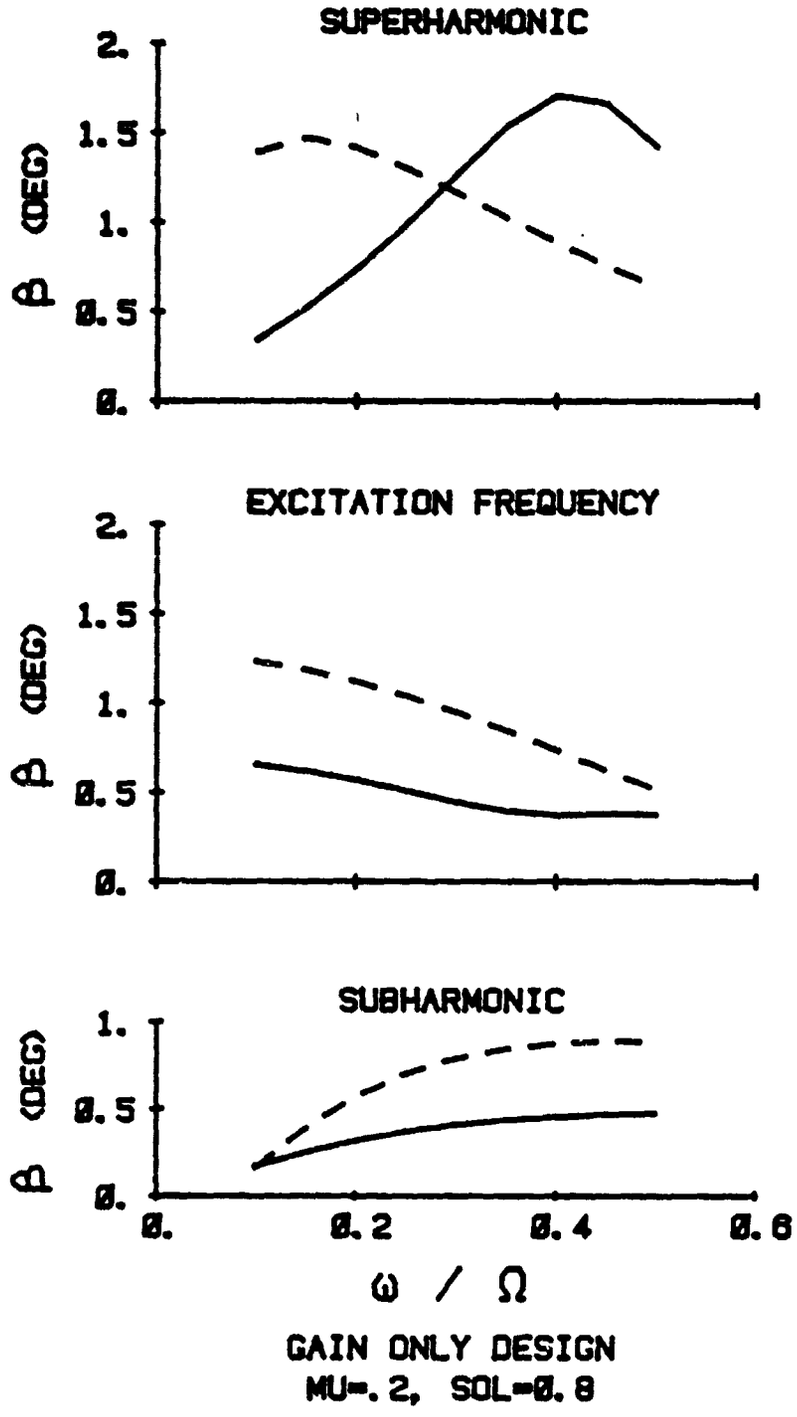

FIG. 17c I.B.C. GAIN ONLY FEEDBACK DESIGN

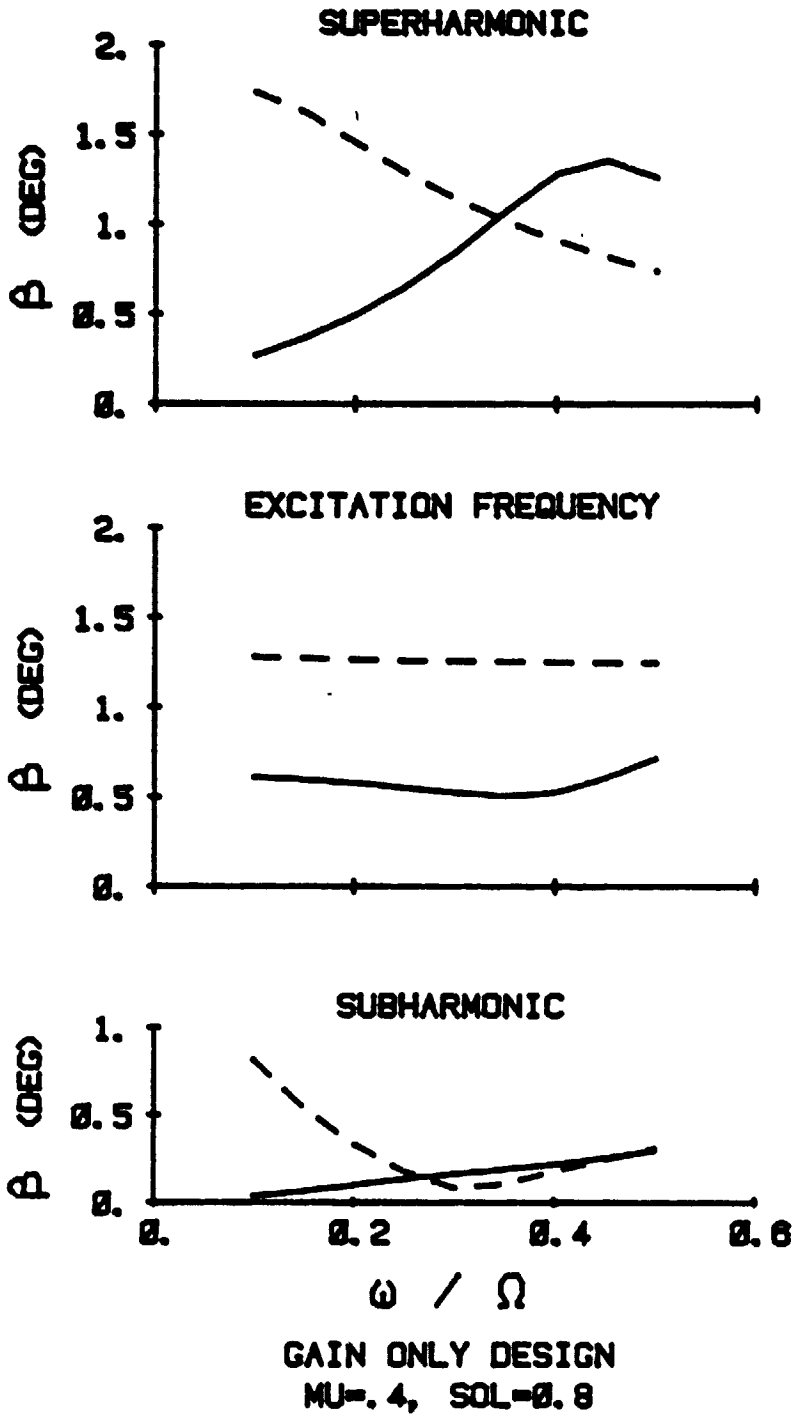

FIG. 17c (CONCLUDED)

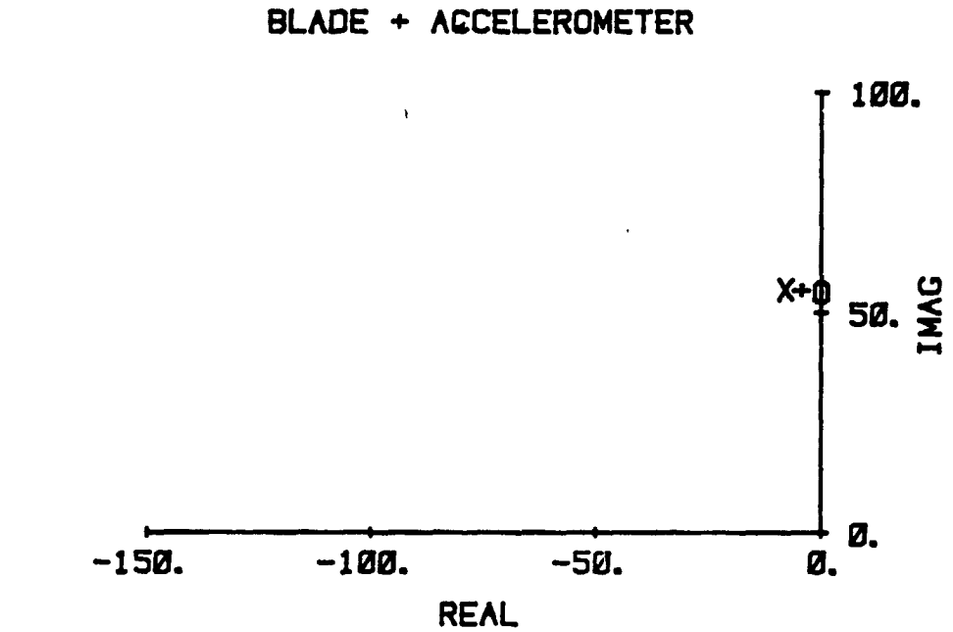

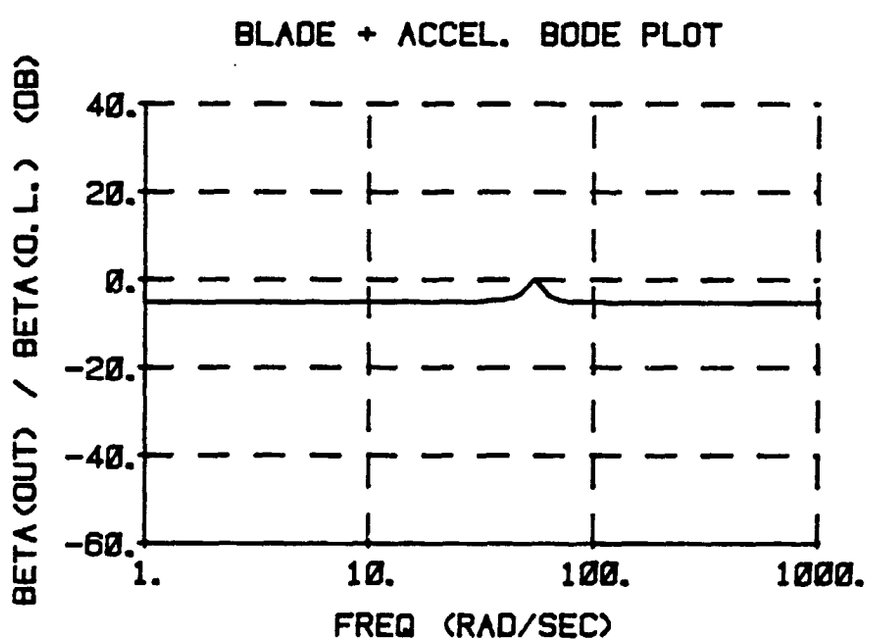

FIG. 18a, 18b BLADE PLUS ACCELEROMETER DESIGN

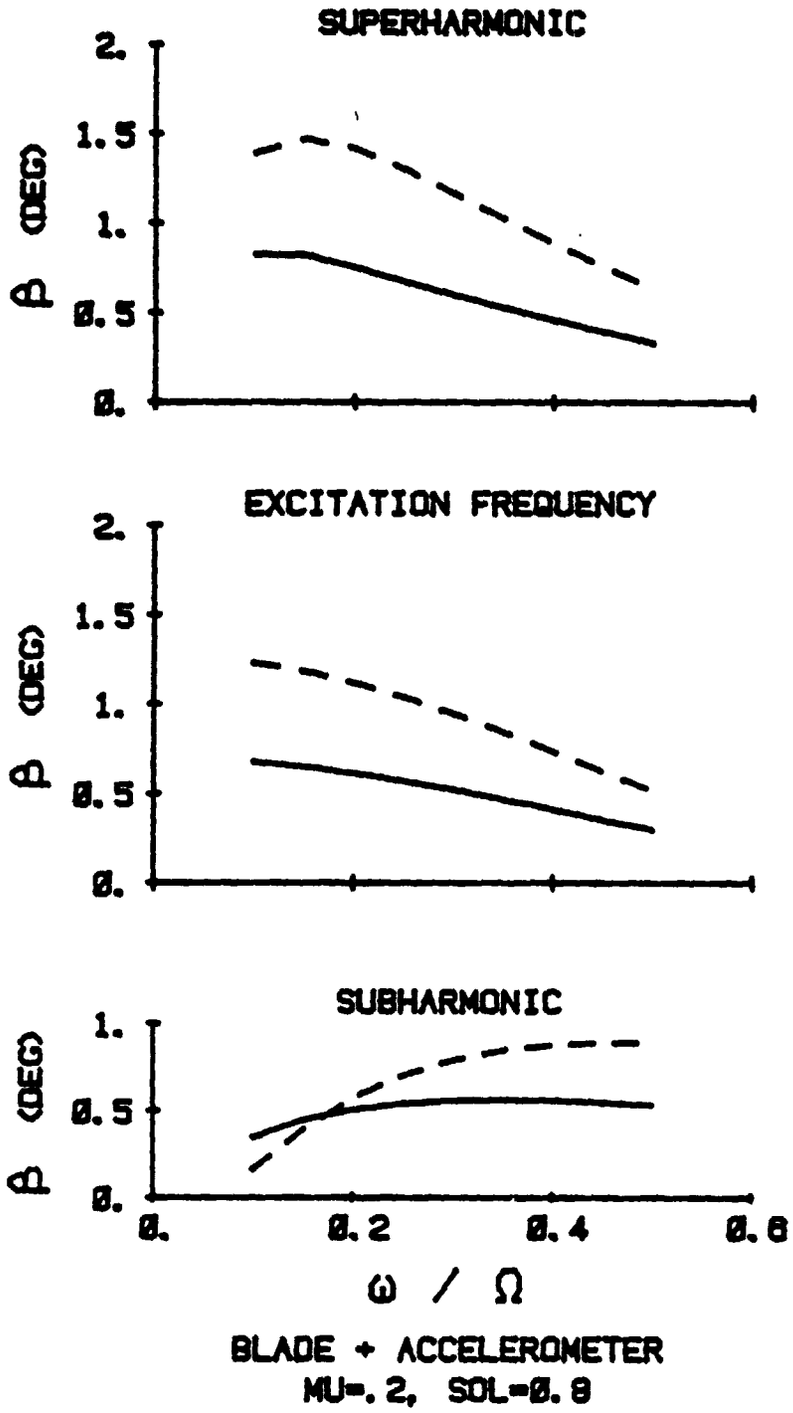

FIG. 18c (CONTINUED)

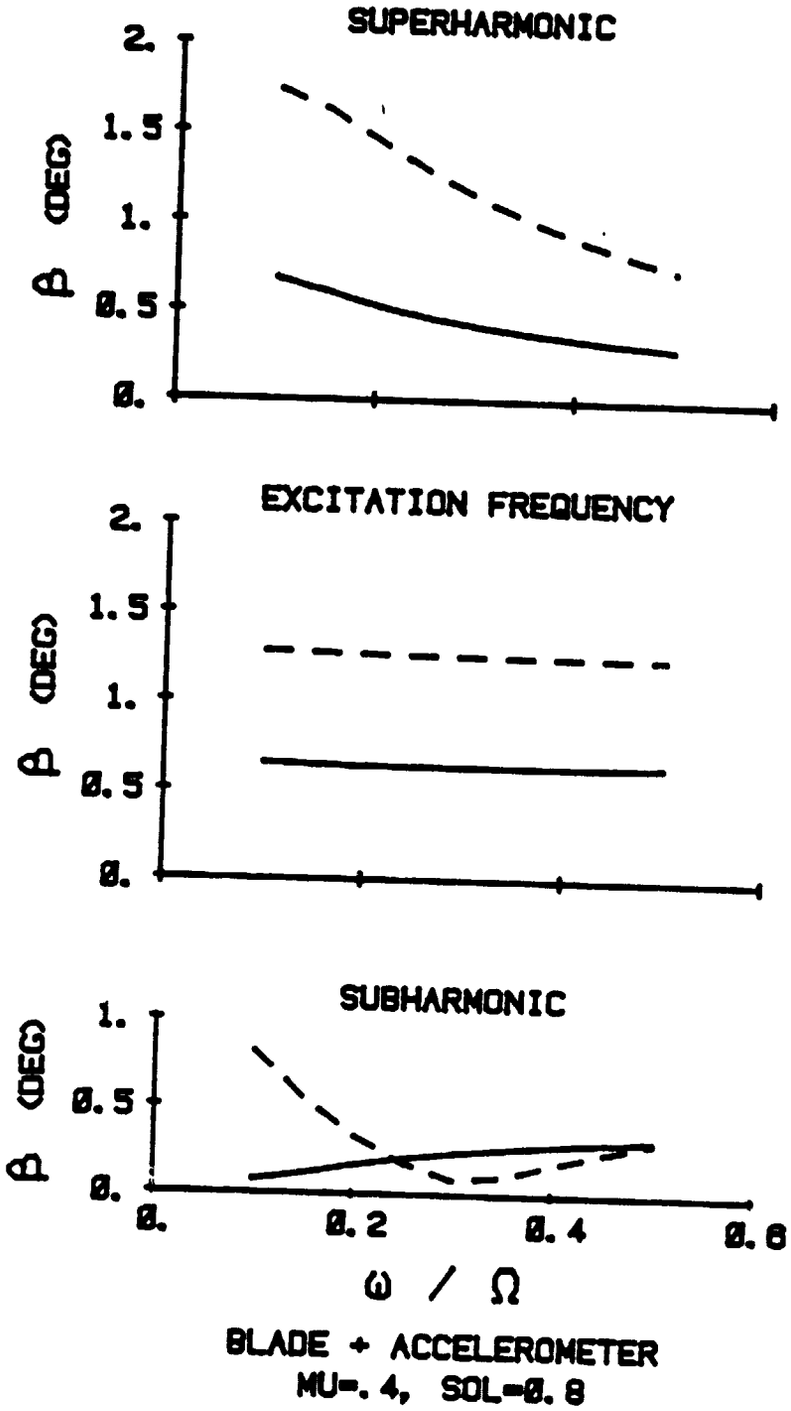

FIG. 18c (CONCLUDED)

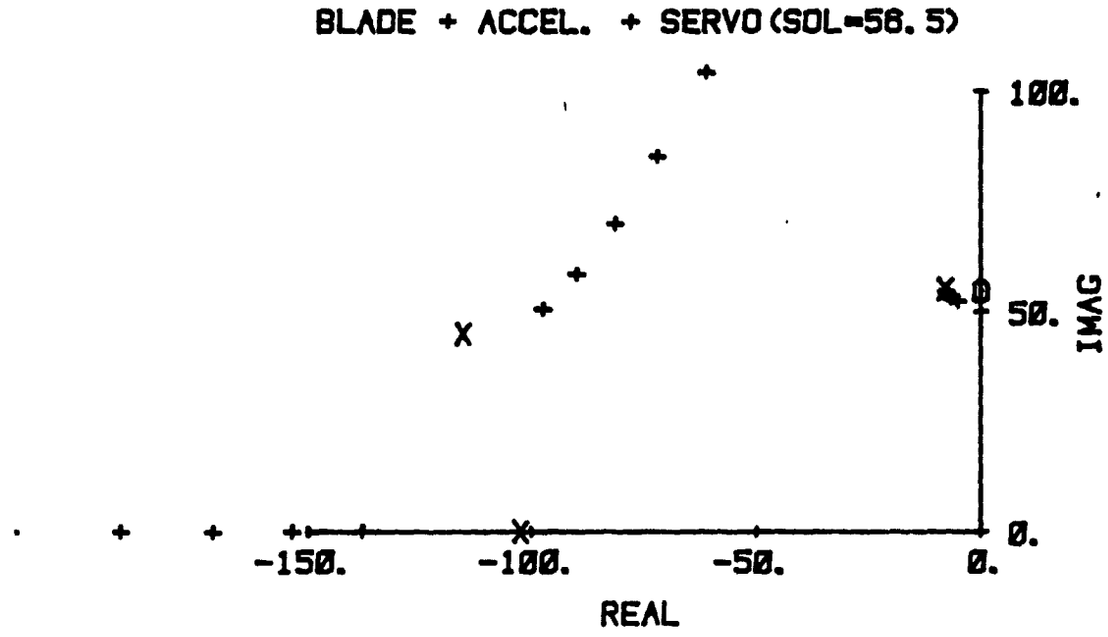

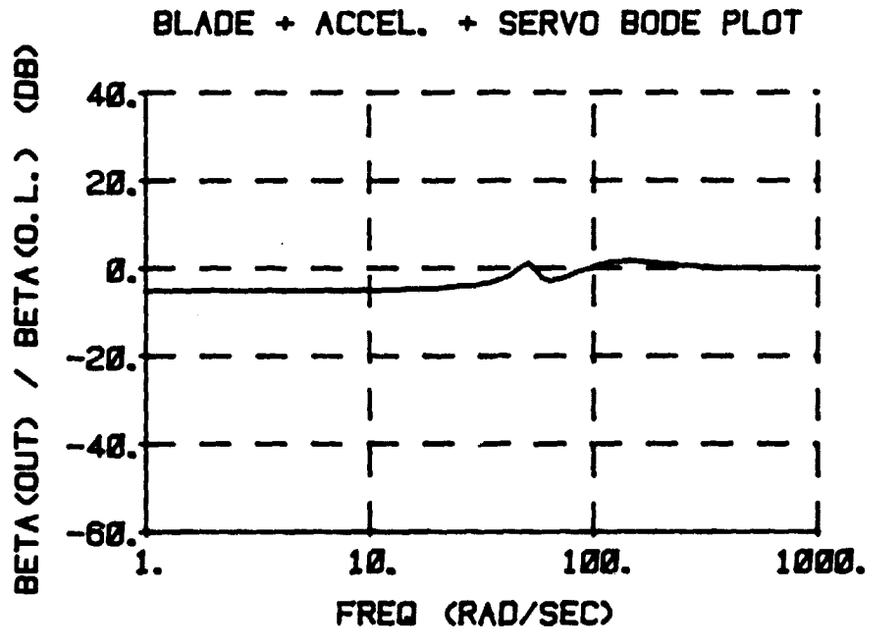

FIG. 19a, 19b BLADE, ACCELEROMETER, AND LOW-GAIN-SERVO DESIGN

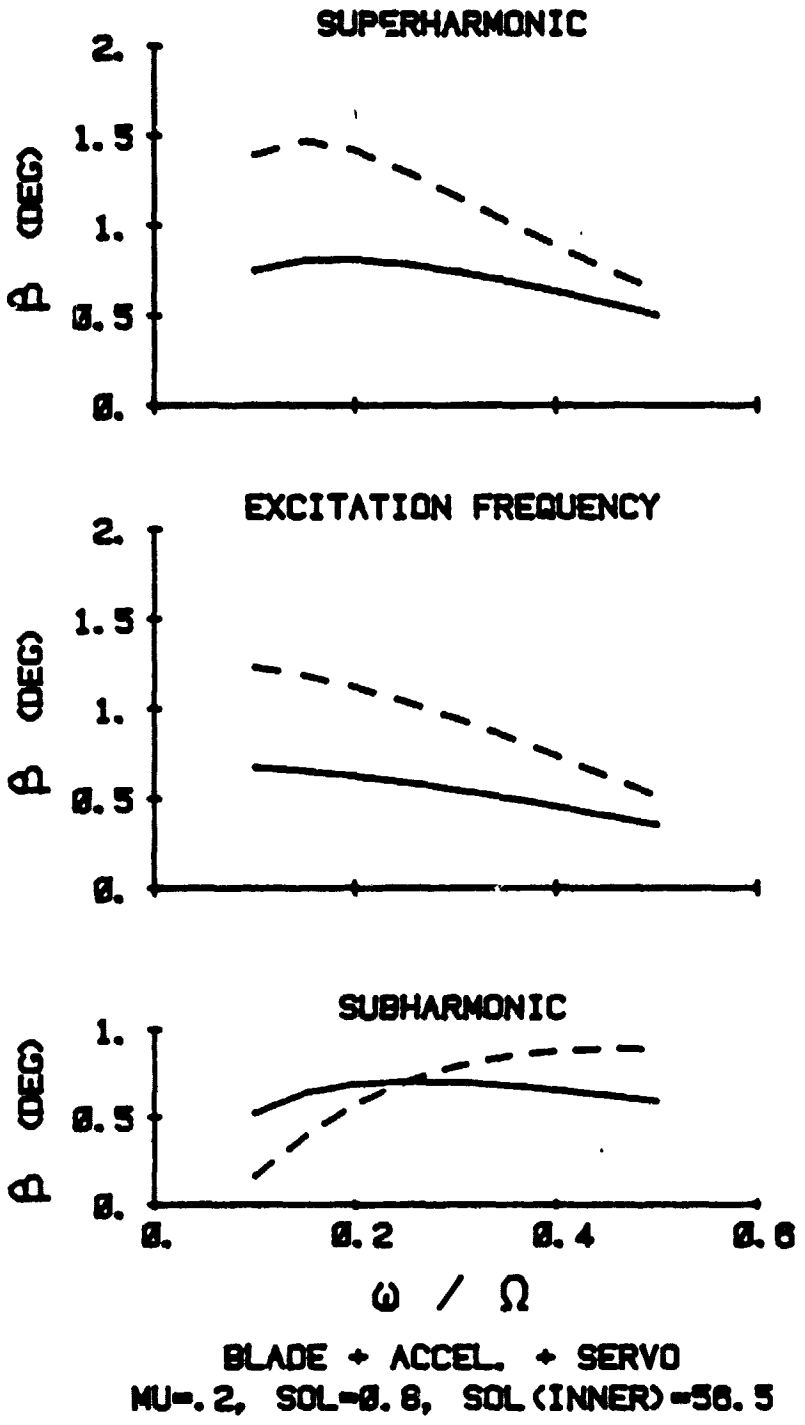

FIG. 19c (CONTINUED)

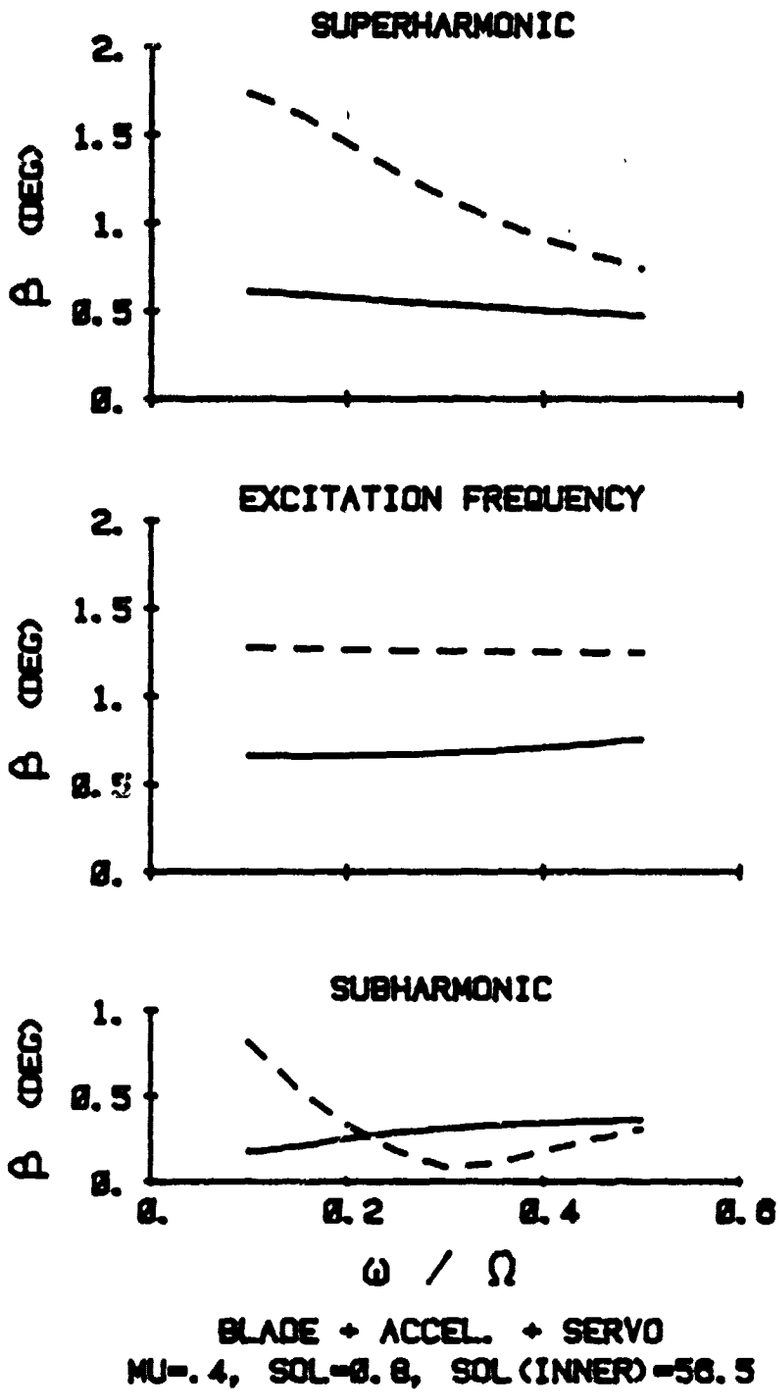

FIG. 19c (CONCLUDED)

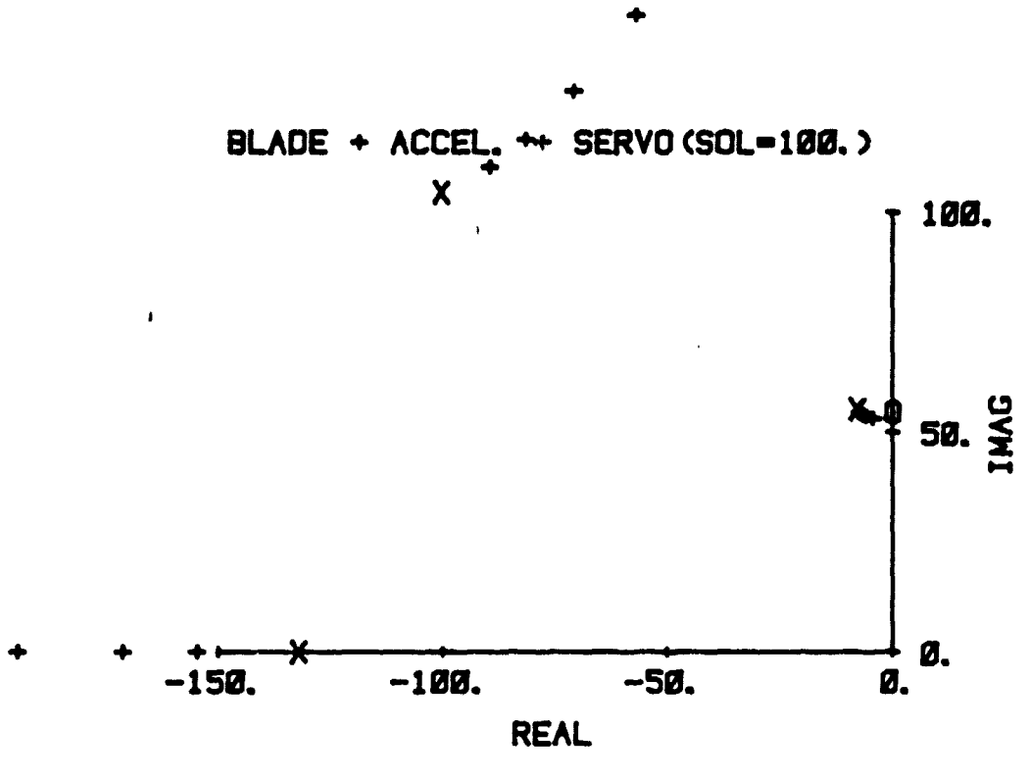

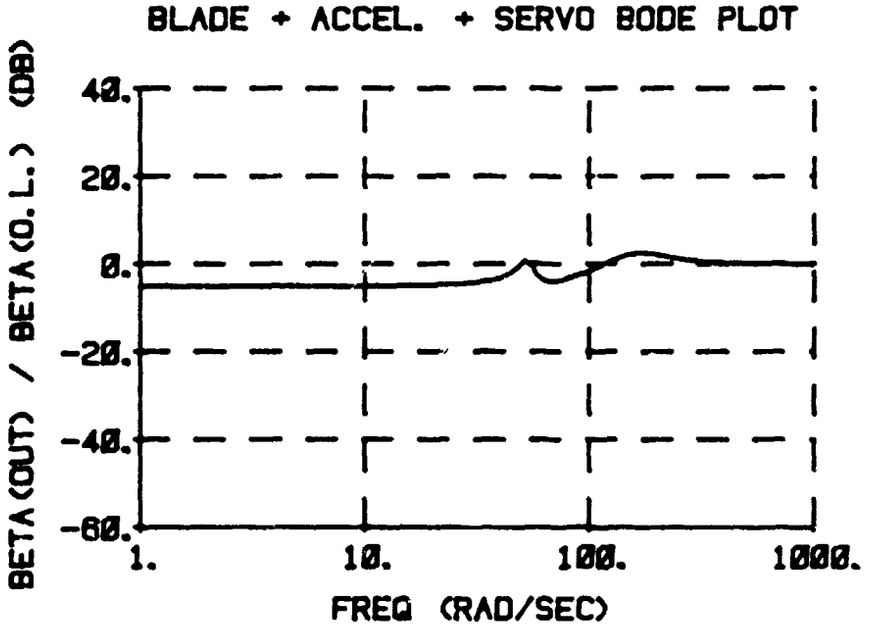

FIG. 20a, 20b BLADE, ACCELEROMETER, AND MEDIUM-GAIN-SERVO DESIGN

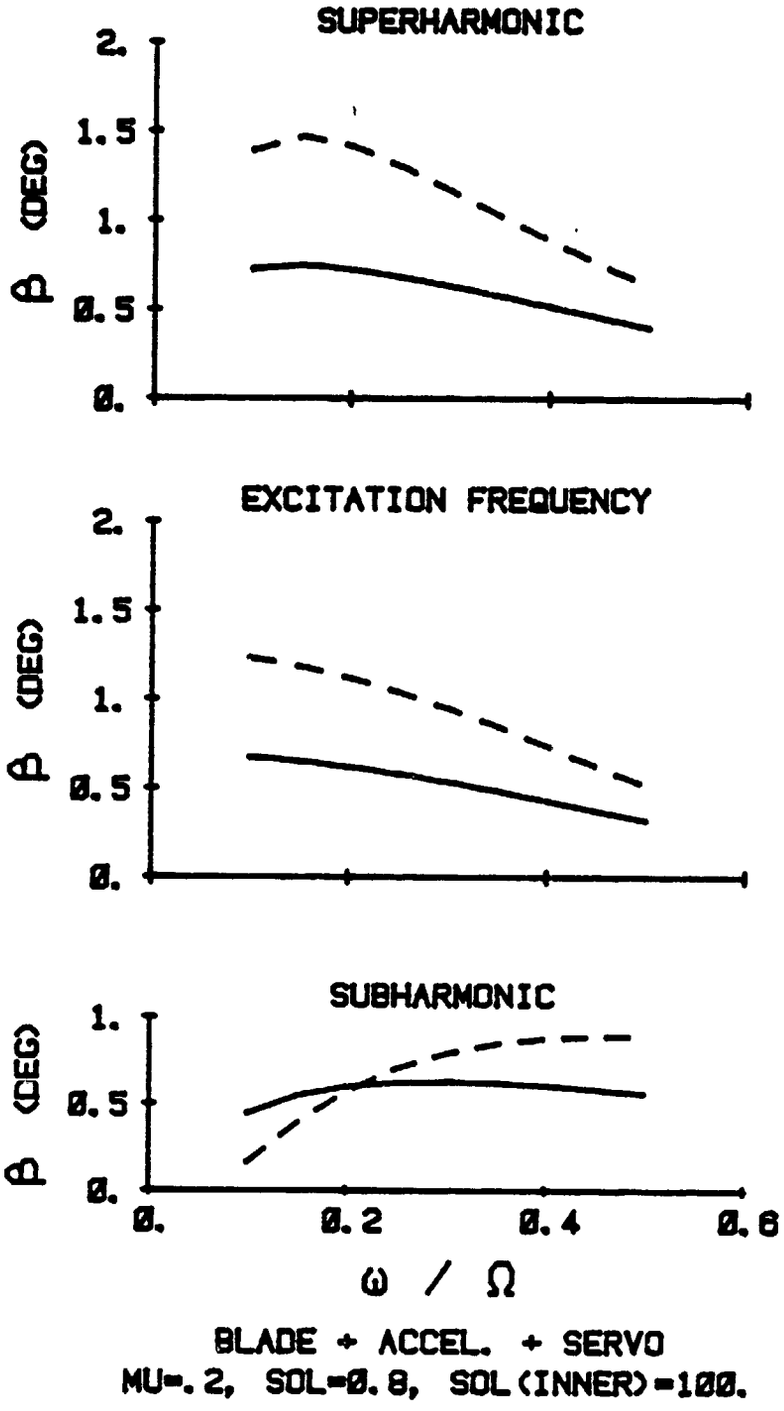

FIG. 20c (CONTINUED)

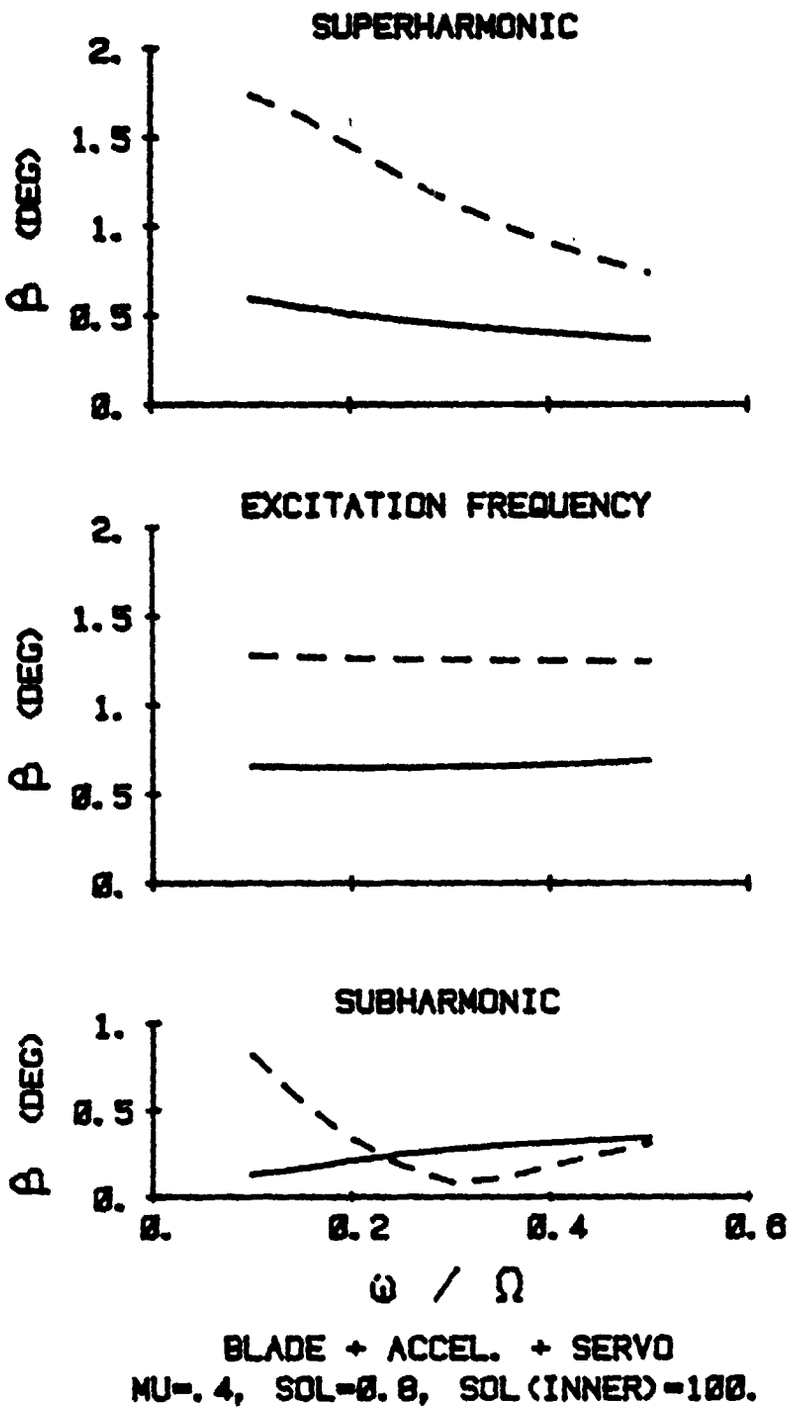

FIG. 20c (CONCLUDED)

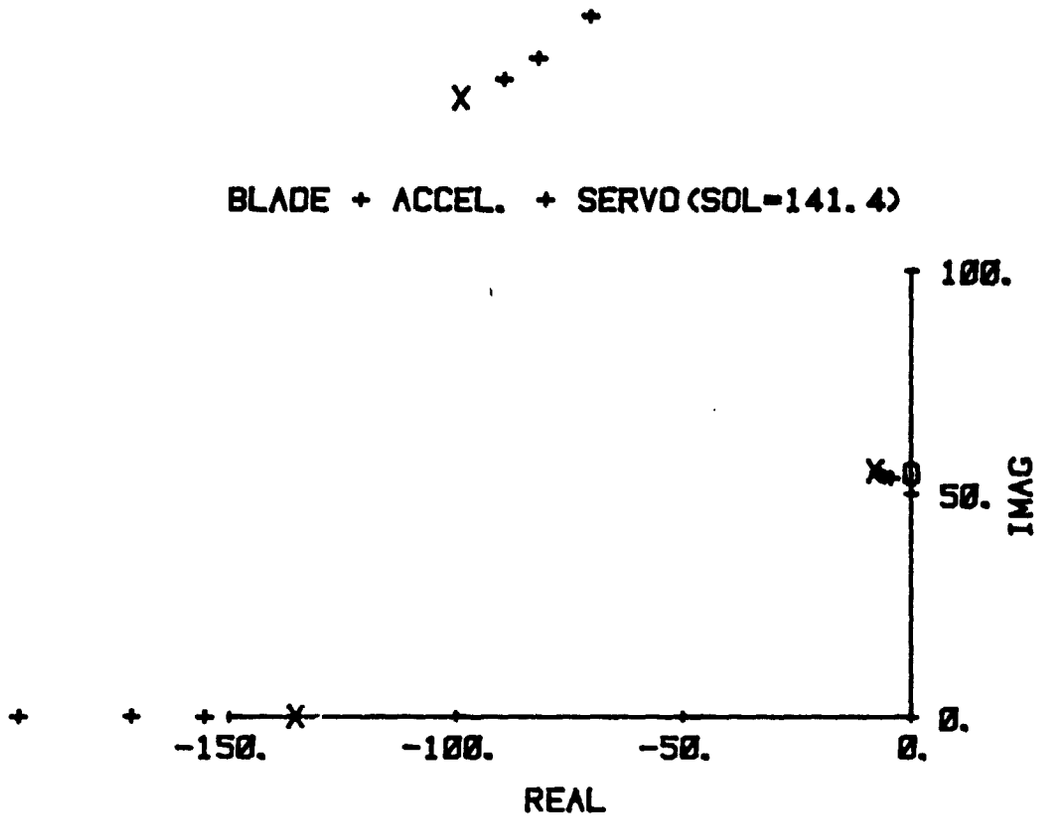

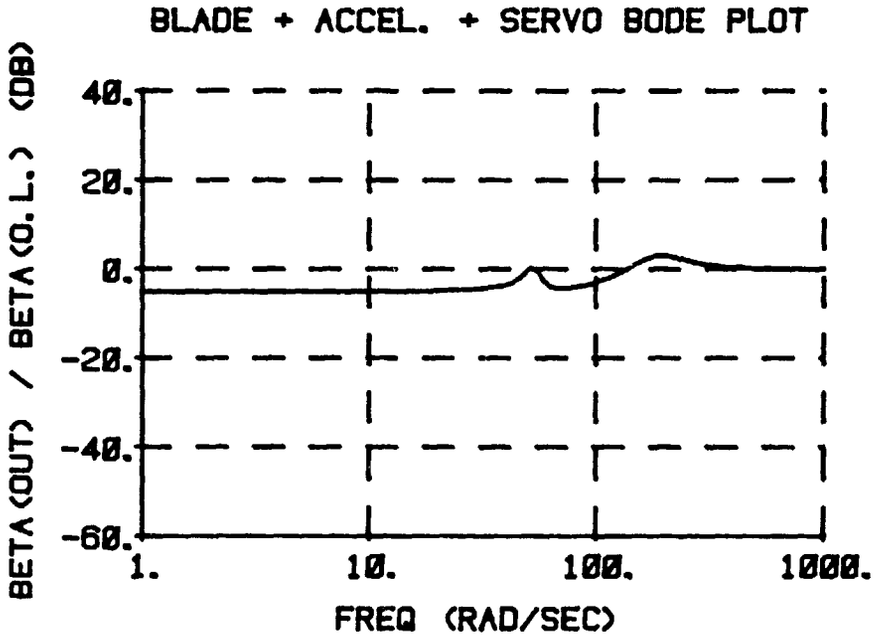

FIG. 21a, 21b BLADE, ACCELEROMETER, AND HIGH-GAIN-SERVO DESIGN

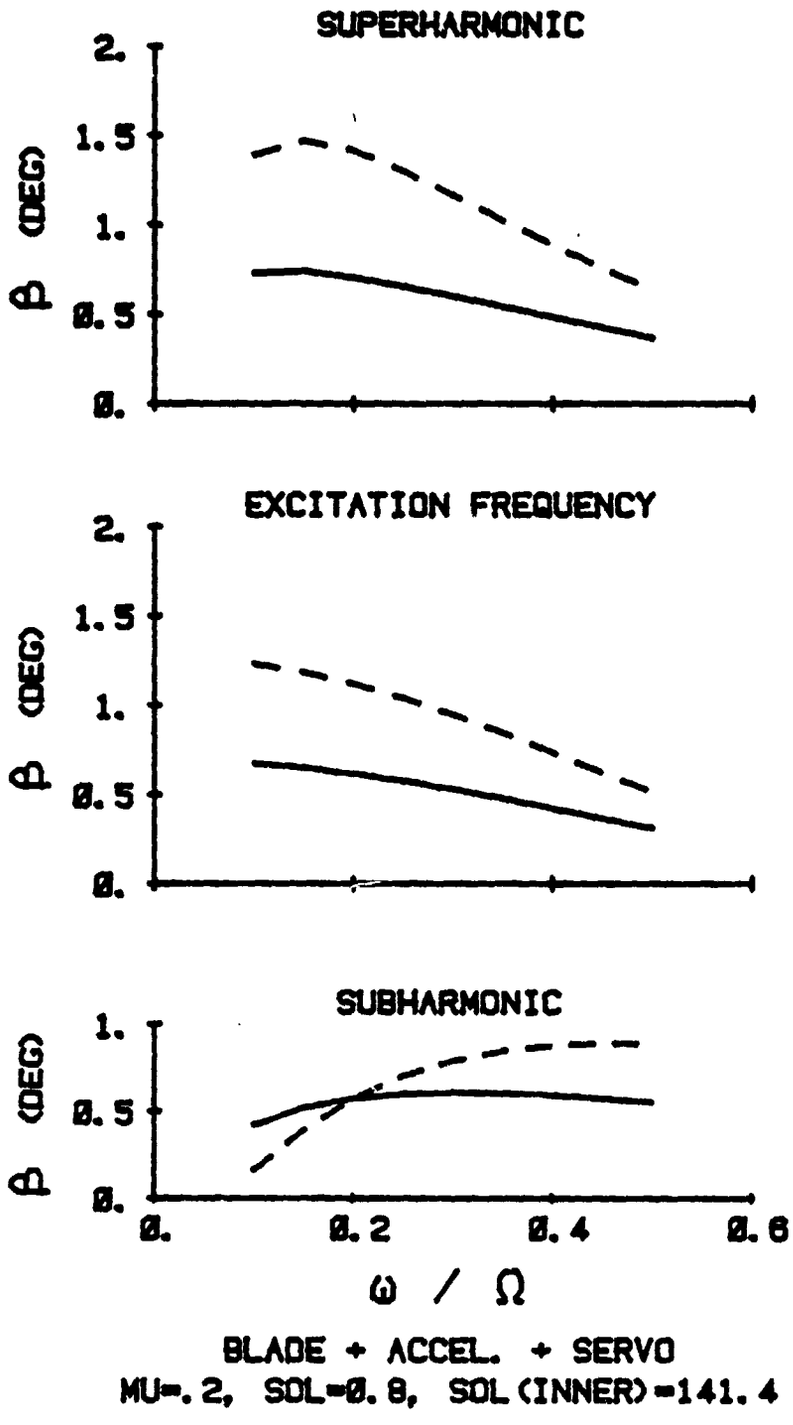

FIG. 21c (CONTINUED)

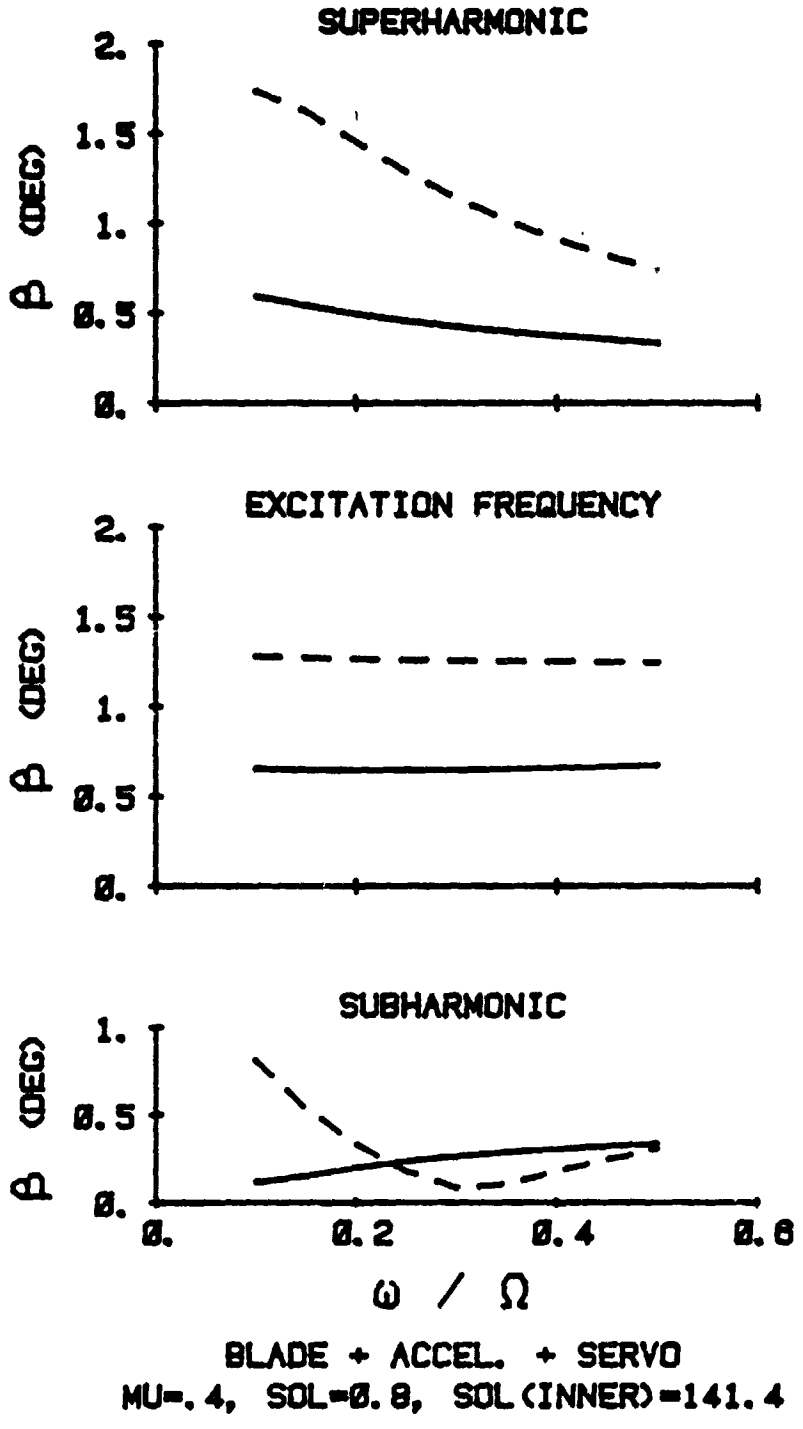

FIG. 21c (CONCLUDED)

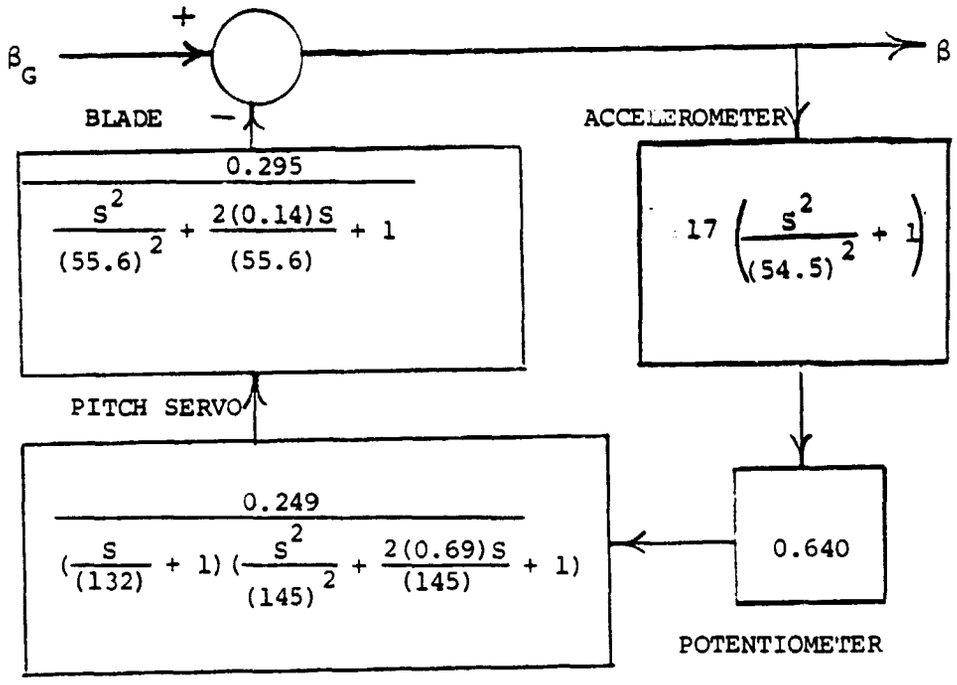

FIG. 22 GUST ALLEVIATION SYSTEM MATHEMATICAL BLOCK DIAGRAM

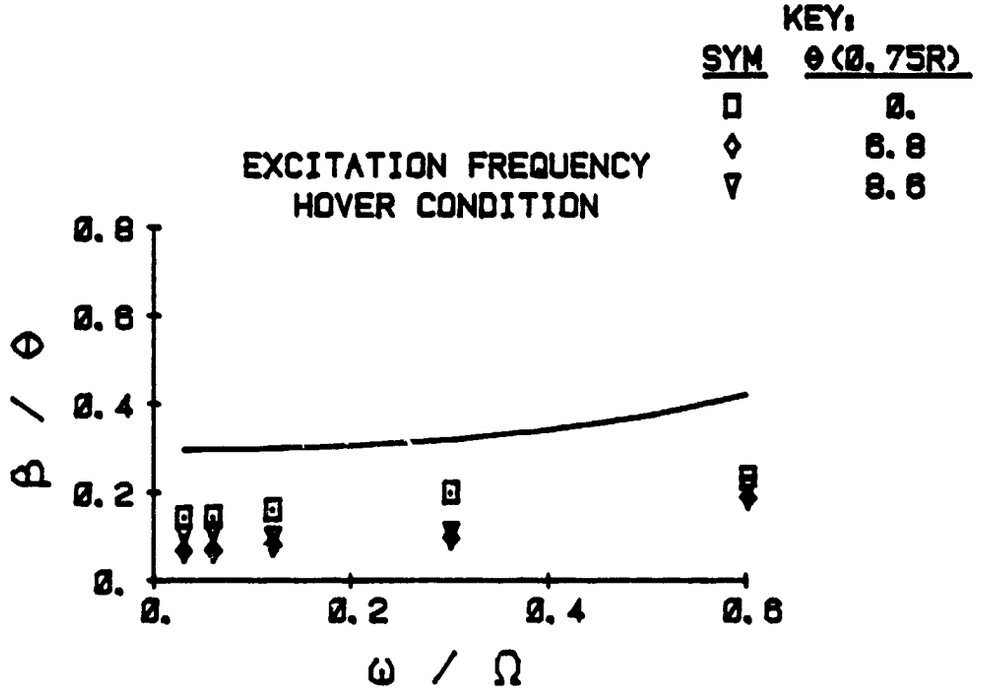

FLAP RESPONSE TO PITCH

FIG. 23a FLAP RESPONSE TO PITCH EXCITATION

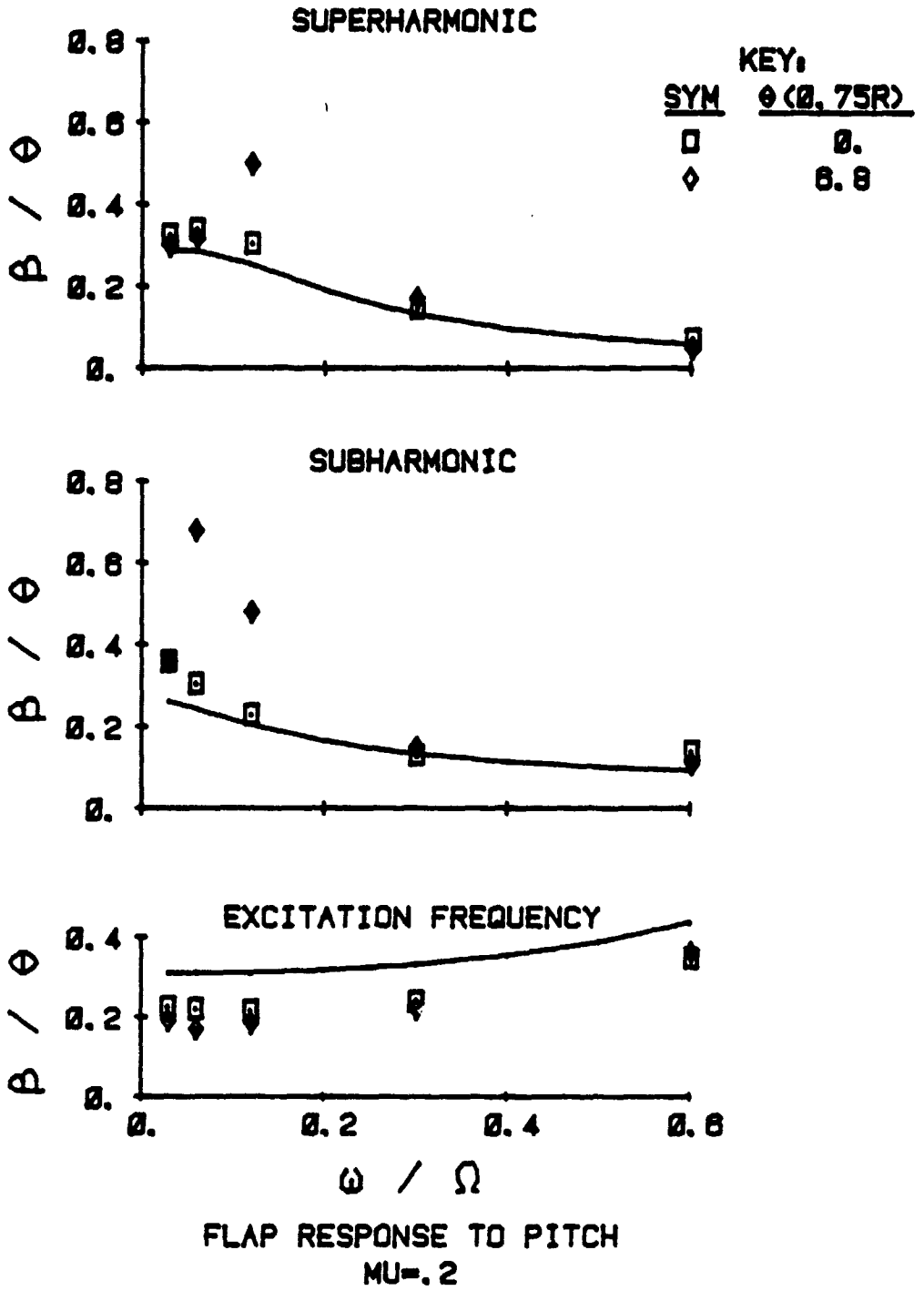

FIG. 23b (CONTINUED)

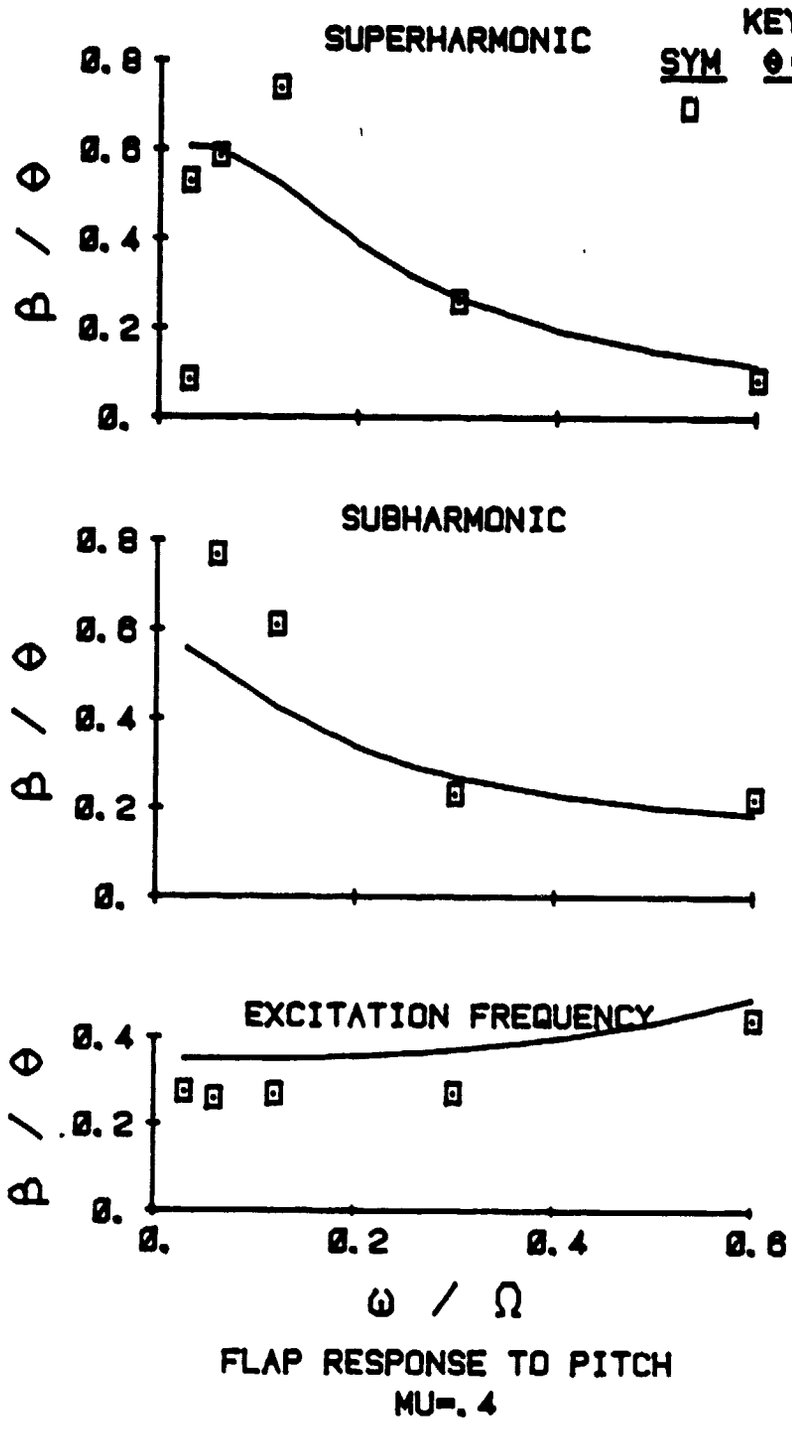

FLAP RESPONSE TO PITCH
MU=.4

FIG. 23c (CONCLUDED)

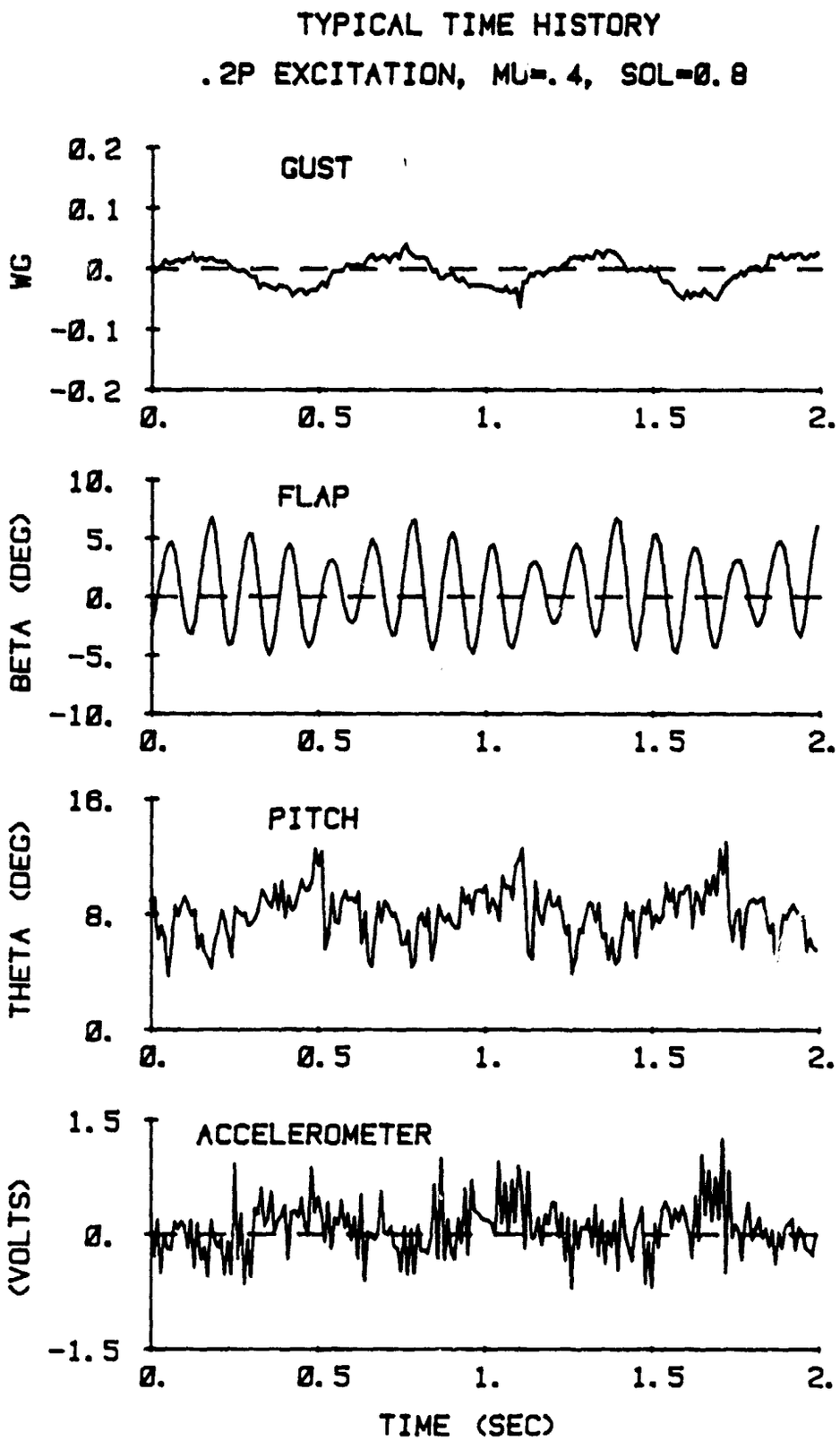

FIG. 24 TYPICAL I.B.C. GUST SYSTEM TIME HISTORY

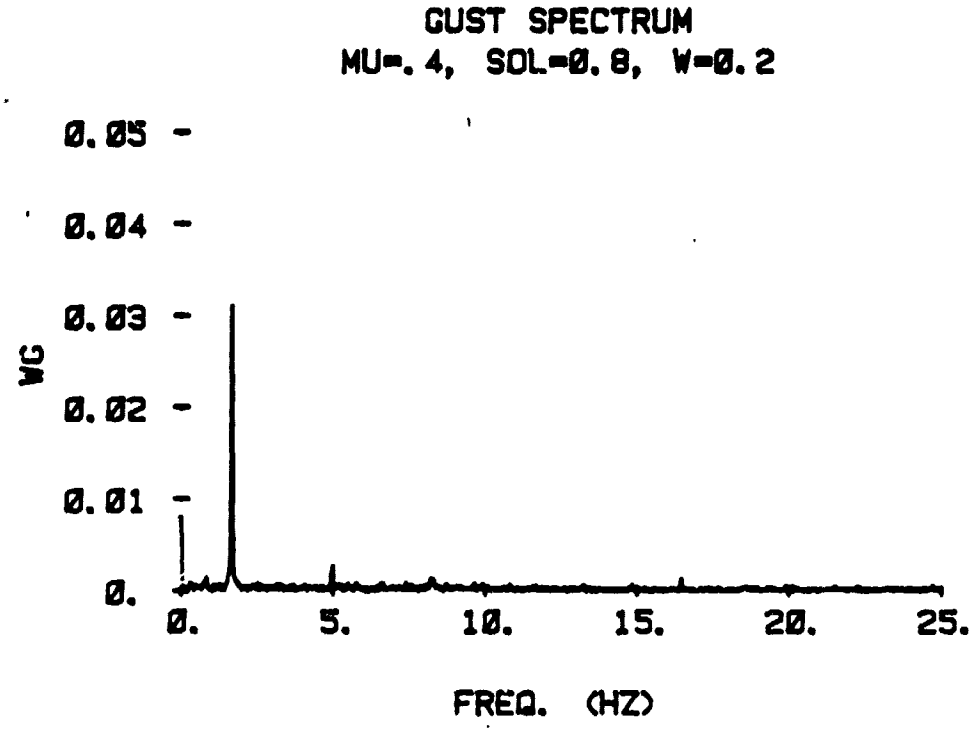

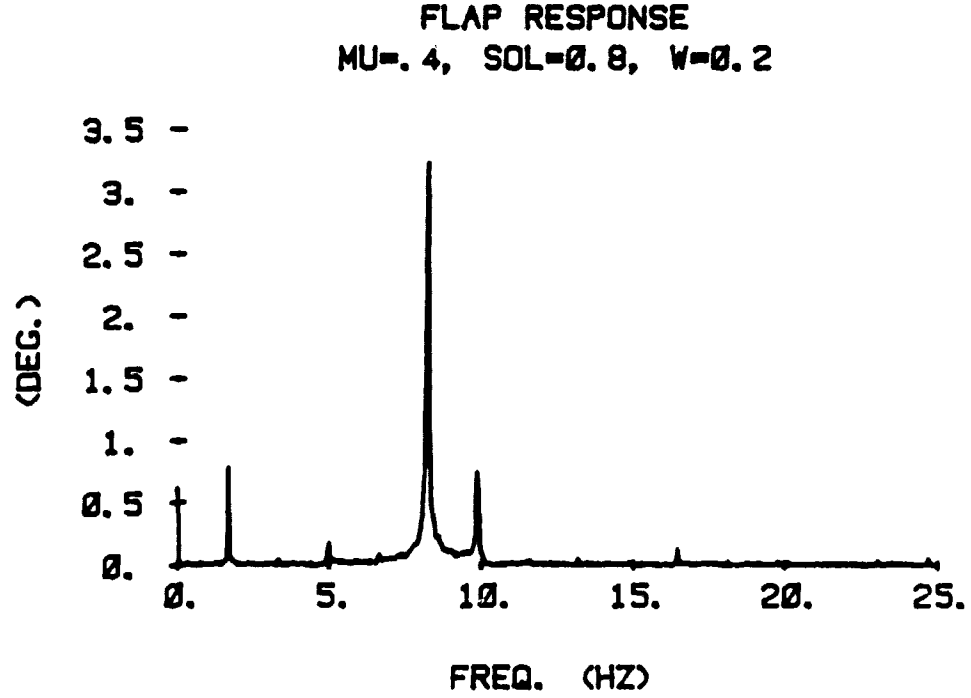

FIG. 25a SPECTRAL DECOMPOSITION OF GUST, FLAP, PITCH AND ACCELEROMETER DATA

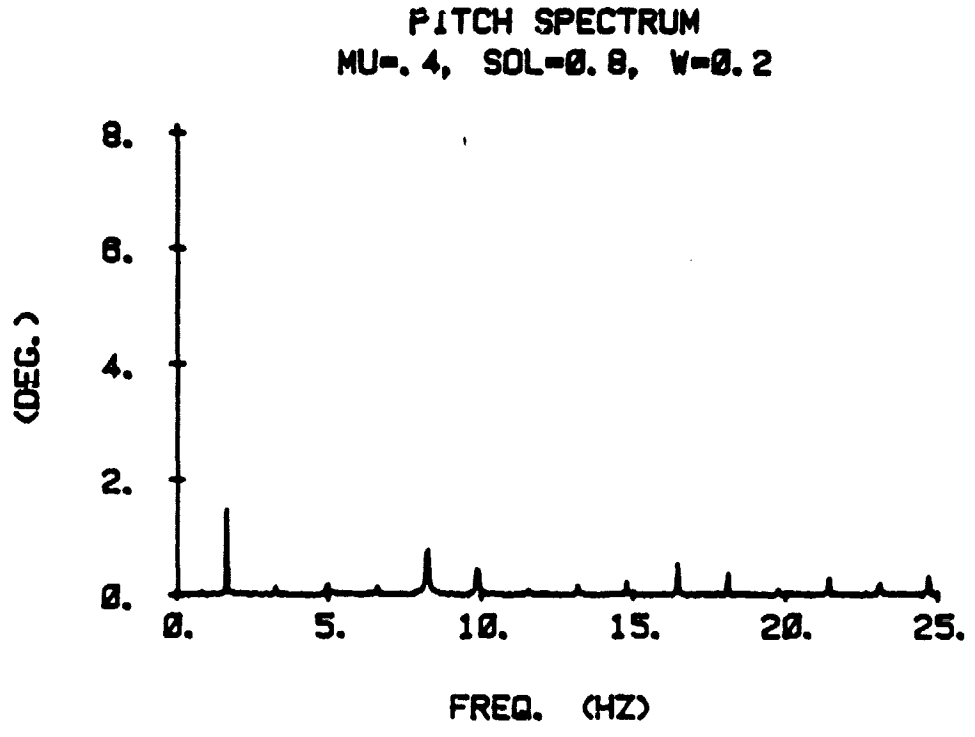

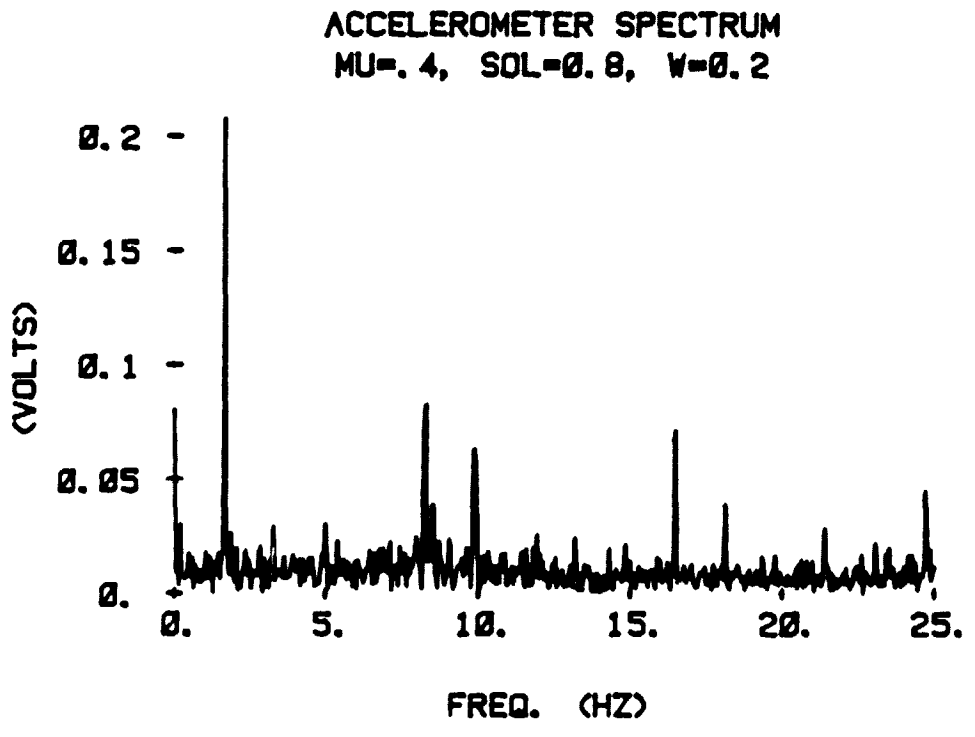

FIG. 25b (CONCLUDED)

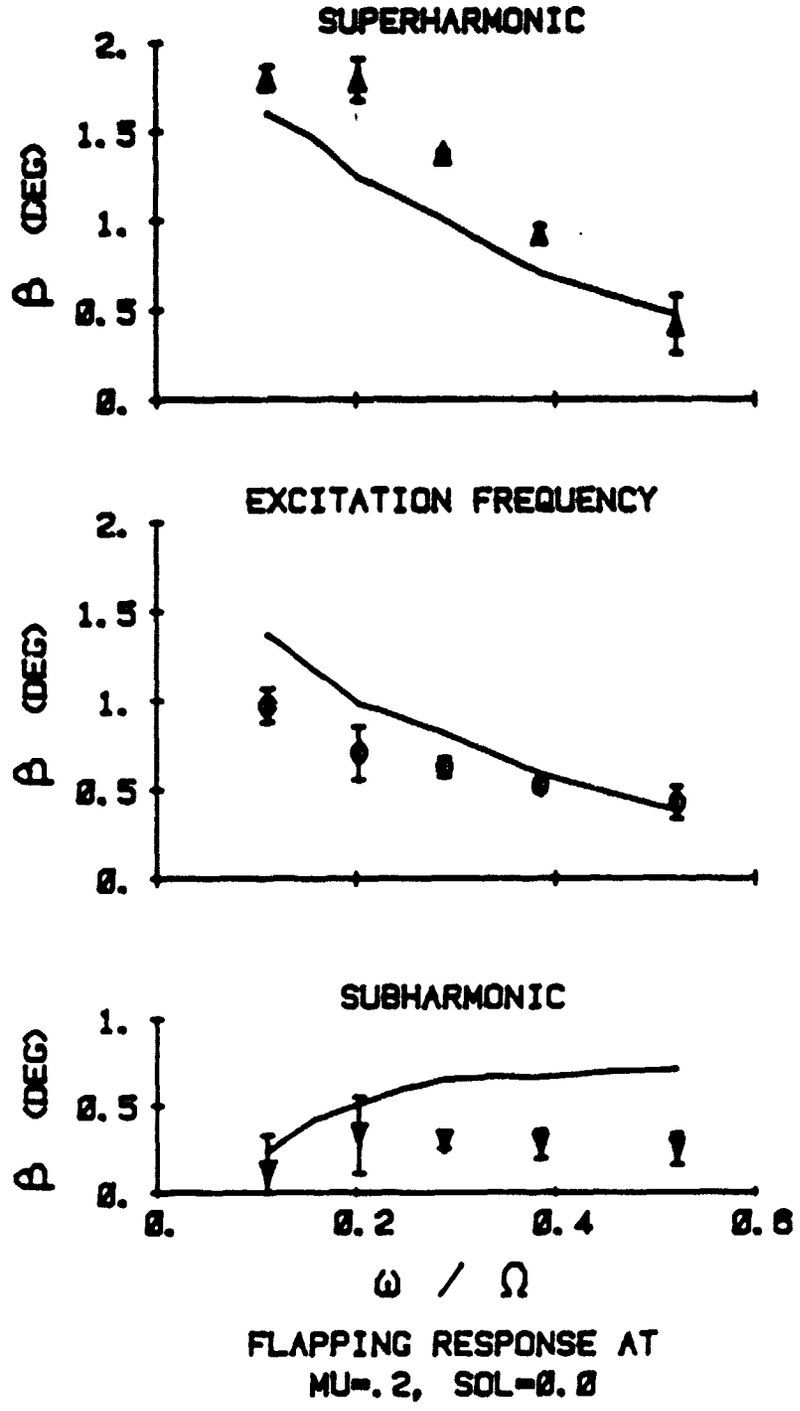

FIG. 26a FLAPPING RESPONSE TO GUST EXCITATION

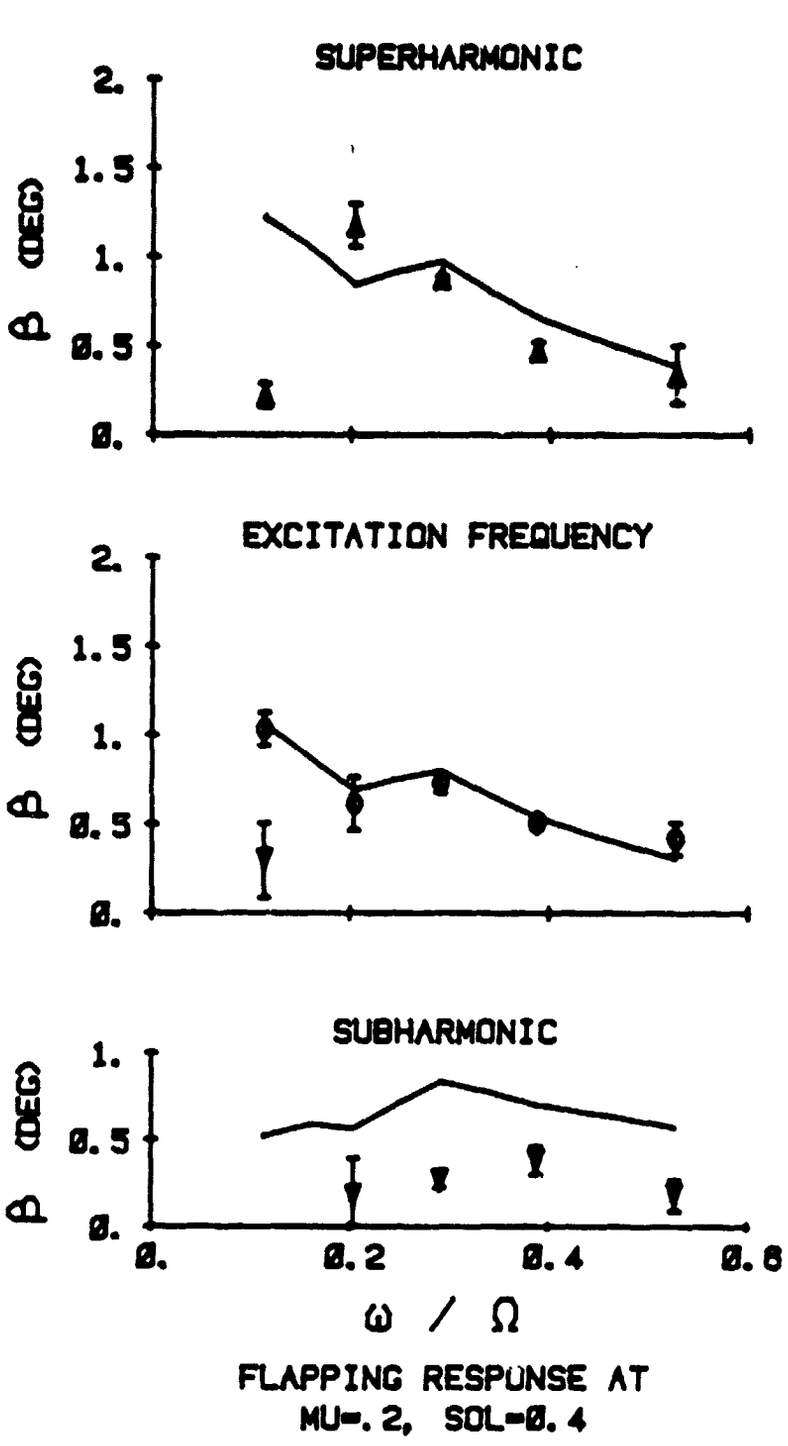

FIG. 26b (CONTINUED)

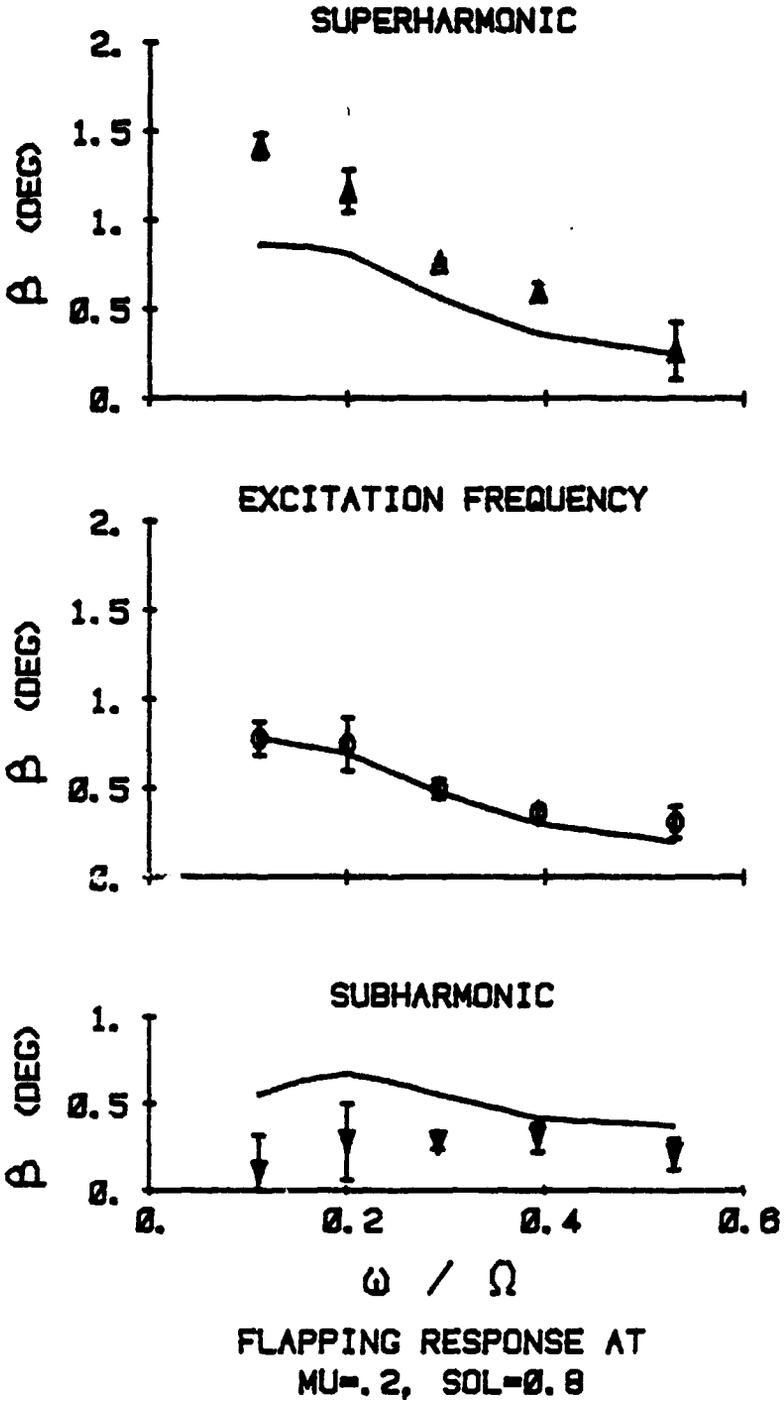

FIG. 26c (CONTINUED)

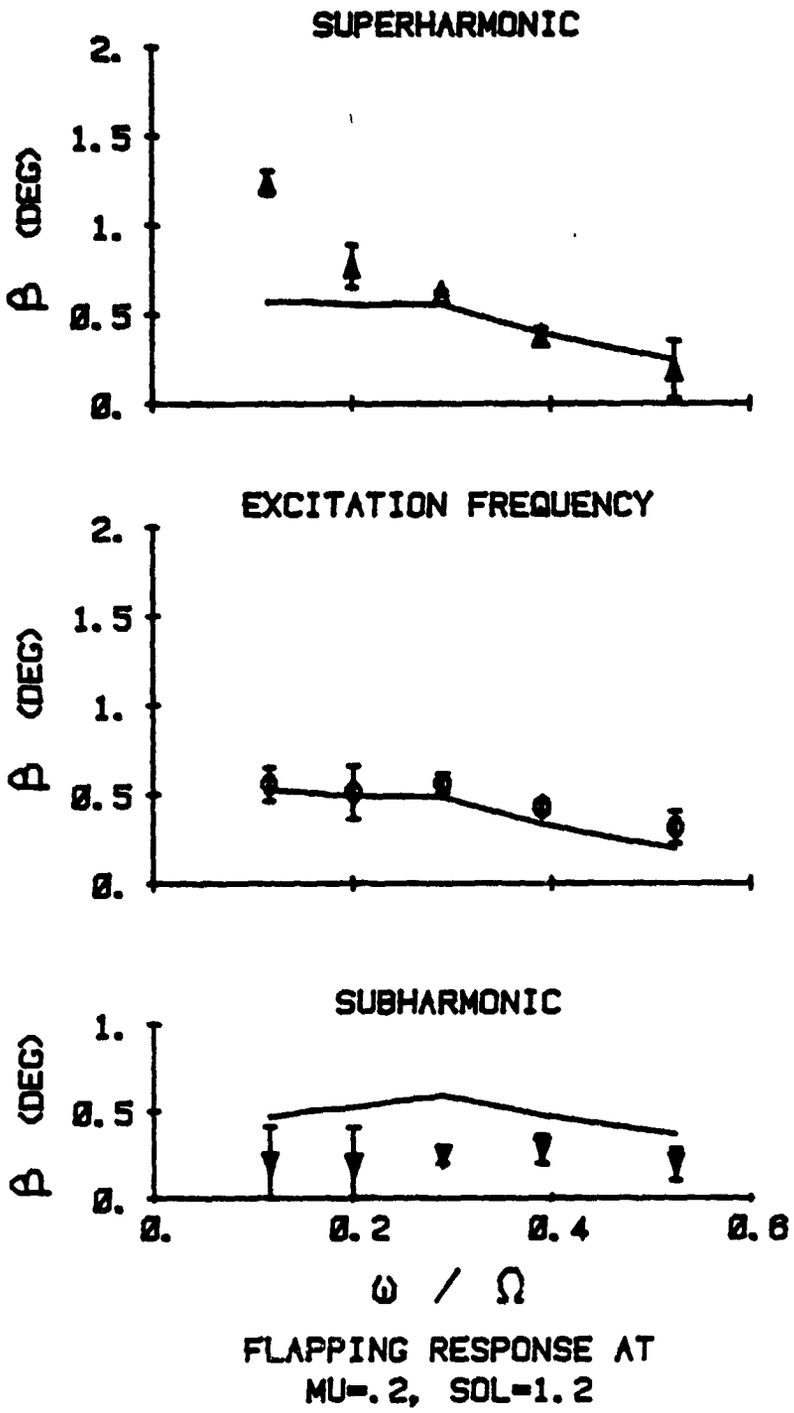

FLAPPING RESPONSE AT
MU=.2, SOL=1.2

FIG. 26d (CONTINUED)

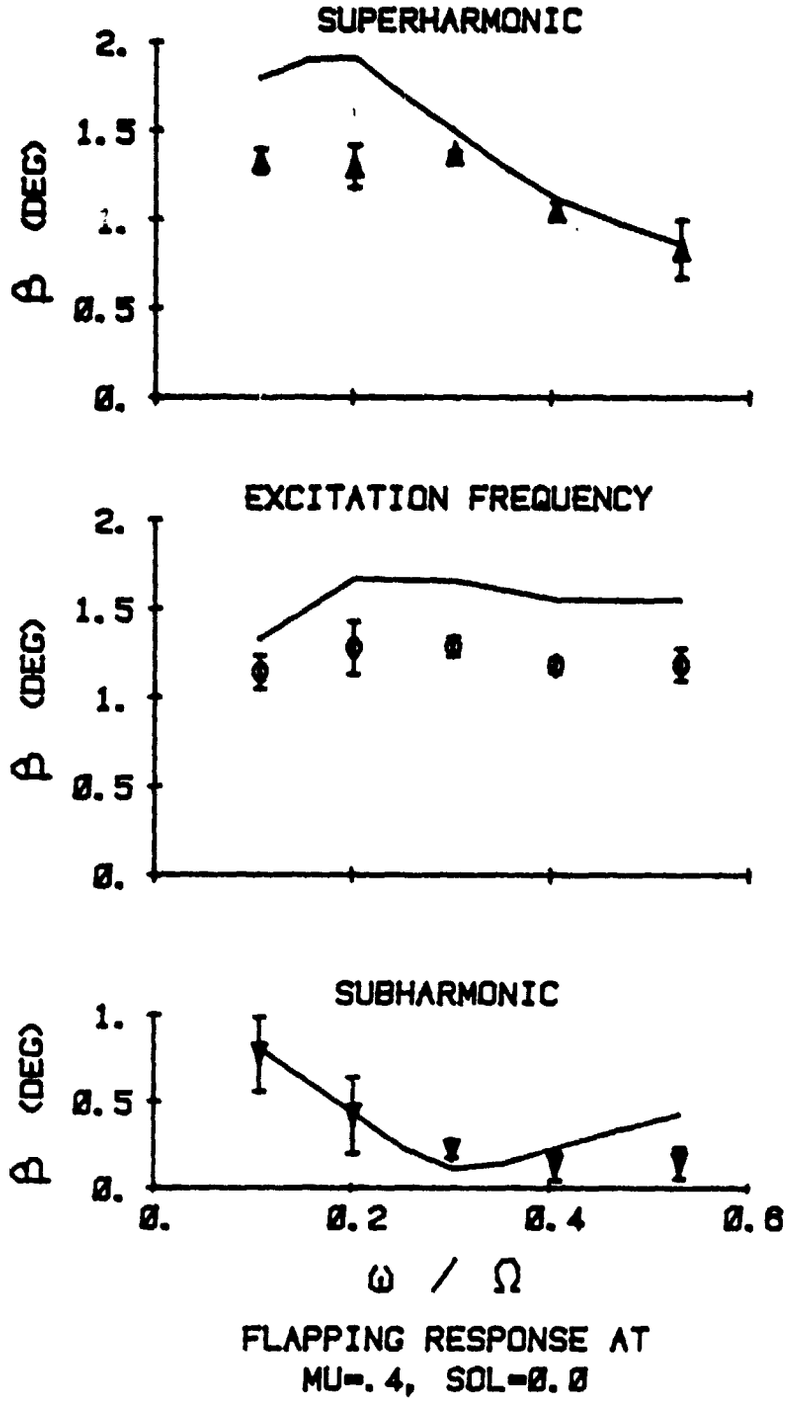

FIG. 26e (CONTINUED)

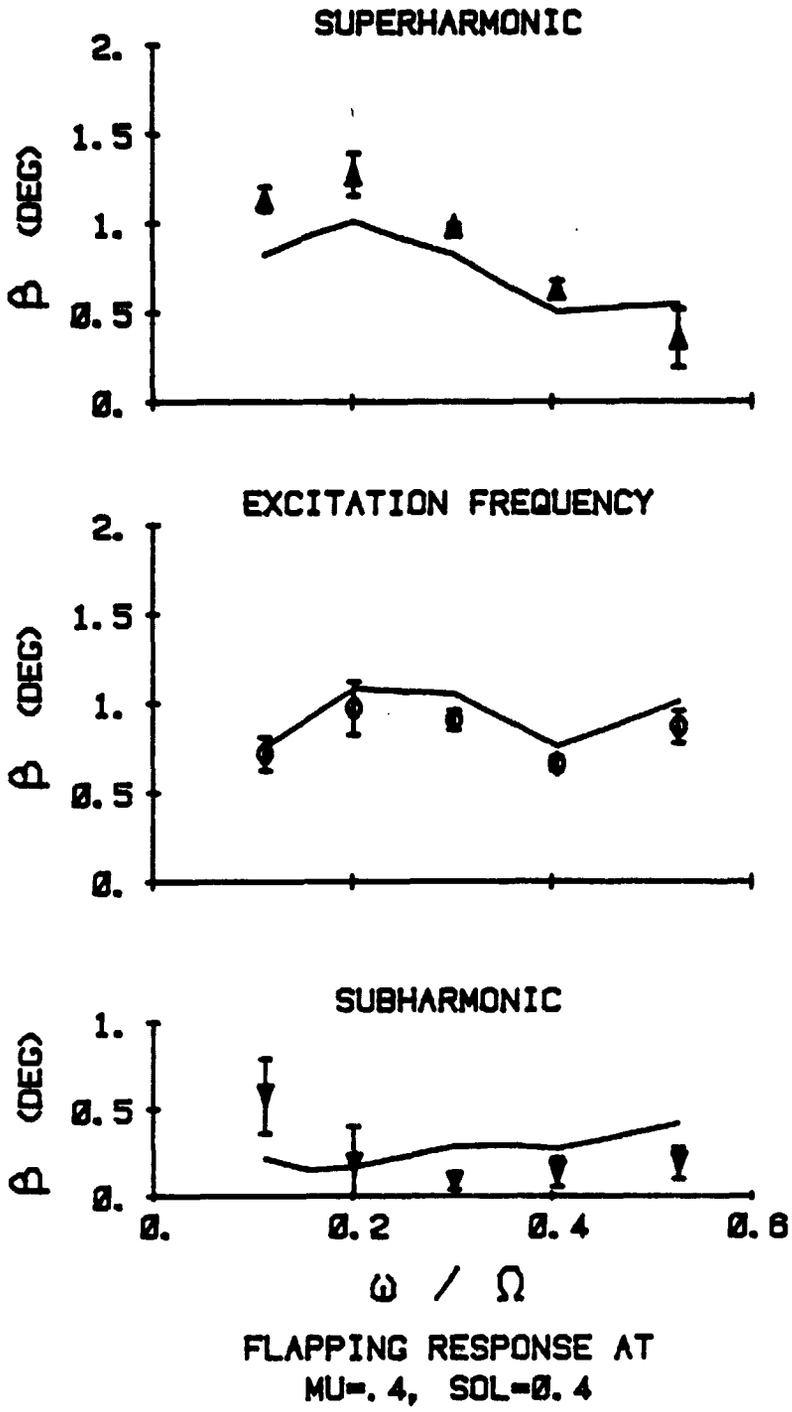

FIG. 26f (CONTINUED)

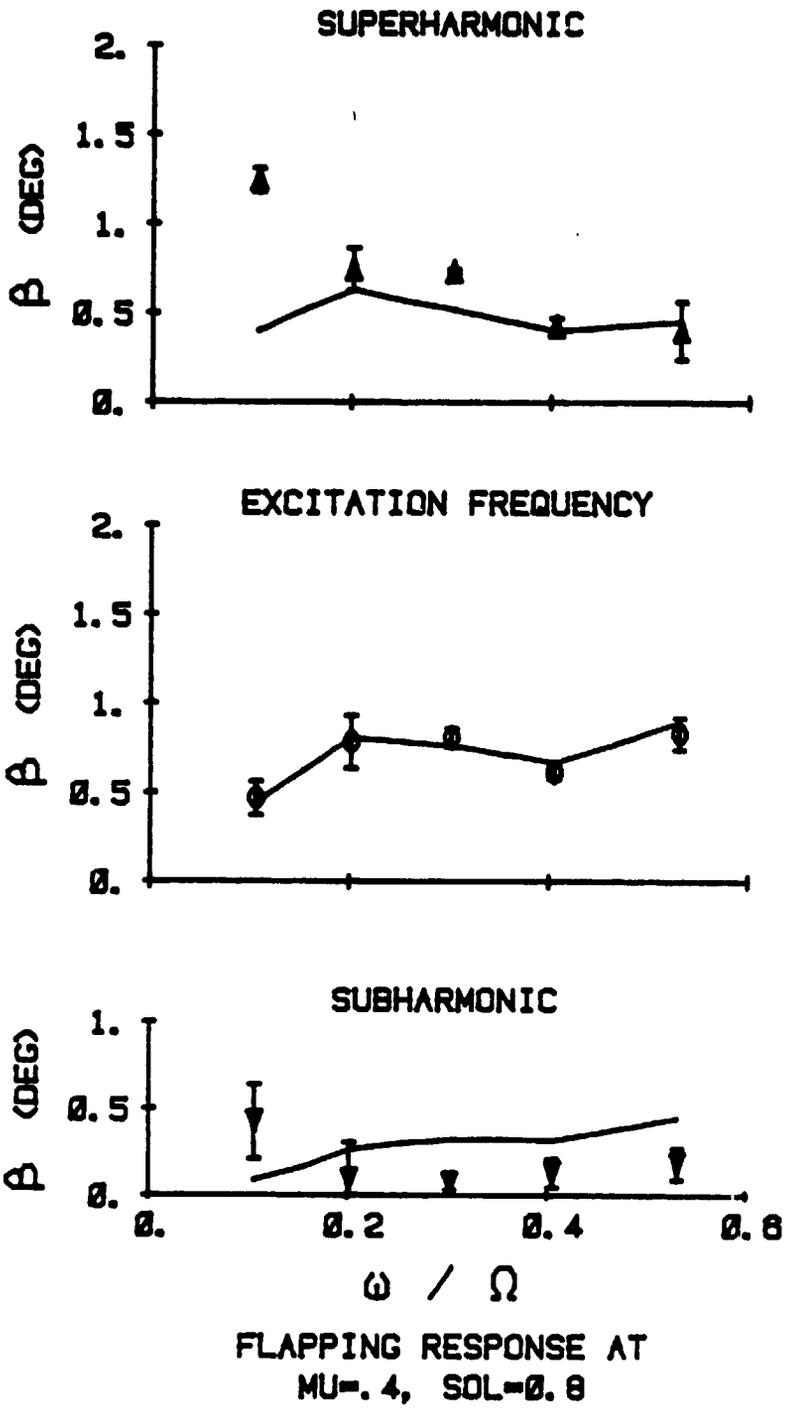

FIG. 26g (CONTINUED)

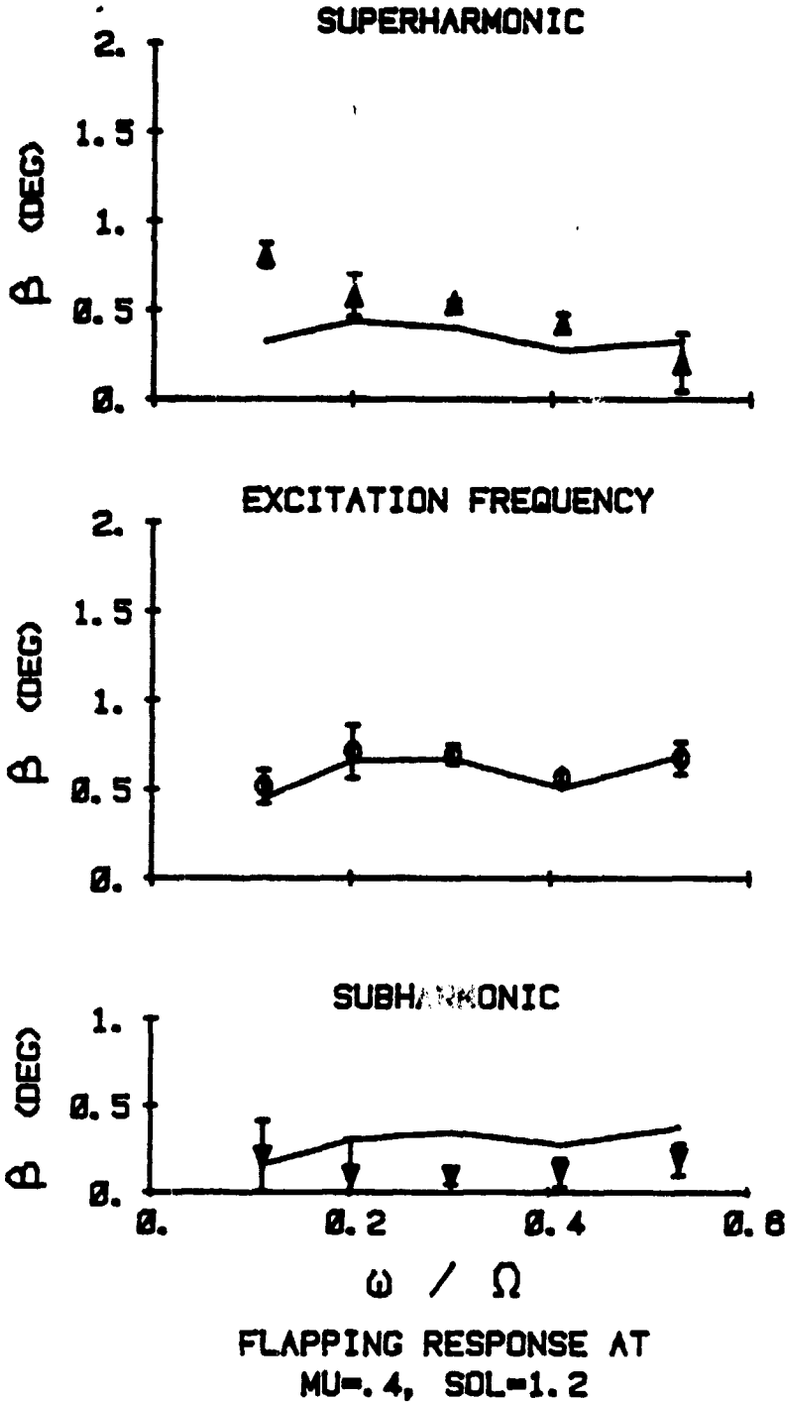

FIG. 26h (CONCLUDED)

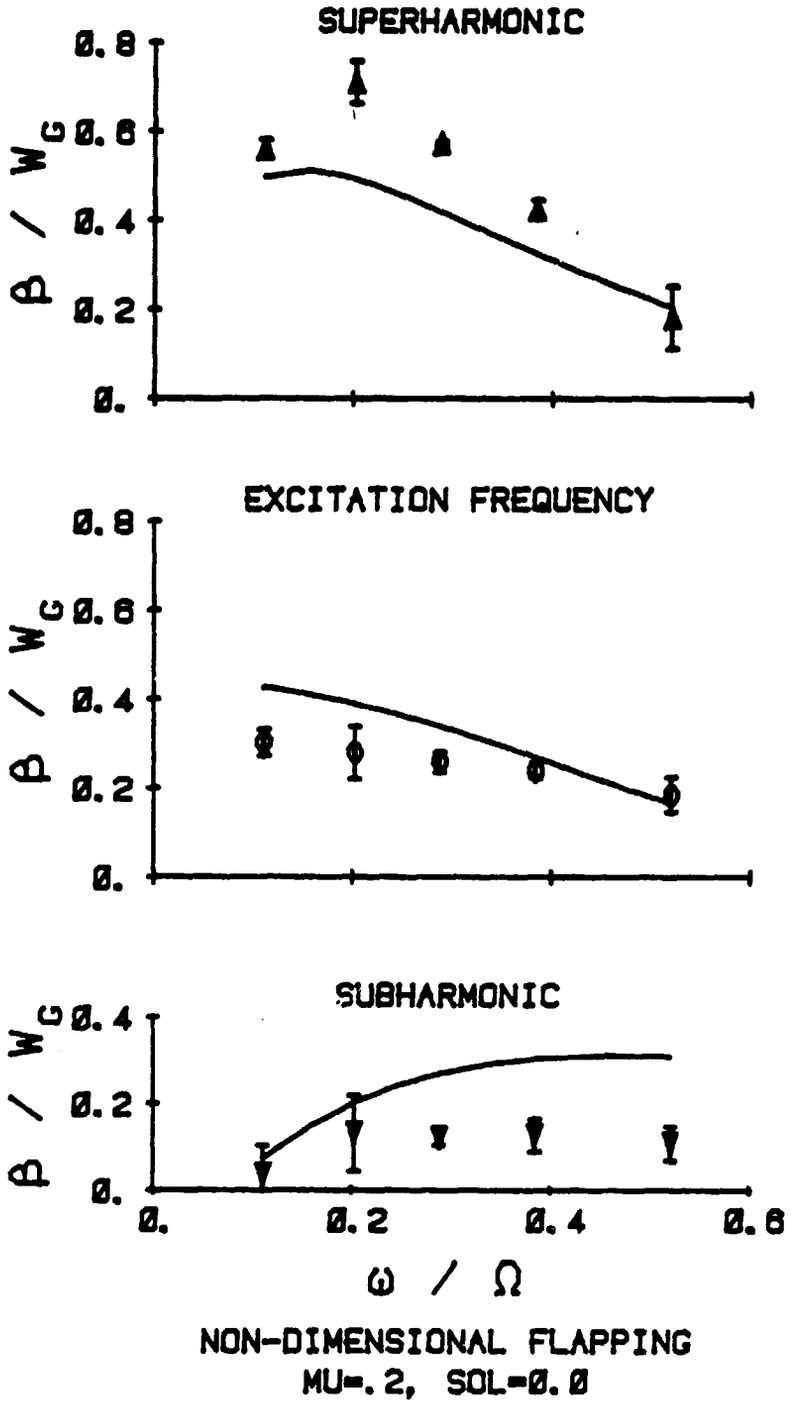

FIG. 27a NON-DIMENSIONALIZED FLAP RESPONSE TO GUST

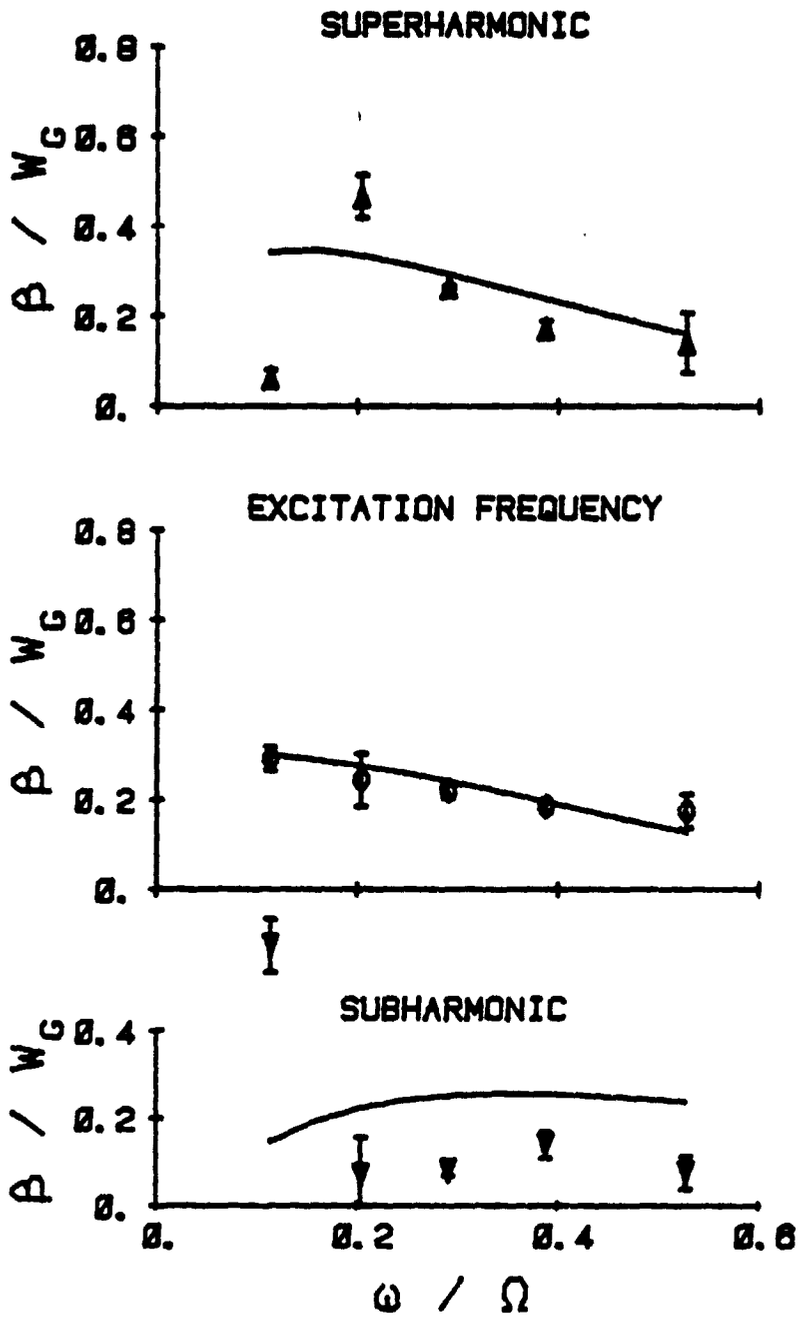

FIG. 27b (CONTINUED)

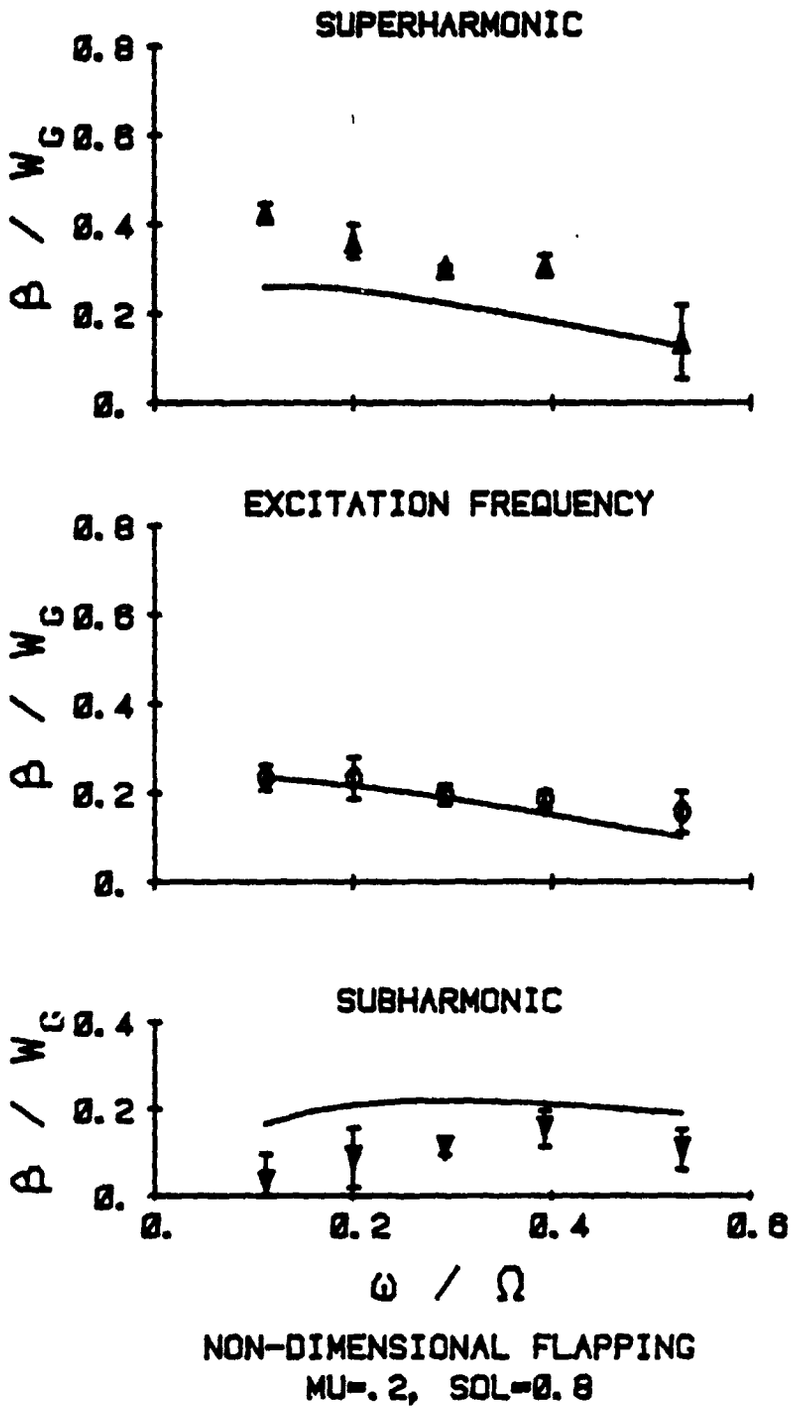

FIG. 27c (CONTINUED)

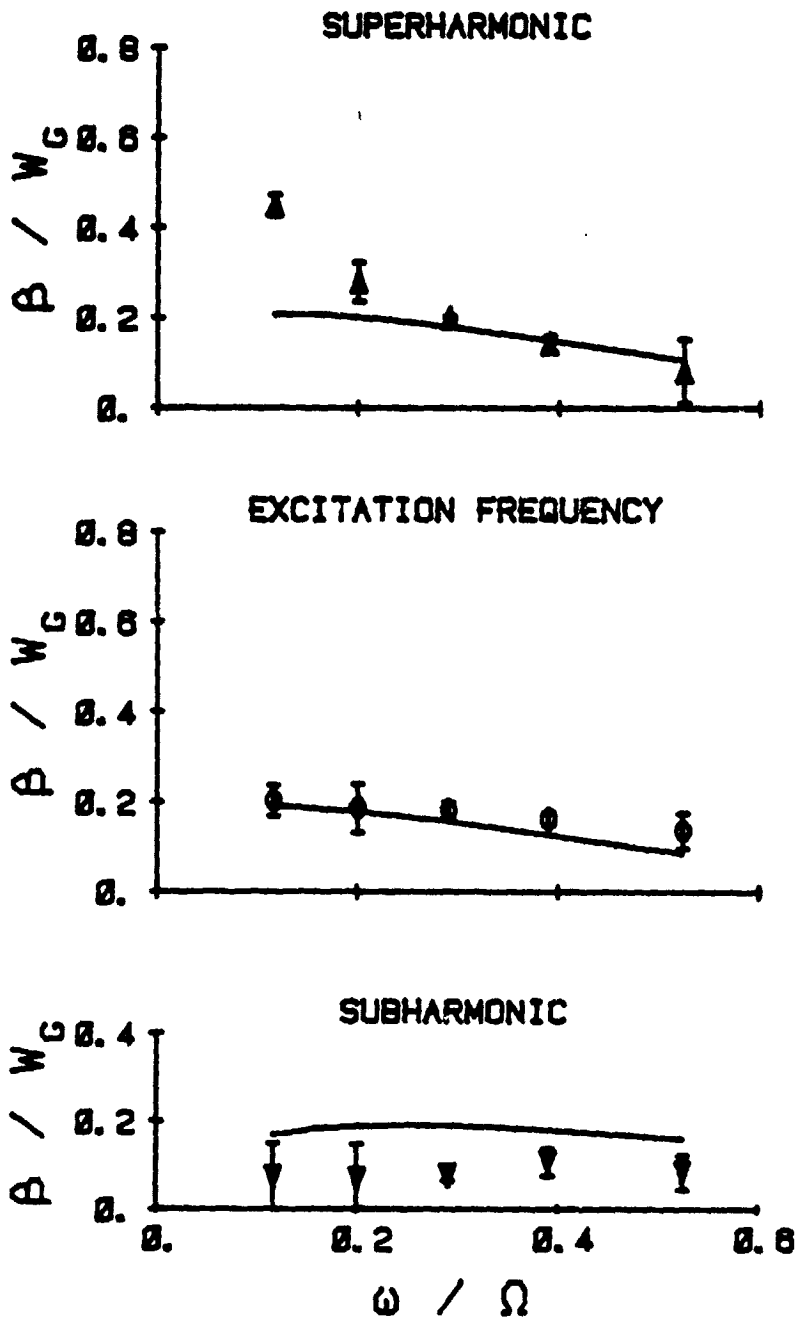

FIG. 27d (CONTINUED)

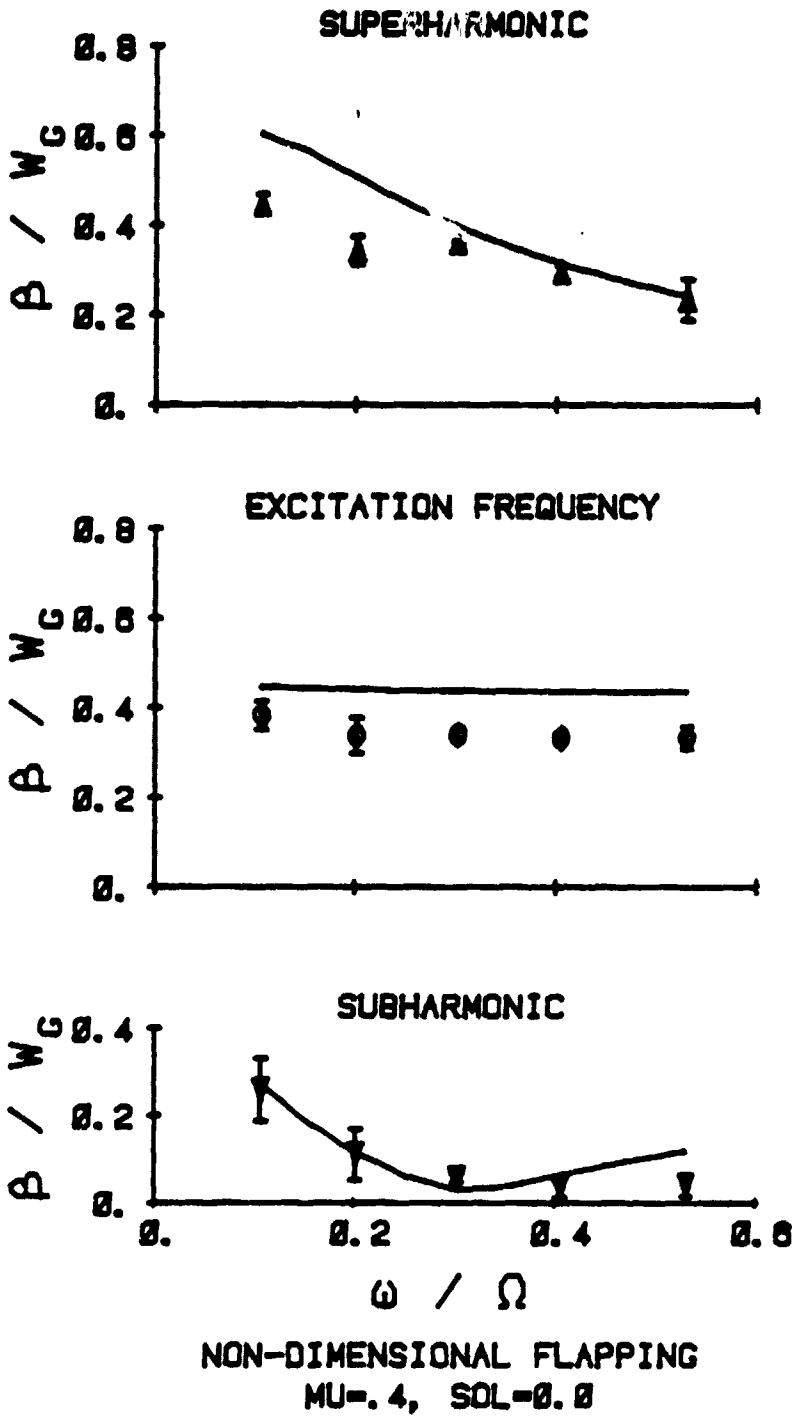

FIG. 27e (CONTINUED)

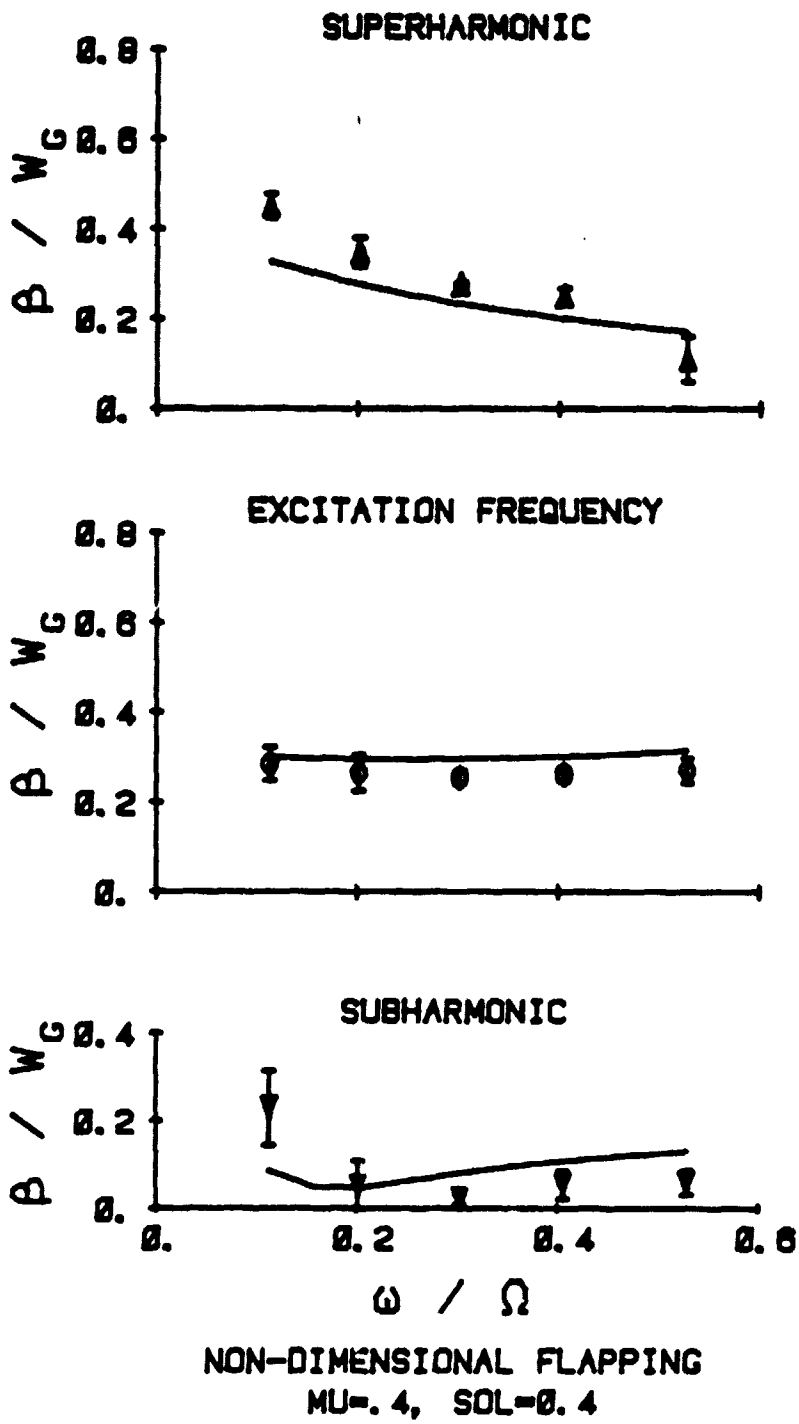

FIG. 27f (CONTINUED)

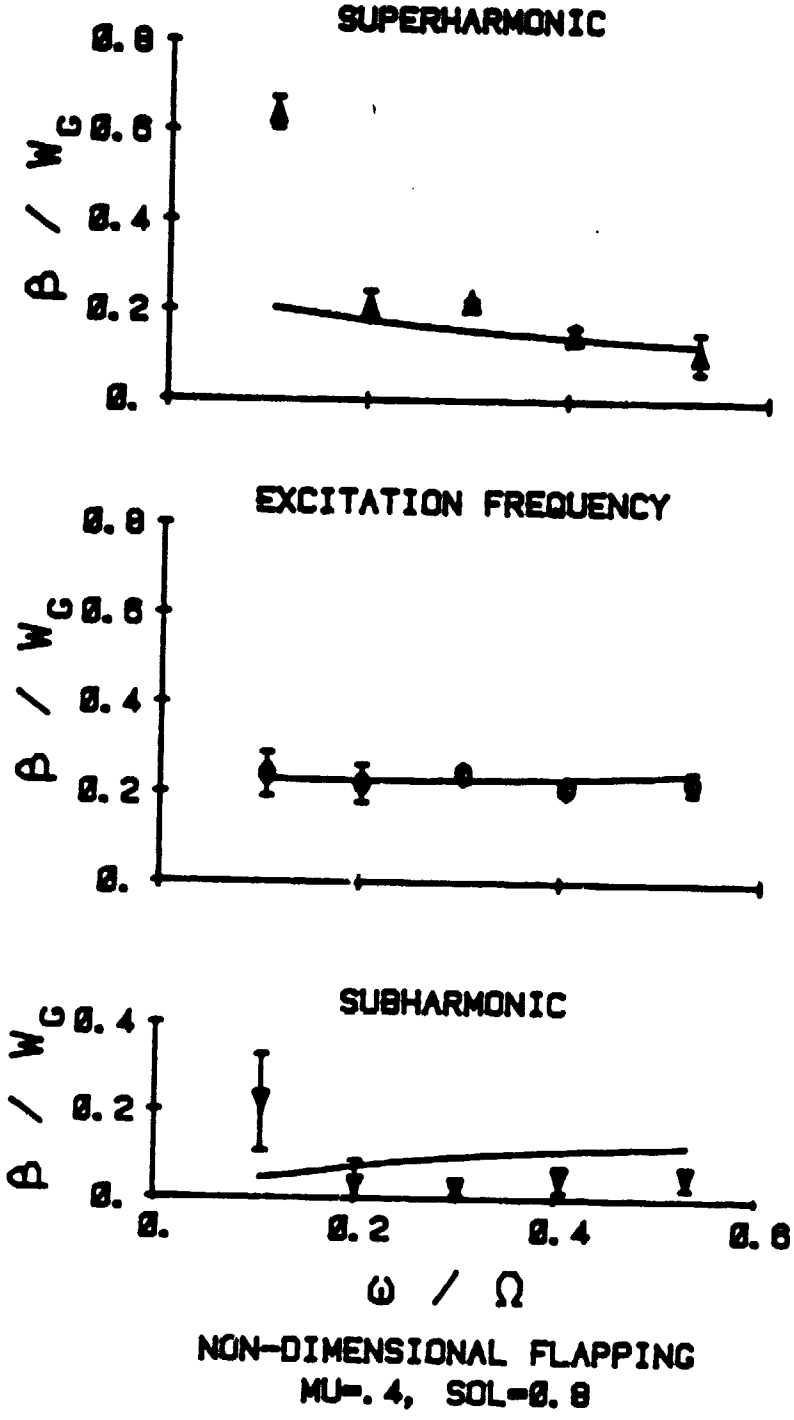

FIG. 27g (CONTINUED)

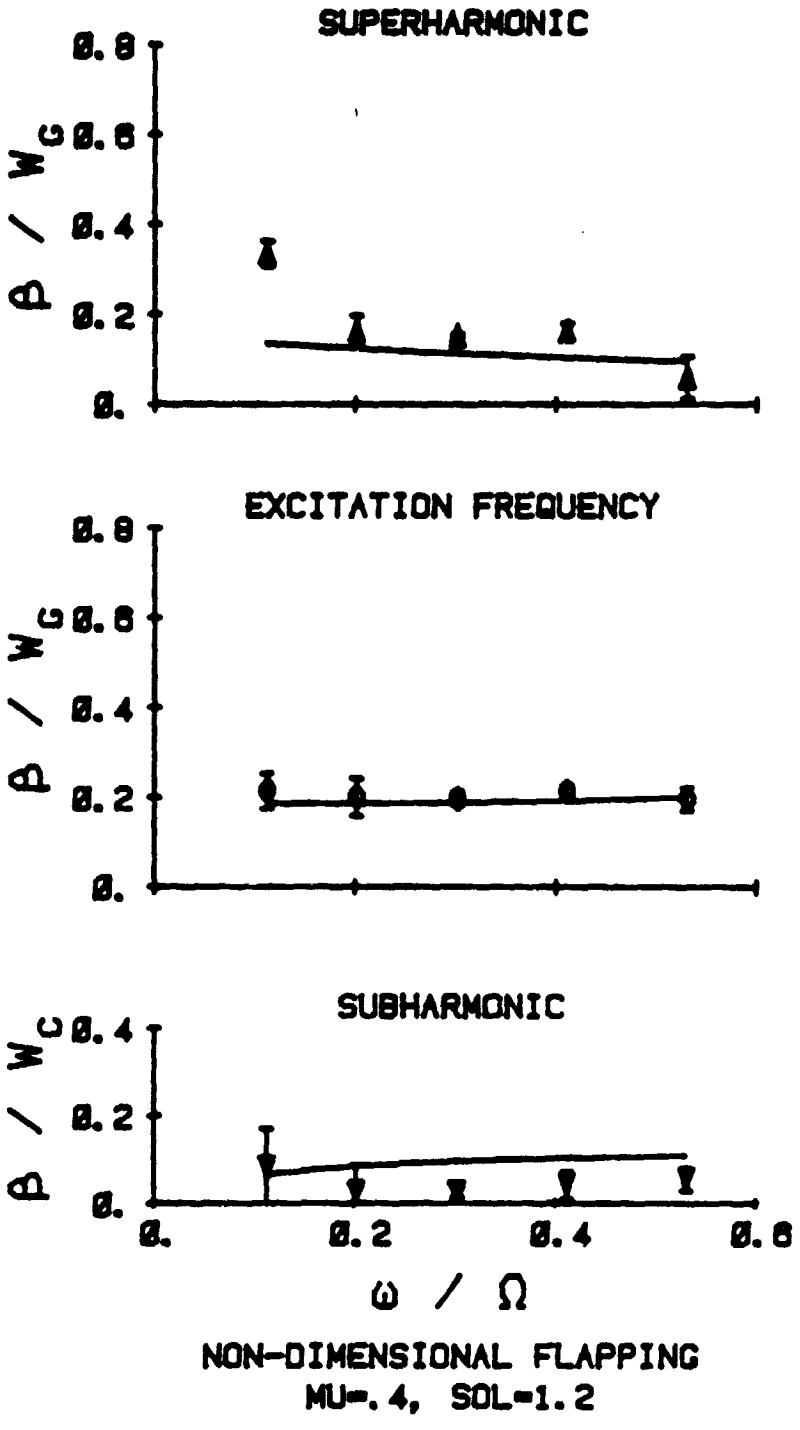

FIG. 27h (CONCLUDED)

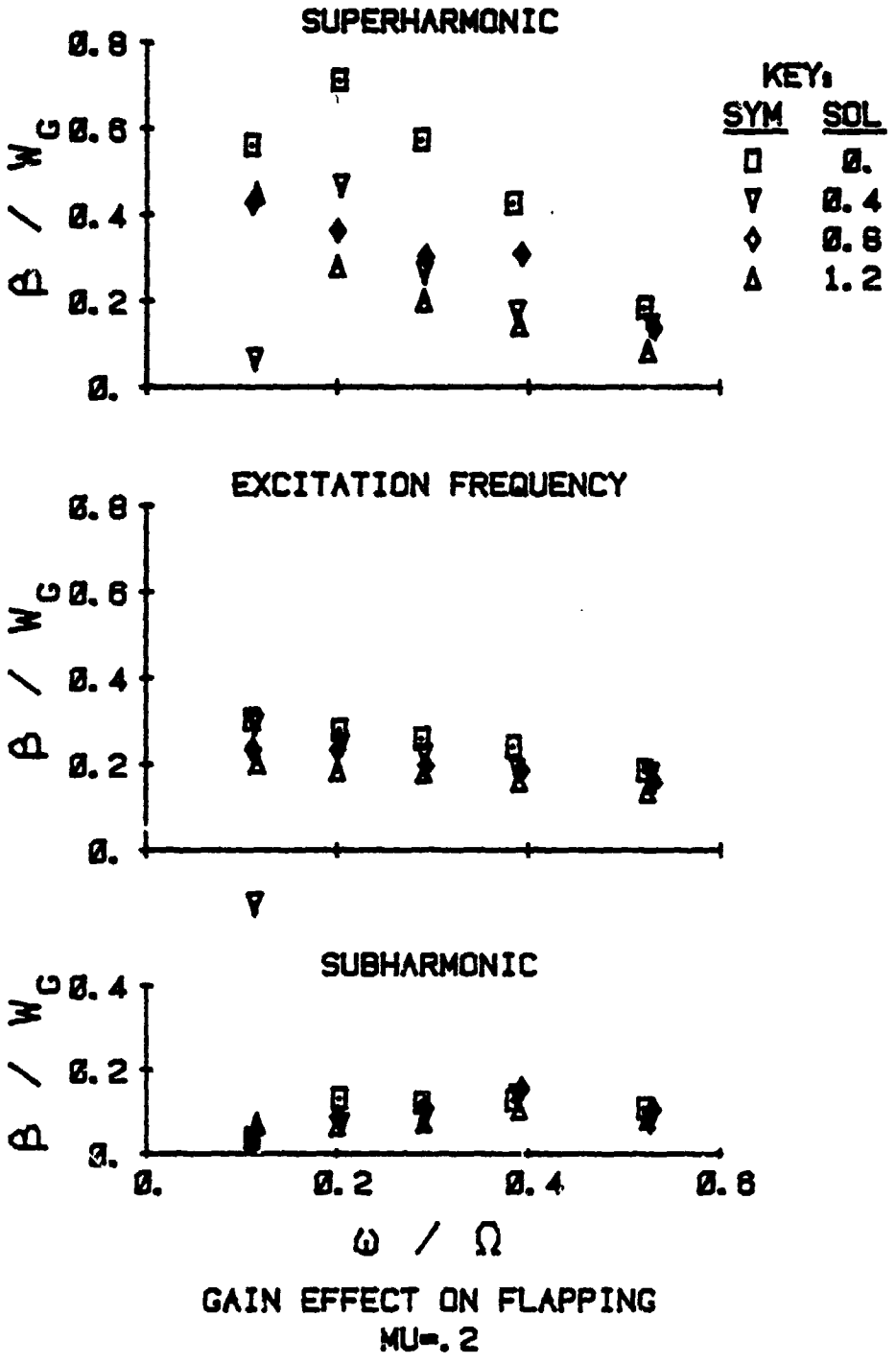

FIG. 28a EFFECT OF FEEDBACK GAIN ON FLAP RESPONSE TO GUST

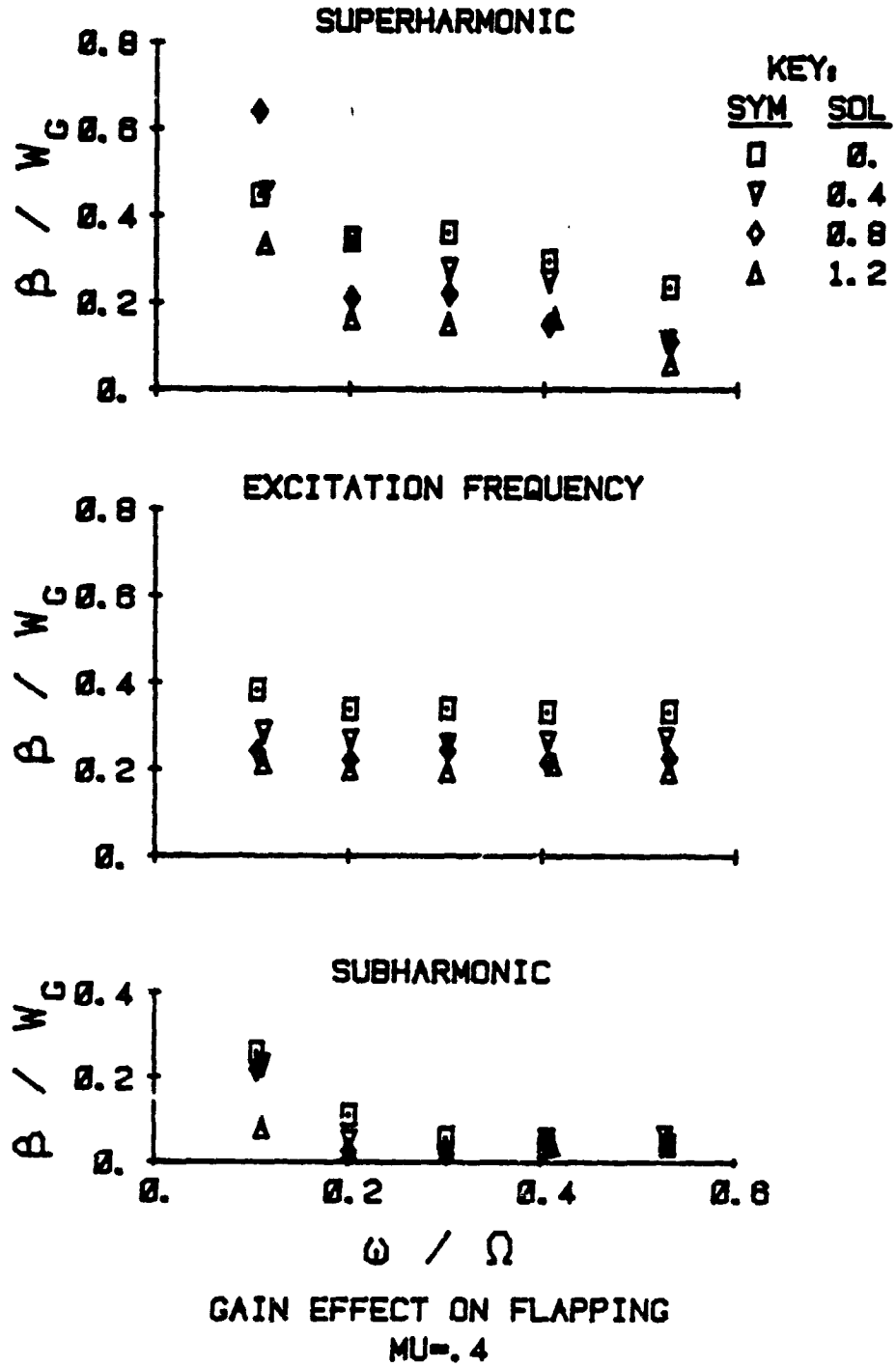

FIG. 28b (CONCLUDED)

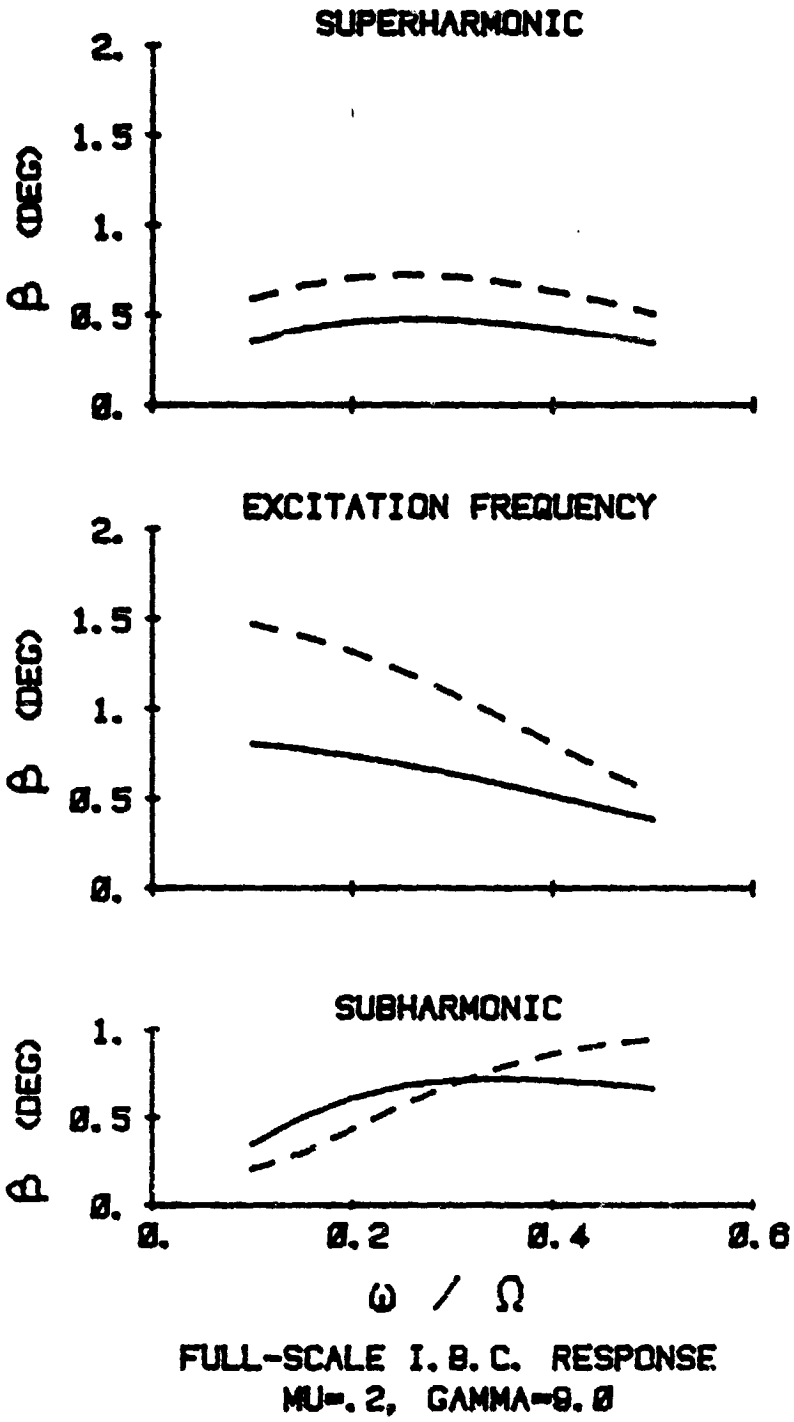

FIG. 29a THEORETICAL FLAP RESPONSE FOR INCREASED LOCK NUMBER

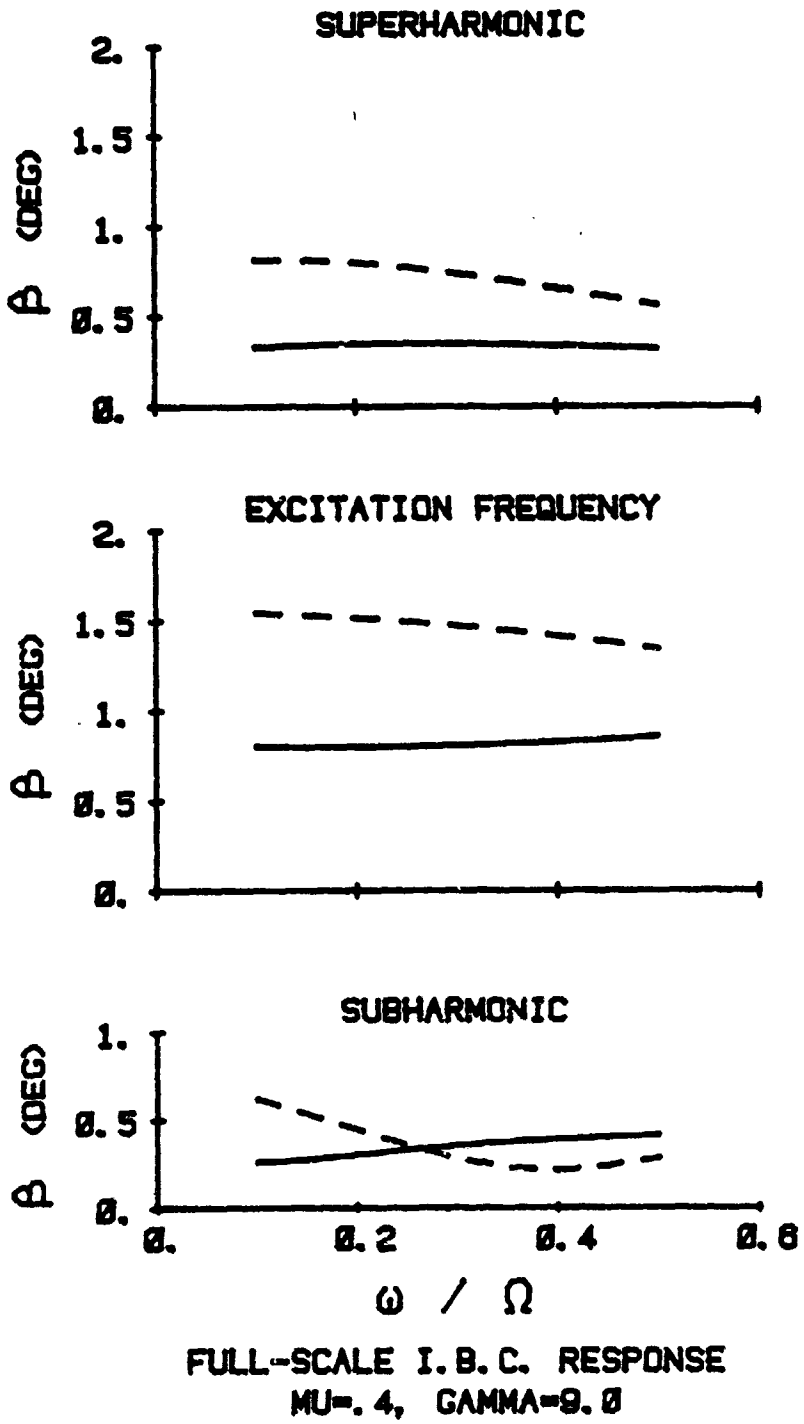

FIG. 29b (CONCLUDED)

APPENDIX

Upon substitution of the assumed solutions for the flapping and pitching motion of the blade into Equation 2, the following matrix equation resulted:

$$\begin{bmatrix} & 1 & \end{bmatrix} \begin{Bmatrix} \beta_o \\ \bar{\beta}_c \\ \bar{\beta}_s \\ \hat{\beta}_c \\ \hat{\beta}_s \\ \beta_c' \\ \beta_s' \\ \beta_c'' \\ \beta_s'' \end{Bmatrix} = \begin{bmatrix} & 2 & \end{bmatrix} \begin{Bmatrix} \theta_o \\ \bar{\theta}_c \\ \bar{\theta}_s \\ \hat{\theta}_c \\ \hat{\theta}_s \\ \theta_c' \\ \theta_s' \\ \theta_c'' \\ \theta_s'' \end{Bmatrix} + \begin{Bmatrix} & 3 & \end{Bmatrix} \bar{\omega}_e + \begin{Bmatrix} & 4 & \end{Bmatrix} \lambda$$

where the matrices $\begin{bmatrix} & 1 & \end{bmatrix}$, $\begin{bmatrix} & 2 & \end{bmatrix}$, {3}, and {4} are defined below:

$$\begin{bmatrix} & 1 & \end{bmatrix} =$$

$$
\begin{bmatrix}
1+G & 0 & 0 & \frac{1}{2}\mu(C-H) & 0 & 0 & 0 & 0 & 0 \\
0 & 1+G-\left(\frac{\omega}{\Omega}\right)^2 & A\left(\frac{\omega}{\Omega}\right) & 0 & 0 & \frac{1}{2}\mu\left(C-H\left(\frac{\Omega-\omega}{\Omega}\right)\right) & 0 & \frac{1}{2}\mu\left(C-H\left(\frac{\Omega+\omega}{\Omega}\right)\right) & 0 \\
0 & -A\left(\frac{\omega}{\Omega}\right) & 1+G-\left(\frac{\omega}{\Omega}\right)^2 & 0 & 0 & 0 & \frac{1}{2}\mu\left(H\left(\frac{\Omega-\omega}{\Omega}\right)-C\right) & 0 & \frac{1}{2}\mu\left(C-H\left(\frac{\Omega+\omega}{\Omega}\right)\right) \\
C\mu & 0 & 0 & G & A+\frac{1}{4}E\mu^2 & 0 & 0 & 0 & 0 \\
0 & 0 & 0 & -A+\frac{1}{4}E\mu^2 & G & 0 & 0 & 0 & 0 \\
0 & \frac{1}{2}\mu\left(C-H\left(\frac{\omega}{\Omega}\right)\right) & 0 & 0 & 0 & 1+G-\left(\frac{\Omega-\omega}{\Omega}\right)^2 & A\left(\frac{\Omega-\omega}{\Omega}\right) & 0 & \frac{1}{4}E\mu^2 \\
0 & 0 & \frac{1}{2}\mu\left(H\left(\frac{\omega}{\Omega}\right)-C\right) & 0 & 0 & -A\left(\frac{\Omega-\omega}{\Omega}\right) & 1+G-\left(\frac{\Omega-\omega}{\Omega}\right)^2 & \frac{1}{4}E\mu^2 & 0 \\
0 & \frac{1}{2}\mu\left(C+H\left(\frac{\omega}{\Omega}\right)\right) & 0 & 0 & 0 & 0 & \frac{1}{4}E\mu^2 & 1+G-\left(\frac{\Omega+\omega}{\Omega}\right)^2 & A\left(\frac{\Omega+\omega}{\Omega}\right) \\
0 & 0 & \frac{1}{2}\mu\left(H\left(\frac{\omega}{\Omega}\right)+C\right) & 0 & 0 & \frac{1}{4}E\mu^2 & 0 & -A\left(\frac{\Omega+\omega}{\Omega}\right) & 1+G-\left(\frac{\Omega+\omega}{\Omega}\right)^2
\end{bmatrix}
$$

$$
\begin{bmatrix} \\ Z \\ \\ \end{bmatrix} =
$$

$$
\begin{bmatrix}
B+\frac{1}{2}E\mu^2 & 0 & 0 & 0 & C\mu & 0 & 0 & 0 & 0 \\
0 & B+\frac{1}{2}E\mu^2 & 0 & 0 & 0 & 0 & 0 & 0 & 0 \\
0 & 0 & B+\frac{1}{2}E\mu^2 & 0 & 0 & C\mu & 0 & -C\mu & 0 \\
0 & 0 & 0 & B+\frac{1}{4}E\mu^2 & 0 & 0 & C\mu & 0 & C\mu \\
2C\mu & 0 & 0 & 0 & B+\frac{3}{4}E\mu^2 & 0 & 0 & 0 & 0 \\
0 & 0 & C\mu & 0 & 0 & B+\frac{1}{2}E\mu^2 & 0 & -\frac{1}{4}E\mu^2 & 0 \\
0 & C\mu & 0 & 0 & 0 & 0 & B+\frac{1}{2}E\mu^2 & 0 & -\frac{1}{4}E\mu^2 \\
0 & 0 & -C\mu & 0 & 0 & -\frac{1}{4}E\mu^2 & 0 & B+\frac{1}{2}E\mu^2 & 0 \\
0 & C\mu & 0 & 0 & 0 & 0 & \frac{1}{4}E\mu^2 & 0 & B+\frac{1}{2}E\mu^2
\end{bmatrix}
$$

$$\{3\} =$$

$$\begin{Bmatrix} 0 \\ 0 \\ \frac{\gamma}{6}(1-\xi^3) - \frac{\gamma}{40}\frac{1}{\mu^2}\left(\frac{\omega}{\Omega}\right)^2(1-\xi^5) + \frac{\gamma}{896}\frac{1}{\mu^4}\left(\frac{\omega}{\Omega}\right)^4(1-\xi^7) \\ 0 \\ 0 \\ \frac{\gamma}{8}\mu(1-\xi^2) - \frac{\gamma}{16}\frac{1}{\mu}\left(\frac{\omega}{\Omega}\right)(1-\xi^4) - \frac{3\gamma}{128}\frac{1}{\mu}\left(\frac{\omega}{\Omega}\right)^2(1-\xi^4) + \frac{\gamma}{192}\frac{1}{\mu^3}\left(\frac{\omega}{\Omega}\right)^3(1-\xi^6) + \frac{\gamma}{3072}\frac{1}{\mu^3}\left(\frac{\omega}{\Omega}\right)^4(1-\xi^6) - \frac{\gamma}{6144}\frac{1}{\mu^3}\left(\frac{\omega}{\Omega}\right)^5 \\ 0 \\ -\frac{\gamma}{8}\mu(1-\xi^2) - \frac{\gamma}{16}\frac{1}{\mu}\left(\frac{\omega}{\Omega}\right)(1-\xi^4) + \frac{3\gamma}{128}\frac{1}{\mu}\left(\frac{\omega}{\Omega}\right)^2(1-\xi^4) + \frac{\gamma}{192}\frac{1}{\mu^3}\left(\frac{\omega}{\Omega}\right)^3(1-\xi^6) - \frac{\gamma}{3072}\frac{1}{\mu^3}\left(\frac{\omega}{\Omega}\right)^4(1-\xi^6) - \frac{\gamma}{6144}\frac{1}{\mu^3}\left(\frac{\omega}{\Omega}\right)^5 \end{Bmatrix}$$

$$\{4\} =$$

$$\begin{Bmatrix} -C \\ 0 \\ 0 \\ 0 \\ -\epsilon\mu \\ 0 \\ 0 \\ 0 \\ 0 \end{Bmatrix}$$

This matrix equation can be used in the calculation of the flapping response due to gust with the feedback system engaged by substituting yet another matrix expression for the pitch vector. This expression would represent the frequency response of the feedback elements as follows:

Suppose that we have a transfer function relating the pitch input to the sensed flap output, including all the dynamics of the components of this feedback loop, of the form:

$$\frac{\theta(s)}{\beta(s)} = \frac{b_2 s^2 + b_1 s + b_0}{a_2 s^2 + a_1 s + a_0}$$

Then, since these components comprise a single input-single output system, we need only look at the effects upon the signal passing through this transfer block at a single frequency. Thus, we can substitute $s = j\omega$ above, and using Euler's formula and a bit of complex algebra, it can be shown that we can relate the cosine and sine components of the input signal to those of the output as:

where

$$\begin{Bmatrix} \theta_c \\ \theta_s \end{Bmatrix} = \begin{bmatrix} R & I \\ -I & R \end{bmatrix} \begin{Bmatrix} \beta_c \\ \beta_s \end{Bmatrix}$$

$$R = \left[(a_0 - \omega^2 a_2)(b_0 - \omega^2 b_0) + \omega^2 a_1 b_1\right] \Big/ \left[(a_0 - \omega^2 a_2)^2 + (\omega a_1)^2\right]$$

$$I = \left[\omega b_1 (a_0 - \omega^2 a_2) - \omega a_1 (b_0 - \omega^2 b_2)\right] \Big/ \left[(a_0 - \omega^2 a_2)^2 + (\omega a_1)^2\right]$$

where
- R denotes the real part of the complex number obtained via the $s = j\omega$ substitution
- I denotes the imaginary part
- θ_c, θ_s are the cosine and sine components of the output, respectively
- β_c, β_s are the cosine and sine components of the input.

Hence, to include the feedback dynamics in the gust response we need only construct a large matrix containing these smaller blocks along the diagonal,

evaluated at the particular harmonic of interest for each pair of inputs.

We can then rewrite the first matrix equation as:

$$\left[\begin{array}{c|} 1 \\ \hline \end{array}\right]\{\beta\} - \left[\begin{array}{c|} 2 \\ \hline \end{array}\right]\left[\frac{\theta}{\beta}\right]\{\beta\} = \{3\}\overline{\omega_c} + \{4\}\lambda$$

and it becomes clear that to solve for the flapping coefficients one need merely combine the two matrices that are products of $\{\beta\}$, invert, and multiply by the right hand side terms.